TD

Modelling of Low-Current Gas Discharges by Means of Stationary Solvers

DOCTORAL THESIS

Nuno Fábio Gomes Camacho Ferreira

DOCTORATE IN PHYSICS

UNIVERSIDADE da MADEIRA

A Nossa Universidade

www.uma.pt

May | 2022

Modelling of Low-Current Gas Discharges by Means of Stationary Solvers

DOCTORAL THESIS

Nuno Fábio Gomes Camacho Ferreira
DOCTORATE IN PHYSICS

ORIENTATION
Mikhail S. Benilov

Dedicated to the glowing memory of Victor Vieira Almeida,
a brilliant educator, my dear uncle with a golden heart

Acknowledgements

I wish to thank my supervisor, Professor Mikhail Benilov, a brilliant scientist and man. I had the honour of being his student already as an Engineering undergraduate student at Universidade da Madeira back in 2001, and now again as a Physics PhD student 20 years later. He has always been available, patient, and kept me aware of the required scientific rigour. I thank him for that, for the opportunities he gave me, for the chance of becoming a member of the Physics Group of Universidade da Madeira, and for the fruitful discussions. He has made possible the truly gratifying and unique experience of being part of a great research team, and take part of the long-established and successful collaboration with Siemens AG. I am grateful to Norbert Wenzel and the team in Siemens AG for kindly welcoming me into the ongoing research project at the time. I thank Professor Benilov for his continuous support, for keeping me motivated and for his trust in my abilities.

I acknowledge fruitfull collaboration with Professor Naidis, another brilliant mind, very pragmatic, insightful, and a very kind person. My colleagues Pedro Almeida and Diego Santos were very helpful throughout the development of the model and always available when I needed.

I am grateful to Professor Tarasenko and his group of the Institute of High Current Electronics in Tomsk, for their valuable support in providing the experimental results given in chapter 5.

I thank my friend, colleague and cousin Pedro Almeida for introducing me in the field of gas discharge physics. He was always enthusiastic and optimistic. His incentive and belief in my abilities were very important in this pursuit.

I would also like to thank my colleagues, Mário, Nelson, Helena, and Rui for the friendly environment and help everytime it was needed, for sharing their knowledge in physics, but also their experience concerning COMSOL and other software.

To my wife, Mónica, for her inexhaustible support and constant companionship and encouragement, to my beloved son and daughter, Guilherme and Filomena, for being a source of motivation, and to my mother, Paulina, for always being there unconditionally in my entire life, I am truly grateful. To Victor, I am sorry for not being able to show you this, I am sure you would be proud. A special thanks to my sister Mariana and my entire family, they were always supportive.

Preamble

The work leading to this thesis was performed within activities of:

- Research Fellowship BI-4/PTDC/FIS-PLA/2708/2012 in the framework of the project PTDC/FIS-PLA/2708/2012 *Modelling, understanding, and controlling self-organization phenomena in plasma-electrode interaction in gas discharges: from first principles to applications* of Fundação para a Ciência e a Tecnologia.

- Research project *Investigation of surface discharge development on dielectric surfaces* in the framework of the collaboration between Pole of Instituto de Plasmas e Fusão Nuclear in Universidade of Madeira and Siemens AG, Corporate Technology.

- Research project *Investigation of breakdown along dielectric surfaces in air and vacuum with application to vacuum circuit breakers* in the framework of the collaboration between Pole of Instituto de Plasmas e Fusão Nuclear in Universidade of Madeira and Siemens AG, Corporate Technology.

- Project Pest-OE/UID/FIS/50010/2019 of Fundação para a Ciência e a Tecnologia.

- Research Fellowship PlasMa/BI/2019-2 in the framework of the project PlasMa - M1420-01-0145-FEDER-000016 *PlasMa: teoria e simulação avançada de plasmas relevantes para aplicações energéticas*, co-financed by the Operational Program of the Autonomous Region of Madeira 2014-2020.

Most of the results presented in this thesis are published in the following articles:

- N. G. C. Ferreira, D. F. N. Santos, P. G. C. Almeida, G. V. Naidis, and M. S. Benilov, Simulation of pre-breakdown discharges in high-pressure air. I: The model and its application to corona inception (2019). J. Phys. D: Appl. Phys. 52 No. 35 355206-1-10

- N. G. C. Ferreira, P. G. C. Almeida, G. V. Naidis, and M. S. Benilov, Comment on "Electric field measurements under DC corona discharges in ambient air by electric field induced second harmonic generation" [Appl. Phys. Lett. 115, 244101 (2019)] (2020), Appl. Phys. Lett. 117 No. 2 026101-1-3

- P. G. C. Almeida, R. M. S. Almeida, N. G. C. Ferreira, G. V. Naidis, and M. S. Benilov, Simple computation of ignition voltage of self-sustaining gas discharges (2020) Plasma Sources Sci. Technol. 29 No. 12 125005-1-6

- N. G. C. Ferreira, P. G. C. Almeida, M. S. Benilov, V. A. Panarin, V. S. Skakun, V. F. Tarasenko, and G. V. Naidis, Computational and experimental study of time-averaged characteristics of positive and negative DC corona discharges in point-plane gaps in atmospheric air (2020) IEEE Trans. Plasma Sci. 48, No. 12 4080-4088

- N. G. C. Ferreira, G. V. Naidis, and M. S. Benilov, Simulation of pre-breakdown discharges in high-pressure air. II: Effect of surface protrusions (2021). J. Phys. D: Appl. Phys. 54 No. 25 255203-1-10

Results presented in this thesis were reported at the following conferences:

- M. S. Benilov, N. G. C. Ferreira, D. F. N. Santos, P. G. C. Almeida, and G. V. Naidis, Simulation of pre-breakdown discharges in air, Proc. 71st Gaseous Electronics (November 5-9, 2018; Portland, Oregon, USA), Bull. Amer. Phys. Soc., vol. 63, No. 10

- N. G. C. Ferreira, G. V. Naidis, and M. S. Benilov, Does field emission from 'real' surfaces affect the high-pressure air breakdown in electric power equipment?, 8th International Workshop on Mechanisms of Vacuum Arcs (September 15-19, 2019, Padova, Italy)

Resumo

Este trabalho é dedicado à modelização da ignição de descargas autónomas de baixa corrente, e de caraterísticas tensão-corrente médias de descargas de coroa.

Foi desenvolvida uma abordagem para simulação de descargas quasi-estacionárias de baixa corrente, sendo aplicável para descargas DC e também de baixa frequência. Esta abordagem colmata a lacuna entre os métodos modernos de modelização numérica e as abordagens de engenharia, e foi implementada como parte de um modelo numérico que simule as descargas referidas em ar de alta pressão. O modelo inclui equações de conservação e transporte de espécies carregadas e a equação de Poisson. Utiliza-se um modelo cinético 'mínimo' de processos químicos no plasma, em descargas de baixa corrente em ar de alta pressão, que tem em conta os eletrões, uma espécie eficaz de iões positivos, e os iões negativos O_2^-, O^-, e O_3^-. A implementação do modelo numérico é baseada no uso de *solvers* estacionários, que oferecem vantagens importantes em simulações de descargas quasi-estacionárias.

O modelo desenvolvido foi validado com dados experimentais numa ampla gama de condições, e foi aplicado a diversos problemas de alto interesse científico-tecnológico. Em primeiro lugar, investigou-se a ignição de descargas em ar de alta pressão numa ampla gama de condições. O método desenvolvido pode ser usado como preditor da tensão de rutura em dispositivos de alta tensão, bem como para avaliar a sensibilidade da tensão de ignição em relação a diferentes fatores (o esquema cinético usado, a fotoionização, e a emissão secundária de eletrões do cátodo). O segundo problema estudado foi o efeito que protuberâncias na superfície do ânodo podem ter nas descargas pré-rutura em ar de alta pressão, podendo ser considerado como uma evidência indireta da possível existência de micro-protuberâncias na superfície do elétrodo. O terceiro problema lidou com a investigação de caraterísticas tensão-corrente de descargas de coroa DC, numa ampla gama de correntes e separação entre elétrodos. Demonstra-se que as tensões de ignição calculadas estão em concordância com os dados experimentais. Micro-protuberâncias anódicas com comprimentos da ordem de $50\,\mu$m oferecem concordância qualitativa com a experiência em todos os casos. Os resultados da modelização revelam que as caraterísticas tensão-corrente calculadas oferecem boa concordância com os dados experimentais, e que os solvers estacionários permitem o desacoplamento da estabilidade física e numérica, bem como a redução do tempo de cálculo.

Palavras chave: Descargas de baixa corrente quasi-estacionárias. Descargas de

coroa. Ignição de descarga autónoma. *Solvers* estacionários. Caraterísticas de coroa DC.

Abstract

This work is dedicated to modelling of ignition of self-sustaining low-current discharges and time-averaged characteristics of corona discharges.

An approach for simulation of low-current quasi-stationary discharges has been developed, being applicable not only to DC but also to low-frequency discharges. Such approach bridges the gap between modern methods of numerical modelling and engineering approaches, and it has been implemented as a part of a numerical model of low-current quasi-stationary discharges in high-pressure air, The model comprises equations of conservation and transport of charged species and the Poisson equation. A 'minimal' kinetic model of plasmachemical processes in low-current discharges in high-pressure air is used, which takes into account electrons, an effective species of positive ions, and negative ions O_2^-, O^-, and O_3^-. The implementation of the numerical model is based on the use of stationary solvers, which offer important advantages in simulations of quasi-stationary discharges.

The developed model has been validated against experimental data over a wide range of conditions, and has been applied to several problems of high scientific and technological interest. Firstly, the inception of discharges in high-pressure air has been investigated over a wide range of conditions.The method developed can be used as a predictor of the hold-off voltage in high-voltage devices, as well as to evaluate the sensitivity of the ignition voltage with respect to different factors (the kinetic scheme used, the photoionization, and the secondary electron emission from the cathode). The second problem that has been studied was the effect that anode surface protrusions can have on pre-breakdown discharges in high-pressure air, which can be considered as an indirect evidence of the possible existence of microprotrusions on the electrode surface. The third problem concerned investigation of characteristics of DC corona discharges in a wide range of currents and gap widths. It is shown that computed inception voltages are in good agreement with experimental data. Anode microprotrusions with heights of the order of $50\,\mu$m yield qualitative agreement with the experiment in all the cases. It is also shown that the calculated current-voltage characteristics are in good agreement with the measured data, and that stationary solvers allow decoupling of physical and numerical stability and reduction of computation time.

Keywords: Low-current quasi-stationary discharges, Corona discharges, Ignition of self-sustaining discharge, Stationary solvers, Characteristics of DC corona

Contents

List of Figures

Chapter 1

Introduction

1.1 Low-current gas discharges

The field of gas discharge physics and the underlying phenomena related with the flow of electric current in ionized gases has been of interest for quite some time now, e.g. [1, 2], and still receives significant attention nowadays. There are various classifications for gas discharges according to its underlying features. Non-self-sustained discharges are those occurring only when an external ionization source is present or electron emission from the cathode is ensured, e.g., by an external radiation source. In contrast, self-sustaining discharges are those that are maintained even in the absence of the external mechanisms, when the applied electric field is such that sufficient ionization occurs. Another classification is related with the power supply being used: discharges may be powered by DC, low-frequency (e.g., 50 Hz), high-frequency (e.g., radio-frequency or microwave), and pulsed power supplies. Regarding the medium where the discharge occurs, it can be different gases at different pressures, or, alternatively, the discharge can also occur in vacuum. Another natural classification concerns the thermal state of the cathodes, e.g., cold and hot cathodes, which are intrinsically related with the discharge current. For cold cathodes, typically at lower discharge currents, the emission mechanism is secondary electron emission upon ion impact, or excited particle impact, or photoeffect. For hot cathodes, which are heated when a sufficiently high current is allowed by using a low external circuit resistance, the cathode produces thermionic emission and an arc discharge, also DC self-sustaining, usually develops.

Although many features of plasma processes are common in different types of discharges, e.g. [1, 2], there are also substantial differences. This thesis is dedicated to the study of low-current self-sustaining DC or low-frequency discharges, with typical examples being the Townsend and corona discharges, while discharges in high-frequency and pulsed fields are out of the scope of the thesis.

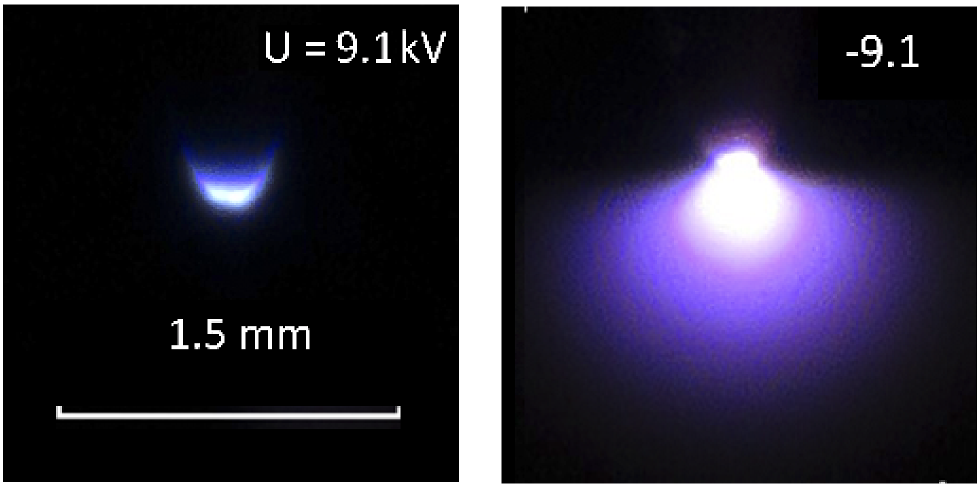

a) b)

Figure 1.1: Stationary glow corona discharge in point-to-plane at atmospheric pressure air. a): Positive corona; b): Negative corona. From [5].

Within the DC self-sustaining discharges, at lower currents there are the Townsend, or dark, discharge, the glow and corona discharges. The former two occur in uniform, or weakly non-uniform (e.g., in parallel-plate gaps) electric fields. The Townsend discharge is characterized by very low currents, and the applied electric field is not distorted. The glow discharge occurs at higher currents, and the applied electric field is distorted by space charge accumulating in the gap. Corona discharges, which have common features with the Townsend and glow discharges, occur in strongly non-uniform fields at voltages insufficient to cause the breakdown. If the stressed electrode is the cathode the corona is said to be negative whereas if it is the anode the corona is called positive. Spectacular glow is typically observed in the vicinity of the sharper electrode [3, 4], as seen in figure 1.1. The glow results from photons, which are released from excited radiating states.

Electron avalanches are fundamental in both the Townsend and corona discharges, and the plasmachemical processes occurring in the gas bulk are similar in both discharges. For definiteness, we will refer to air, an electronegative gas where attachment is an important mechanism since it contributes to electron losses. If the reduced electric field E/N (here E is the electric field strength and N is the number density of neutral molecules) strength in air is above about 100 Td (1 Td $= 10^{-21}$ V m^2), the ionization rate is higher than the attachment rate, and if it is below than about 100 Td, the rate of ionization is lower than the attachment. This value, of about 100 Td, is usually called the critical field. The process of recombination plays a minor role, particularly in very low currents. The charged particles drift toward the electrode of opposite charge by action of the electric field and eventually reach it, being neutralized. In the Townsend discharge the quasi-uniform electric field is equal to the critical field in the whole gap. The electric fields in corona discharges are strongly non-uniform. They are higher than the critical field in the so-called active zone, a thin region in the vicinity of the sharper electrode where ionization occurs, and are lower than the critical field in the so-called drift zone.

Primary electrons are needed so that subsequent avalanches occur in the region of enhanced electric field [1, 6]. In the Townsend or negative corona discharges, the primary electrons are generated mainly by the secondary electron emission from the cathode. The electric field in positive coronas is very weak at the cathode, meaning that secondary electron emission is a minor process. Additionally, the emitted electrons will be attached to oxygen molecules in the drift zone before arriving to the anode. Therefore, the primary electron generation in positive coronas is ensured by photoionization. This process consists of highly energetic photons ionizing neutral molecules in the gas near the edge of the active zone.

It is not unusual to find in the literature different terms for designating the initiation of a self-sustaining DC gas discharge, and also for designating the corresponding voltage V_t, i.e. the threshold voltage which is just sufficient for the ionization mechanisms to compensate losses of charged particles. For example, the terms 'self-sustaining condition' and 'breakdown condition' are used on p. 544 of [2] and the terms 'condition for initiating a self-sustaining discharge' and 'criterion of ignition (self-sustainment)' are found on pp. 131 and 175 of [1]. The terms 'ignition potential' and 'breakdown voltage' for designating V_t are referred as being equivalent in p. 133 of [1]. In electrical engineering, the term 'breakdown' has the meaning of a transition from low- to high-current discharge, usually spark or arc discharge. In this thesis, the term 'ignition' (of a self-sustaining discharge) is used following [1] and 'breakdown' refers to transitions from low- to high-current discharge. The problem of finding the so-called hold-off, or breakdown, voltage, in high-voltage electrical equipment, possibly in complex device configurations, is of utmost importance for the industry.

The discharge ignition and breakdown voltages may coincide or be quite distant from each other depending on the discharge conditions. The relation between these voltages is important and has been subject of attention in the literature, e.g. in the works [7–9] and the book [10]. If the gap width is not large enough such that the electric field distribution is not very non-uniform, the discharge inception and breakdown voltages either virtually coincide or breakdown occurs without a preceding low-current discharge. This can be seen in the schematic representation in figure 1.2, which refers

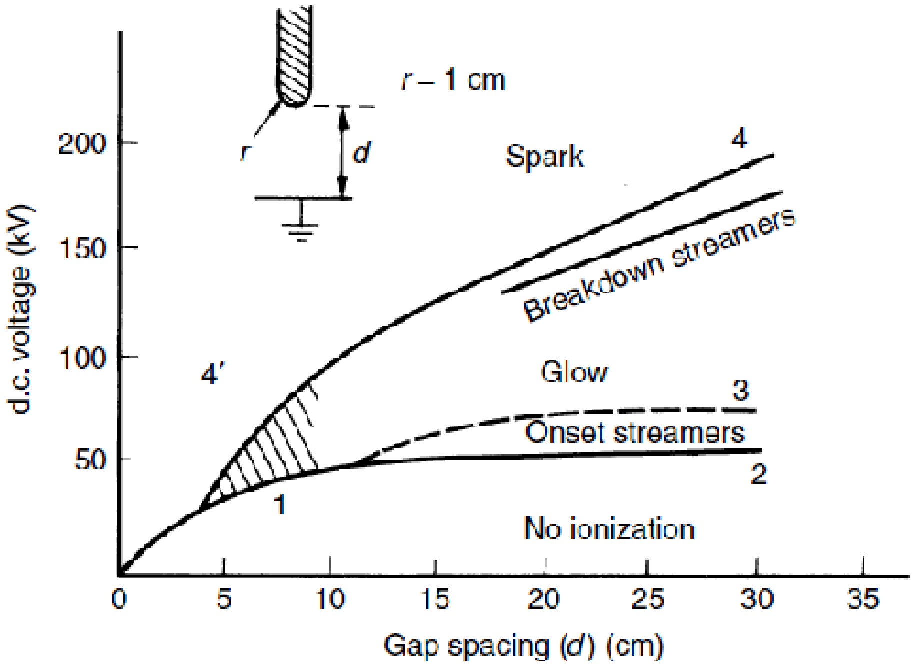

Figure 1.2: Relation between corona inception and spark breakdown voltages. Positive rod-to-plane configuration at atmospheric pressure air for various gap widths d, Fig. 5.33 from [10].

to a positive rod-to-plane configuration at atmospheric pressure air: for gap widths below approximately 4 cm, no corona is observed and the discharge is ignited in the spark mode. A steady-state glow corona can be observed for longer gap widths, and spark breakdown only occurs if the voltage is increased further.

Figure 1.3 shows experimental data for a positive discharge between concentric cylinders of diameters of 0.239 cm and 9.75 cm in air, for various relative pressures δ ($\delta = 1$ corresponds to atmospheric pressure). (Note that d designates the gap width in figure 1.2 and the diameter of the inner cylinder in figure 1.3.) The solid points and the dashed curve represent the experimental sparking voltages, and the open points represent the experimental corona ignition voltages. The solid line, marked with "COR", represents calculations based on empirical Peek's law [11] (expressed below in Eq. (1.1)). The gap width is around 9.5 cm, which is approximately 40 times the diameter of the inner cylinder. This means that the data shown in figure 1.3 for $\delta = 1$ can be compared with the data shown in figure 1.2 for a gap width of, for example, 20 cm. A steady-state glow corona can be observed in both cases and spark breakdown only occurs if the voltage is increased further.

Both the corona inception and spark breakdown voltages increase with increasing gas pressure. The spark breakdown voltage exhibits a maximum at a given pressure

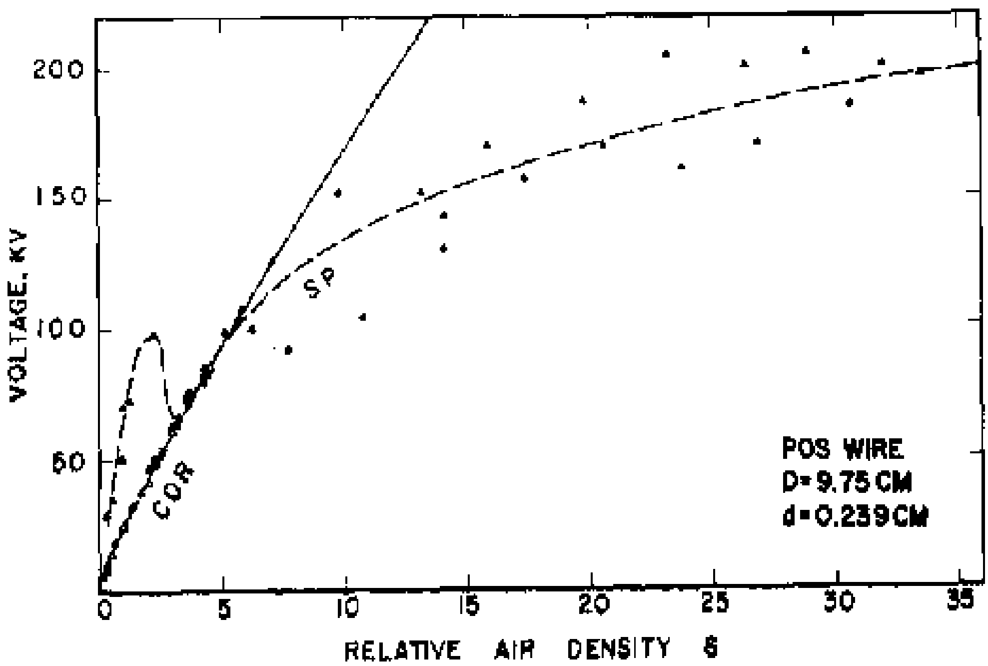

Figure 1.3: Relation between corona inception and spark breakdown voltages. Positive discharge between concentric cylinders in air at various relative pressures δ, Fig. 2 from [9].

and then declines as pressure is further increased. The reduction in the spark breakdown voltage is related to the net charge density increasing very rapidly with pressure, which means that a newly formed streamer can no longer be extinguished by the stabilized corona [7]. Hence, from a certain pressure, the spark voltage eventually coincides with the corona inception voltage. In figure 1.3, this is seen for $\delta \gtrsim 3$. For negative polarity, the behaviour is similar, however the region of stable glow corona, which precedes the spark breakdown, extends for higher pressures. The spark breakdown voltage is typically higher than that for positive polarity, except at low pressures.

1.2 Theory and modelling methods in the literature

The physics of many gas discharge systems has been understood reasonably well by now. High-quality data for evaluation of transport and kinetic coefficients and tools performing such evaluation are publicly available, e.g., LXCat [12] and LoKI [13]. Sophisticated ready-to-use toolkits have been developed for simulation of gas discharge systems, e.g., nonPDPSIM [14], Plasimo [15], and Plasma module of commercial software COMSOL Multiphysics®, which can follow discharge development on the subnanosecond scale, taking into account dozens of plasma species with hundreds of reactions. Such models are however too heavy to be routinely used in engineering practice. Although empirical formulae stemming from an extensive amount of experimental data on breakdown exist, its application is justified only within certain geometries and conditions, which are overly simplistic for engineering practice. On the other hand, extrapolation of such formulae for more realistic situations can lead to large errors. What is typically done in practice is the evaluation of the Townsend ionization integral, e.g. reviews [16, 17], where the effective ionization should reach a certain discharge-dependent level. Examples of empirical formulae are given in the next section and the method based on the Townsend ionization integral is discussed in the following section. A summary of analytical descriptions of corona current-voltage characteristic (CVC) is given in the subsequent section. Modelling methods will be reviewed in the final section.

1.2.1 Peek's law and similar formulas

There are analytical formulae that give the ignition voltage or ignition field in some particular situations, especially for air. Corona discharges occur in situations of strongly non-uniform electric fields, examples being concentric cylinders or parallel wires provided the radius r_0 of the smaller electrode is much smaller than the gap width d. For example, for parallel wires, if $d/r_0 < 5.85$, the field is not sufficiently non-uniform, therefore a corona does not form and a spark discharge occurs instead, e.g. [1, 6].

The corona ignition between concentric cylinders in air is described by the well-known empirical Peek's formula [11]:

$$E_c = 31\delta \left[1 + \frac{0.308\,\mathrm{cm}^{1/2}}{(\delta r_0)^{1/2}}\right] \mathrm{kV\,cm}^{-1}. \tag{1.1}$$

Here E_c is the electric field at the surface of the inner cylinder required to ignite the corona (the so-called inception field) and δ is the ratio of gas density to the normal density (the one corresponding to values of temperature of 25 °C and pressure of 1 atm). Note that the ignition voltage V_t is related to E_c by the formula $E_c = V_t/\left[r_0 \ln\left(R/r_0\right)\right]$, being R the radius of the outer cylinder.

An expression similar to Eq. (1.1) was derived by Frank Peek also for the spherical geometry [18]:

$$E_s = 19.3\delta \left[1 + \frac{0.54\,\mathrm{cm}^{1/2}}{(\delta r_s)^{1/2}}\right] \mathrm{kV\,cm}^{-1}. \tag{1.2}$$

Here r_s is the radius of the sphere. Note that the formula (1.2) is applicable for d in the range $d > 0.54\sqrt{r_0}$ (here d and r_0 are in centimeters), $d < 2r_0$. E_s is the sparkover field, rather than the corona inception field, and in this d range this field is virtually independent of the gap width.

Other forms of these expressions exist as well. For concentric cylinders, the authors [19] evaluated the so-called ionization integral (discussed in some detail in the next section), based on the electric field distribution across the gap and a specific dependence of the ionization coefficient on the electric field, and derived an expression to determine the ignition field E_c:

$$\left(\frac{E_c}{\delta}\right)^2 - 2\frac{E_c}{\delta}E_{cr}\ln\left(\frac{1}{E_{cr}}\frac{E_c}{\delta}\right) - E_{cr}^2 = \frac{K/C}{\delta r_0}. \tag{1.3}$$

Here $K/C = 42\,\mathrm{kV^2\,cm^{-1}}$ and E_{cr} is the critical field at the studied pressure. Expression (1.3) was taken from [10] and has to be solved iteratively for each value of δr_0 in order to determine E_c/δ.

Another example is the formula for the ignition field of corona in the spherical geometry, given in [20]:

$$E_c = b\left[1 + \frac{c\,\mathrm{cm}^{1/2}}{(r_0)^{1/2}}\right]\,\mathrm{kV\,cm^{-1}}, \tag{1.4}$$

where r_0 is the radius of the sphere, and the parameters b and c are constants. The values of b and c depend weakly on the nature of the applied voltage, whether it is DC or low-frequency AC. The DC inception field is on average $3-4\%$ higher or lower (for positive and negative corona respectively) when compared to AC. Neglecting this dependence, one can set $b \approx 29\,\mathrm{kV\,cm^{-1}}$ and $c \approx 0.45\,\mathrm{cm^{0.5}}$ to evaluate Eq. (1.4). The fact that the difference between the DC and AC inception fields is small is very important in the context of this thesis as will be discussed in section 1.3.

The dependence of E_c/δ on δr_0 given by Eq. (1.1) is shown by the solid line in figure 1.4 along with experimental data for varying r_0 and δ. It can be seen that the values given by Peek's formula are in good agreement with those observed experimentally for $\delta r_0 \lesssim 1$. For higher values of δr_0 however, Peek's formula gives values of E_c/δ that are higher than experimental data, represented in figure 1.4 by open circles and corresponding to measurements with $\delta = 1$ for conductors of large radius. Peek's formula, being empirically derived from experiments on conductors of smaller radius, is only valid within certain ranges of measurements and whence the deviation from experiments at large δr_0. The dashed line in figure 1.4 corresponds to values given by Eq. (1.3) with $E_{cr} = 24.36\,\mathrm{kV\,cm^{-1}}$, which is the value of the critical field in air at 1 bar according to [10]. This line is closer to the experimental data at high values of δr_0 whilst still being independent of d or R.

Note that the E_c for concentric cylinders is independent of outer cylinder radius R as long as the field strength at the surface of the outer cylinder does not exceed δE_{cr} [10]. For higher values of the electrode radius, or, equivalently, smaller values of the

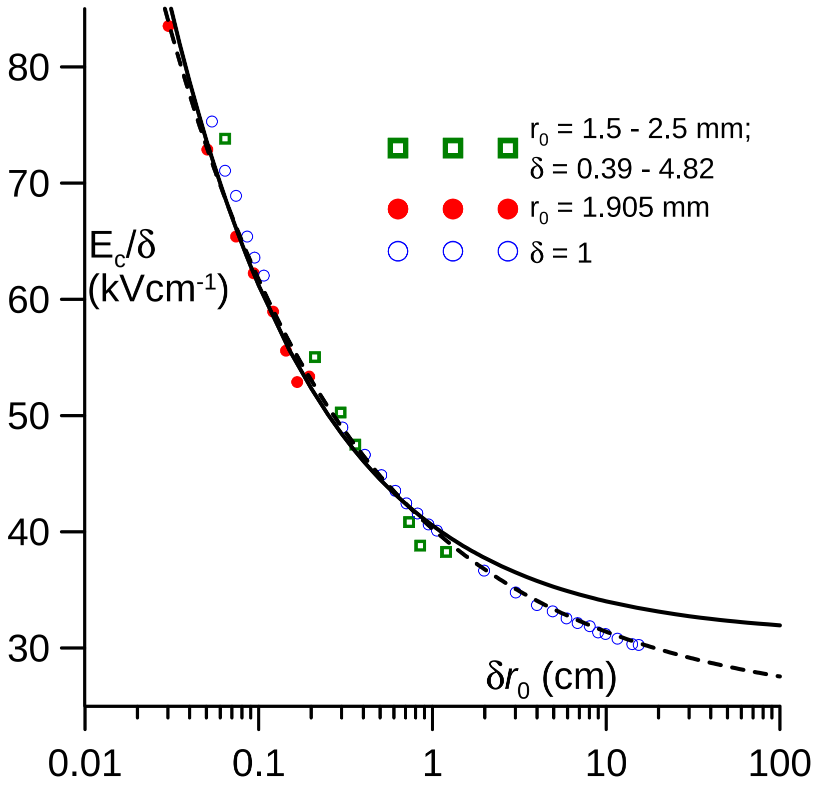

Figure 1.4: Reduced inception field, concentric cylinders in air. Solid line: Peek's formula (1.1). Dashed line: expression (1.3). Points: experimental data. Adapted from figure 5.28 of the book [10].

gap width, the field is more uniform along the gap and the region where the electric field is higher than the critical field extends further across the gap. In these situations, the inception field should also be a function of d or R while the discharge is still a corona. If the non-uniformity of the field in the gap is reduced further, eventually a spark will occur instead of a corona.

1.2.2 Townsend's criterion and evaluation of the ionization integral

Friedrich Paschen in 1889 [21] observed the non-monotonic dependence of the ignition voltage of gas discharges in parallel-plate gaps with varying pd, being p the gas pressure. The obtained experimental data constitute the so-called Paschen curves. An example is shown in figure 1.5, where the triangles and full circles represent measurements of breakdown voltage in air in medium gaps and pressures, and constitute the Paschen curve for air.

In 1915, John Townsend [23] proposed a theory to explain the process of ignition of a self-sustained discharge (the Townsend dark discharge), in which electrons are

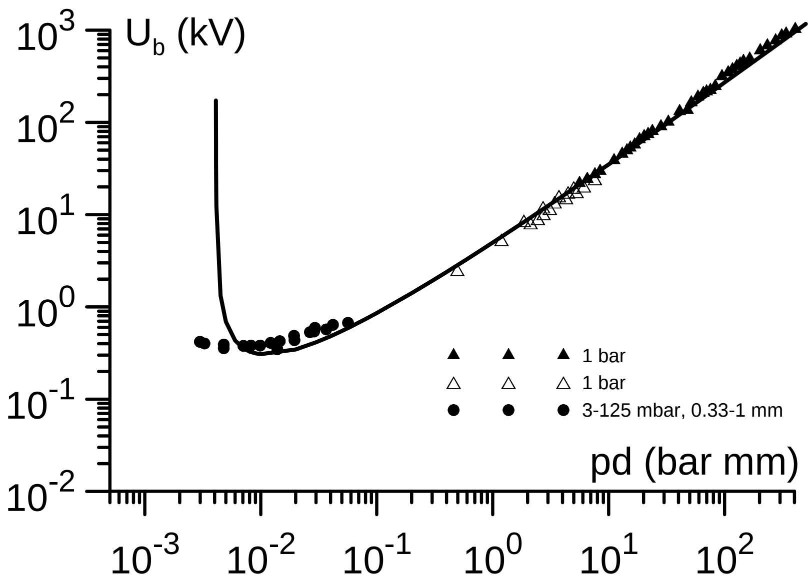

Figure 1.5: Breakdown voltage in uniform field in air for various air pressures p and gap widths d. Points: data from figure C1 of [22] (figure 5.23 of the book [10]). Line: ignition voltage V_t by Eq. (1.6) evaluated with $A = 15\,(\mathrm{Torr\,cm})^{-1}$, $B = 365\,\mathrm{V}\,(\mathrm{Torr\,cm})^{-1}$, and $\gamma = 10^{-2}$.

emitted from the cathode due to a secondary emission process and then the number of electrons in the avalanche grows exponentially towards the anode. The theory leads to the following self-sustainment criterion; e.g., Eq. 7.1 on p. 131 of [1] or Eq. 8 on p. 27 of [6]:

$$\alpha d = \ln\left(1 + \gamma^{-1}\right). \tag{1.5}$$

Here α is the so-called Townsend's ionization coefficient evaluated in terms of the applied electric field and γ is the effective secondary emission coefficient from the cathode. By evaluation of the Townsend criterion in Eq. (1.5) it is possible to determine directly the value of the self-sustainment voltage V_t, since the field is constant (spatially uniform) in this particular case and α is usually a known function on the reduced electric field.

When the ionization coefficient is written as a function of the electric field, the Townsend criterion gives a theoretical analog of the experimental Paschen curves, yielding the ignition voltage V_t for a given pd. As an example, let us assume the ionization coefficient as given in [1]: $\alpha = Ap\exp\left(-Bp/E\right)$, where A and B are constants obtained by fitting data on α, which is derived from experiments in which the discharge current was measured for various p and constant E/p. Substituting this formula into

Eq. (1.5), one obtains for the ignition voltage

$$V_t = \frac{Bpd}{\ln \frac{Apd}{\ln(1+\gamma^{-1})}}, \tag{1.6}$$

The solid line in figure 1.5 depicts V_t given by Eq. (1.6) obtained with $A = 15\,(\mathrm{Torr\,cm})^{-1}$ $(0.2\,(\,\mathrm{Pa\,cm})^{-1})$, $B = 365\,\mathrm{V}\,(\mathrm{Torr\,cm})^{-1}$ $(4.85\,\mathrm{V}\,(\,\mathrm{Pa\,cm})^{-1})$, and $\gamma = 10^{-2}$ [1].

Electron attachment can contribute significantly to electron losses in electronegative gases such as air. The so-called effective ionization coefficient $\overline{\alpha} = \alpha - \eta$ is commonly used in such gases to represent the net ionization rate, where η represents the electron attachment coefficient.

An accurate generalization of the classical Townsend criterion to 3D does not require additional assumptions, apart from those that need to be made for the derivation of this criterion in 1D (no photoionization, no detachment, and negligible contribution of negative ions to the current transport to the anode in comparison with electrons). The generalization coincides with the classical Townsend criterion, except that the so-called ionization integral appears instead of the product αd:

$$\int_0^{z_c} \overline{\alpha}\, dz = \ln\left(1+\gamma^{-1}\right). \tag{1.7}$$

Here z_c is the coordinate measured along a field line, counted from the anode to the cathode. Equation (1.7) represents the self-sustainment condition: the applied voltage should ensure that the ionization integral along at least one field line attains the value $\ln\left(1+\gamma^{-1}\right)$. Obviously, this will happen first for the field line where the ionization integral takes a maximum value.

For other cases (e.g., corona discharges with account of photoionization) the self-sustainment condition commonly used is based in an empirical criterion relating the ionization integral with a dimensionless parameter K, which is typically in the range $5 - 20$:

$$\int_l \overline{\alpha}\, dl = K. \tag{1.8}$$

Here l is the path for which the integral attains a maximum value (e.g., for axially symmetric configurations l coincides with the line along the axis, starting from the stressed electrode). For a known value of K, a known electric field distribution near the stressed electrode, and a known dependence of $\overline{\alpha}$ on the reduced electric field, it is possible to solve this equation for the ignition voltage V_t. The determined value will have nevertheless a significant error due to the somewhat arbitrary choice, dependent on the discharge configuration and conditions, of the value of K. The value $K = \ln\left(1+\gamma^{-1}\right)$ is typically used to determine the onset of a negative corona. Typical values of the secondary emission coefficient of the cathode fall between $10^{-2} - 10^{-5}$, which yield values of $K \approx 5 - 12$, respectively. The values $K \approx 18 - 20$ are used to determine the onset of a positive corona discharge; e.g., section 12.6.2 of [1] and section 4-II-B of [6]. The integral in Eq. (1.8) is also used in the literature for determining the occurrence of breakdown through the streamer mechanism, with K around $\ln 10^8 \approx 18$; the Meek breakdown condition [24, 25] (e.g., Eq. 12.9 on p. 336 of [1]).

There are several works in the literature both on ignition and breakdown in which the integral in Eq. (1.8) is used and discussed. In [26] the corona inception and breakdown in a coaxial cylindrical geometry were studied. The authors measured corona inception (discharge voltage for currents of the order of $0.5 - 1\,\mu$A) and the breakdown potentials in dry air in the pressure range $0.025 - 760\,$Torr ($3.33 - 1.01 \times 10^5\,$Pa). The measured voltage of inception of positive corona was compared with values given by Eq. (1.8) (evaluated in terms of assumed dependencies $E\left(r\right)$ and $\alpha = \alpha\left(E/p\right)$; attachment was neglected), using $\gamma = 5 \times 10^{-3}$ and $K = \ln\left(1 + \gamma^{-1}\right) \approx 5$ and a good agreement was found over the range of $pr_0 = 0.001 - 1.5\,$Torr m ($0.133 - 2 \times 10^2$ Pa m). Note that, as established in the literature, e.g. [1, 6], K values appropriate for the onset of positive corona are between $18 - 20$, while $\ln\left(1 + \gamma^{-1}\right)$ is appropriate for the case of negative corona. Concerning the breakdown (sparking) potentials, it was observed that at $p < 100\,$Torr ($1.33 \times 10^4\,$Pa) the corona inception and sparking voltages are very close to each other. For higher pressures, a corona discharge clearly precedes the occurrence of sparking as voltage is gradually increased. The difference between the corona inception and sparking voltages increases as p increases (this is seen in figure 1.3 in the range $\delta = 0.1 - 2$). The measured sparking voltage for the positive polarity is higher than for the negative one at $p < 375\,$Torr ($5 \times 10^4\,$Pa); as pressure is increased, the reverse happens, which is in line to what is seen in the literature, e.g. [10].

In [27] the ionization integral was evaluated for conditions of experiments in uniform field gaps, filled with electronegative gases, using the measured values of the breakdown potential given in [22] and dependencies $\alpha = \alpha\left(E/p\right)$ and $\eta = \eta\left(E/p\right)$ taken from the literature as a function of pd. It was found that K was not constant but a function of pd. Approximate expressions were derived, where K varies between 1 and 74 for air and between 3 and 8 for nitrogen. The author identified two distinct patterns for different ranges of pd, and claims this could be an indication of two different breakdown mechanisms present at low and high pd: the Townsend and streamer breakdown respectively, in accordance to what is expressed in [1]. The obtained value for K in air at $pd = 1\,$bar cm ($1 \times 10^5\,$Pa cm) is 20, which is in line to what is commonly used for breakdown. At different values of pd however, the use of $K \approx 18$ (which is based on the assumption that the avalanche size has reached 10^8 electrons, yielding $K = \ln 10^8$) can lead to significant error in the estimation of the breakdown voltage, with $8 - 50\%$ difference being seen between the estimated and measured values.

The ionization integral was evaluated in [28] in conditions of experiments of breakdown in uniform gaps described in the literature using different $\overline{\alpha}\,(E/p)$ dependences, and it was concluded that using the dependence $\overline{\alpha}/p = C\,[E/p - (E/p)_M]^2 - A$, with $A = 0.2873\,(\,\mathrm{mm\,bar})^{-1}$ $(2.87 \times 10^{-6}\,(\,\mathrm{mm\,Pa})^{-1})$, $C = 1.6053\,\mathrm{mm\,bar\,kV^{-2}}$ $(1.61 \times 10^5\,\mathrm{mm\,Pa\,kV^{-2}})$, and $(E/p)_M = 2.165\,\mathrm{kV}\,(\,\mathrm{mm\,bar})^{-1}$ $(2.17 \times 10^{-5}\,\mathrm{kV}\,(\,\mathrm{mm\,Pa})^{-1})$ brought the results closer to the experiment, and the value $K = 9.15$ is suitable to calculate the breakdown or inception voltages in uniform field air gaps. The typically used value of $K \approx 18$ is associated with higher values of $\overline{\alpha}/p$.

In [29] the ionization integral was evaluated with several values of K in conditions of corona onset in air known from different experiments described in the literature, without making distinction between different corona polarities. A good agreement was found for $K \approx 9$. In addition, it was shown that the evaluation of the ionization integral with $K = 9$ in cylindrical and spherical geometries, using respectively quadratic or linear approximations for the dependence of $\overline{\alpha}/N$ on E/N, leads to a formula close to the classic Peek's equation for corona onset. The best agreement with the experiment is achieved with K equal to 9, which is significantly below the values $\ln\left(1 + \gamma^{-1}\right)$ or 18, appearing in the Townsend and the streamer breakdown criteria respectively. The potential reasons invoked by the authors for such value of K are multi-step processes such as photo detachment and metastable detachment of electrons from negative ions (e.g., $\mathrm{O_2^+} + \mathrm{O_2}\left({}^1\Delta_g\right) \rightarrow \mathrm{e} + 2\mathrm{O_2}$), two-step ionization (e.g., $\mathrm{A} + \mathrm{e} \rightarrow \mathrm{A}^* \rightarrow \mathrm{A}^+ + 2\mathrm{e}$), and associative ionization (e.g., $\mathrm{A} + \mathrm{A}^* \rightarrow \mathrm{A}_2^+ + \mathrm{e}$). These processes are also described in [1] for explaining breakdown at intermediate values of pd.

In [30], conditions for inception of positive corona discharges in air in spherical and cylindrical geometries are considered. The author states that a physical mechanism capable of providing the values of $K \approx 9$ used in [29], especially for positive coronas, has not been revealed unambiguously. The inception field is evaluated in [30] by applying the criterion of equality of the number of ionizing photons produced by the primary avalanche to that produced by all secondary avalanches. From this criterion, for known dependence $E\,(r)$ governed by the Laplace equation, the corona onset is determined by calculating the value of the onset electric field at the anode. This onset field is then used for evaluation of (1.8), which gives K. The dependence of K on $r_0\delta$ is weak for low values of $r_0\delta$ and its values for cylinders are close to those for spheres. At large $r_0\delta$, K increases with $r_0\delta$. At normal air density the results are similar to those found in the work [29], being $K \approx 9$ for $10^{-2}\,\mathrm{cm} < r_0 < 10^{-1}\,\mathrm{cm}$ and then increasing for higher values of r_0. Contrary to what was suggested in [29], positive corona inception in [30] is shown to occur under the effect of direct ionization only, without the need to introduce multi-step processes.

The effect of humidity on inception of positive corona in the point-to-plane configuration was studied in [31]. The measured inception voltage was compared with values given by the ionization integral evaluated for different field lines with account of the requirement of the minimal avalanche size imposed by the critical volume model. The critical volume is defined as a volume sufficient for an avalanche to grow and reach a size which provides a certain minimum value of the ionization integral Eq. (1.8). The value $K\ = 10$ provides a good agreement with the experiments at atmospheric pressure in the range of humidity values from 1 to 20 g m^{-3}.

In [32] the avalanche growth and streamer inception near curved (spherical and needle-like) electrodes in air at elevated gas densities are analyzed. At elevated gas densities corona starts as a streamer corona. An inception criterion for positive corona is derived taking into account an "electrostatic compression", due to the curved anode, of the avalanche head: $K = K_0 + \ln\left(R_0\,\mathrm{cm}^{-1}\right)$, being R_0 the radius of the anode curvature and $K_0 \approx 18$. For R_0 of the order of 1 cm, this gives a value of K of around 18, i.e., the usual streamer breakdown criterion. However, the evaluation of the ionization integral for corona onset under conditions of numerous experiments typically gives $K \approx 9 - 10$. Thus, a discrepancy of a factor of about 2 is present. The author mentioned that the conventional ionization coefficient $(\alpha - \eta)$ is not accurate enough and has to be replaced by a coefficient which accounts also for electron detachment and was introduced in another work [33].

The work [34] investigated breakdown voltages, by means of both experiments and simulations, in quasi-uniform fields using a concentric cylinder configuration with a gap of 5 mm, in several gases in a wide range of pressures, up to 100 bar (1×10^7 Pa). The experiments have shown that at pressures below approximately 5 bar (5×10^5 Pa) the breakdown voltage increases linearly with p, but at higher pressures the breakdown voltage increases only weakly, i.e. tends to saturate. The saturation was explained by the authors as a consequence of roughness of the electrode surface (apparently the anode, although the authors do not indicate expressly the polarity). The experimental data were compared with results of estimates performed by means of an elementary electrostatic modelling: a cylindrical protrusion on the anode surface was considered and the ionization integral was evaluated assuming that the streamer breakdown corresponds to $K = 10.5$. The so-called "aspect ratio" of a protrusion is the ratio between its height and tip radius. Protrusions with the aspect ratios of 50 and 100 were required in order to obtain agreement with the experiments. This work is an illustration of deviations of breakdown voltage from Paschen curve observed at very high pressures, from 5 bar up to 100 bar (the experimental data are shown with full squares and open circles in figure 4.1). Concerning deviations of breakdown voltage from Paschen curve observed in microgaps, analytic equations for determination of the breakdown voltage for any gas at atmospheric pressure in microgaps were derived in [35], and it was obtained excellent agreement with experimental data, showing that field emission is significant and contributes to these deviations in microgaps.

In [36] the authors rely on a matched asymptotic analysis of a simplified but self-consistent problem, including equations of conservation and transport of charged species and the Poisson equation, and derived an explicit analytical solution for the current-voltage relation of corona discharge, and its onset voltage, for cylindrical electrodes. The matched asymptotic analysis or, as it is commonly known, the method of matched asymptotic expansions, is used to solve equations describing physical processes that are dominant in some regions (boundary layers) and negligible elsewhere, which is the case of the active and drift regions of corona discharges. The analytical model allows to evaluate, for instance, the effect of different diameters of the internal cylinder on corona current. An equation similar to Peek's law is derived for evaluating the onset surface electric field, which gives values in agreement with those given by the onset criterion given in [30]. The equation is applicable to gases other than air and different densities and can be used to validate previous approaches.

Recently in [17] it was introduced a method of calculation of breakdown voltage, which is built upon the ionization integral and consideration of the streamer-induced field superposed to the background electric field. The method aims to improve and simplify calculations in air and SF_6, and takes into consideration field distributions in arbitrary non-uniform fields. Unlike several other studies, the value of K is not pre-determined but found by means of an iterative method that runs until the ignition condition is satisfied and the number of charge carriers tends to infinity. The background field must be calculated first by a finite element method, and for each electrode geometry new calculations are required.

In summary, within the analytical methods for determining the ignition and breakdown voltages, the Townsend criterion given by Eq. (1.5) for the 1D case, or by Eq. (1.7) in the general 3D case, is the only method based on the first principles. However, it has a limited applicability and cannot be generalized to discharges where dominant processes go beyond the electron impact ionization and secondary electron emission by the cathode. In these cases, the criterion given by Eq. (1.8) is commonly used, where the value of K is chosen somewhat arbitrarily and depends on the discharge configuration and conditions.

1.2.3 Analytical description of corona current-voltage characteristics

The determination of the DC corona current-voltage characteristic is of interest for a variety of reasons, e.g. for calculating the distributions of ion current density and electric field intensity on high voltage transmission lines systems. Part of the charge carriers produced in the active zone drift towards the opposite electrode, being positive ions in the case of positive coronas, and negative ions in negative coronas (or electrons if the gas is not electronegative). The corona current is determined by the applied voltage (rising above the ignition voltage) and is limited by the space charge in the drift zone.

Initially derived by Townsend in 1914 [37], the approximate CVC of a low-current DC corona discharge between concentric cylinders with a wide gap is expressed by the so-called Townsend relation, usually given by the following formula:

$$I_l = \frac{8\pi\mu\varepsilon_0 U\left(U - V_t\right)}{R^2 \ln\left(\frac{R}{r_0}\right)}. \tag{1.9}$$

Here I_l is the corona current per the unit length, μ is the mobility of the ions that are believed to dominate current transfer in the drift region, ε_0 is the permittivity of free space, and U is the applied voltage. It should be noted that Eq. (1.9) appears vastly in the literature, examples being [1, 6, 38]. However, in the work by Townsend in 1914 [37], the expression has the ignition voltage V_t instead of the applied voltage U in the numerator (the derivation is detailed in Appendix B). The expression derived by Townsend is mathematically correct and it was derived using the first approximation for low current. One can rewrite Eq.(1.9) as:

$$I_l = CU\left(U - V_t\right), \quad C = \frac{8\pi\mu_i\varepsilon_0}{R^2 \ln\left(\frac{R}{r_0}\right)}.$$

In terms of the applied voltage we have

$$U = V_t + \frac{I_l}{CU}.$$

This means that for low currents ($I_l \approx 0$) $U \approx V_t$, and as current increases there is a correction parameter. If one expands Eq.(1.9) in the small parameter ε, where $U = V_t + \varepsilon$, and neglects the second order term of the order of ε^2, we have

$$I_l = C\left[\left(V_t + \varepsilon\right)\varepsilon\right] = C\left[\varepsilon V_t\right] = CV_t\left(U - V_t\right),$$

which is the same as the expression appearing in [37].

For point-to-ring and point-to-plane configurations, at large gap widths, a formula similar to Eq. (1.9) gives the relation between the corona current I and the applied voltage, $I = C\left(U - V_t\right)$, where C is a constant determined experimentally and dependent on geometrical factors and mobility of ions [39, 40]. For shorter gap widths, the work [40] has shown that Eq. (1.9) does not hold due to increasing participation of current transported by electrons, and the CVC is rather described by an (empirical) formula $I = C\,(U - V_t)^2$. Similar relations for the CVC of corona discharges in point-to-plane configuration can also be found in the literature, e.g. the work [41], where a relation $I = C\,(U - V_t)^m$ was proposed on the basis of experiments, with m within the range $1.5 - 2.0$. Measurements of positive and negative corona discharges between coaxial cylinders in atmospheric pressure air were performed in [42], and the measured data were compared with different formulae based on the Townsend relation Eq. (1.9), showing that the current-voltage characteristics can also be expressed as $I = C\,(U - V_t)^m$, similar to the point-plane geometry at high currents.

Although there is not an explicit expression for the CVC, the works [43, 44] use a similar procedure and give an expression relating the electric field distribution with the corona current between concentric cylinders. The classic Townsend-Kaptzov assumption is taken into consideration, which states that the steady state electric field at the conductor surface remains at the corona onset value E_c, given by Peek's formula, and the following expression for the electric field distribution is given:

$$E^2\,(r) = \frac{I_l}{2\pi\varepsilon_0\mu}\left(1 - \frac{r_0^2}{r^2}\right) + \left(\frac{E_c r_0}{r}\right)^2. \tag{1.10}$$

This expression is the same shown in Eq.(B.2) in Appendix B.

At very low corona currents the space charge does not distort the external field. When increasing the current, the space charge starts perturbing the electric field distribution and eventually it will completely dominate it (the so-called saturation limit). In [45] it was investigated coaxial cylinders and point-to-plane corona discharges, under time-dependent electric fields, and the effect of space charge on the ion current in the drift zone (assuming only one charge carrier species), for the case where space charge dominates the electric field in the drift zone. An approximate distribution of current density is derived, equivalent of the so-called Warburg distribution, which describes the current density distribution over the plane electrode for point-to-plane configurations. Equations were derived for the upper limit of current in a given corona geometry. It is demonstrated, building upon the unipolar charge drift formula, which describes the distribution of charge density with time along the path of a cloud of unipolar ions drifting with constant mobility, that corona currents in excess of that limit always involve free electron and/or bipolar conduction phenomena, like streamers.

1.2.4 Numerical modelling

We can also find in the literature many studies which use numerical modelling methods to investigate gas discharge dynamics and determine the ignition and breakdown voltages. The studies described here are those in which the employed numerical methods are of general use for studying low-current discharges, or those in which corona discharges or breakdown conditions (e.g., deviations from Paschen curve) are studied.

Time-dependent solvers are virtually universally employed in gas discharge modelling, including popular ready-to-use software such as the nonPDPSIM code [14], the Plasma module of COMSOL Multiphysics, and the Plasimo code [15]. The nonPDPSIM code is based on a previous model (LAMPSIM) that was used in particular for studying the dynamics of microdischarge devices, and is a time-dependent two-dimensional multifluid hydrodynamics model in which the Poisson equation and conservation equations are solved for densities and momenta of charged and neutral particles, and for radiation transport. The Plasma module of COMSOL Multiphysics is a specialized tool for modelling low temperature gas discharges, and although it is intended to work with time-dependent solvers, it can still be used with stationary solvers [46]. The work [15] illustrates the features of the Plasimo code, a toolkit for the numerical simulation of plasma sources of various degrees of equilibrium. It comes with a number of electromagnetic modules, flow solvers, modules for calculating transport coefficients, radiation transport and for the generation of ortho-curvilinear coordinate systems (those in which vectors aligned with the three coordinate directions are mutually perpendicular, and in which the variation of a single coordinate will generate a curve in space). Plasimo supports transient and steady-state simulations of plasma sources in one-, two and three-dimensional geometries. The code was used recently in [47] as one of six different codes being compared for simulation of positive streamers in air.

The work [48] is concerned with modelling positive glow corona between concentric spheres or cylindrical electrodes in air at atmospheric pressure. The model comprised conservation equations for electrons, positive ions, negative ions and metastable oxygen molecules, coupled with the Poisson equation, and the non-stationary 1D equations were solved. The simulation results showed the occurrence of onset streamers prior to positive glow current pulses with 'saw-tooth' shape. The corresponding light intensity was in the form of sharp pulses which coincided with the sharp rise in current near the anode.

In [49] it was investigated ion generation processes and breakdown characteristics in atmospheric air between two parallel plates in microscale gaps. The numerical simulation was performed by means of particle-in-cell and Monte Carlo (PIC-MC) techniques and allowed the evaluation of ionization coefficients, discharge current, and breakdown voltage. The deviation of the breakdown voltage from the Paschen curve for microscale gaps is shown by results of simulations with account of electron field emission.

In [50], a so-called 1.5-D numerical calculation is performed in order to study the physics of the temporal and spatial evolution from the negative corona to diffusive glow discharge, and transition to spark, in a pin-to-plane discharge. Three conservation equations of charged species along with the Poisson and the electric circuit equations are solved. The model is considered 1.5-D since it studies the evolution of the discharge parameters changing only along the axial direction. For this purpose, the plasma parameters are considered to be constant within the current cross section with area $S(x)$, being this area a known function of the axial location x. It was found that Trichel pulses features (amplitude and repetition frequency) can be controlled effectively by geometrical and gas-dynamical effects, and the diffusive glow discharge in the pin-to-plane corona necessarily occurs before transition to a spark as transient discharge in static air.

The work [51] is dedicated to simulation of a negative corona discharge in air in a 2D blade-to-plane geometry. The model was implemented using the COMSOL Multiphysics platform, by solving conservation equations for the transport of three charged species coupled with the Poisson equation for the electric field. Electron field emission was taken into account by incorporating the Fowler-Nordheim current into the electron current at the cathode. The diffusion component in fluxes of charged species was neglected, as well as photoionization, and the authors mention the use of artificial diffusion to avoid numerical instabilities. The temporal evolution of the species densities and the discharge current were monitored until a steady-state is reached. Successively increasing step in voltages were applied until the corona discharge onset was established, which was defined by calculation of a discharge current of the order of milliampere. The authors mention that the applied voltage was higher than that observed in experiments because it was not considered a magnification factor for the applied electric field at the cathode in order to take into account the microscopic field-effect emission at the cathode surface. A similar method was employed in [52] for computing the electric field change due to the ion flow generated by corona discharges under a high-voltage DC bipolar transmission line. In the work [52] a field enhancement factor β was introduced to describe effects of roughness of the conductor surface. The real geometry used in high-voltage transmission lines (composed of many stranded sub-conductors) was simulated directly, which was possible by means of the simulations being 2D. The numerical results agreed well with those of experiments in the electric field strength and the ionic current density when the used value of β is between 5 and 6.

In [53] simulations of the temporal evolution of corona current and space-charge density in air in point–plane geometry were performed, under step and pulsed applied voltages. The model accounts for single-species charge carriers and neglects the ionization zone (positive ions are assumed injected from the corona electrode). The electric field is calculated by means of finite-element method and the space-charge density calculated with the flux-corrected transport technique (discretization and coefficient matrix are manipulated), which can capture the steep density gradients while avoiding spurious oscillations and introduction of artificial diffusion. Later the same authors expanded the model to three charged species in order to study Trichel pulse regime of corona discharge in air and the effect of different parameters on Trichel pulse characteristics [54].

A finite element model was developed in [55] to perform 2D axisymmetric simulations of negative corona discharge in point-to-plane configuration with and without a dielectric barrier over the plane electrode, and to study the dynamics of volume charge generation, electric field variations and charge accumulation over the dielectric surface. The model comprises conservation equations for the transport of three charged species coupled with the Poisson equation for the electrostatic potential. It was found that before the occurrence of the first Trichel pulse (electron multiplication stage) the maxima of both positive ion and electron densities are not at the symmetry axis but situated at some distance away and the plasma actually forms a charged torus ring rather than a charged ellipsoid. Trichel pulses characteristics were studied and validated by comparison with experimental data. In the case of the dielectric barrier only one pulse is produced rather than a pulse sequence as is the case of the corona discharge, due to accumulated surface charge distorting the electric field.

The work [56] is dedicated to investigation of formation of Trichel pulses in negative DC corona in atmospheric air for a needle-plane configuration. The numerical model was implemented using the COMSOL Multiphysics platform and comprises three charged species transport equations as well as the Poisson equation. A thorough analysis of distribution of charged species in the gap during the different stages of Trichel pulse formation was done, as well as the evaluation of time variation of peak densities and total number of charged species. The transition of the discharge from the Trichel pulse regime to glow discharge occurred when increasing the applied voltage, at which the current waveform becomes flat and a plasma channel is formed from the cathode to the anode.

In [42] it was studied numerically stationary positive and negative DC corona discharges between coaxial cylinders in atmospheric pressure air. The model comprises 1D conservation and transport equations of electrons, positive and negative ions, coupled with the Poisson equation. Diffusion was neglected in the transport of charged species and the considered reactions were ionization and attachment. The surface onset fields given by the model were close to those given by Peek's formula. Also considered was a simplified model, which neglects the electrons, and considers only the transport equation of one ion species (positive or negative depending on the corona polarity), coupled with the Poisson equation. The simulation results given by both models are almost the same for low corona currents, but differ significantly for higher currents. The ionization region has no significant effect on the current-voltage characteristic provided that the corona current is low.

In [57] a model is proposed to simulate stable glow corona discharges in coaxial-cylinder and point-to-plane geometries, and a transition of the corona between coaxial cylinders to streamers, in atmospheric air, and validated the model by comparison of simulation results with those given by a more complex model and experimental data. The numerical simulations performed employed a two-step segregated procedure where the stationary conservation equation for electrons was solved followed by time-dependent conservation equations for ions. Due to the characteristics of stable glow corona discharges, which allow to assume that electrons reach a quasi-steady state within the characteristic time of ion drift, the electron conservation equation was written in the quasi-stationary approximation. Jointly with the use of simplifications of the physical model, these features eliminated the constraint on the time step imposed by the electron drift time and thus allowed the time step to be significantly increased. However, the ion conservation equation included the time-dependent term, hence the constraint imposed by the ion drift time remained.

PIC simulations for computing the breakdown voltage for any gas at atmospheric pressure in microgaps were performed in [35]. The PIC code utilized was a modification of the XPDP1 (1-D in space and 3-D in velocity) which incorporates field emission. The simulation results are in excellent agreement with experimental data, showing that field emission can be significant and contributes to deviations of breakdown voltage from Paschen curve observed in microgaps.

The work [58] is concerned with simulations of positive and negative corona discharges in dry air at atmospheric pressure in a wire-cylinder gap. The 1D-axisymmetric model was implemented using the COMSOL Multiphysics platform and the considered hydrodynamic plasma model comprises 12 charged species and 32 chemical reactions. The conservation equation for electrons and momentum conservation equation for ions are solved coupled with the Poisson equation, under the local-field approximation (the electron transport and kinetic coefficients are assumed to be dependent on the local reduced electric field E/N only). The discharge is triggered by applying a step voltage with maximum of 25 kV and waiting for a steady-state to be reached, considered when the density distribution of charged species no longer changes beyond a certain time of the order of microsecond. The authors have also simulated the effect of gas pressure and temperature on the distribution of the electron density and discharge current; it is shown that the rise of temperature causes a rapid increase in the density of electrons in negative corona whereas the increase is slower in positive corona, and also an increase in discharge current; the increase in pressure has an inverse influence on the current and the electron density.

In [59] it was proposed an approximate approach for the study of needle electrode corona discharges in atmospheric air in a large-scale space. The approximations are suited for a large gap width being considered (25 cm). The approach is based on finding an equipotential surface slightly bigger than the ionization region, where continuity of charged particle density and electric field is ensured. A hydrodynamic fluid model, consisting of the Poisson equation and three conservation equations of charged particles, is solved in the ionization region in the vicinity of the needle electrode. The obtained charged particle distribution on the equipotential surface is assigned as a boundary condition for the outer region (the drift zone), where the ion conservation equation is solved jointly with the Poisson equation. The fluid model does not take into consideration the process of photoionization, which was regarded as having little influence on the charged particle distribution, and the diffusion component of ions fluxes was neglected. For a given applied voltage on the corona electrode, the simulation was run for 1 ms in order to reach a steady-state solution. Simulation results were compared with experiments performed by the authors and a good agreement was found, demonstrating the accuracy and feasibility of the proposed approach for large-scale space corona discharges with a needle electrode.

1.3 This work

As shown in the preceding sections, there is a vast literature on the physics of low-current and corona discharges and a number of useful theoretical results, including analytical ones, have been obtained under various approximations. Also, there are several well developed general-use numerical codes which allow modelling the ignition and dynamics of low-current discharges, including the ignition and breakdown voltages. The vast majority employ time-dependent solvers. Although stationary solvers are available, e.g. the Plasimo code [15], their use is rarely seen. As a consequence, modern numerical codes for modelling low-current high-pressure gas discharges are too heavy computationally to be routinely used in engineering practice, and the hold-off voltage in high-voltage devices is usually estimated by evaluating the ionization integral given in Eq. (1.8). Thus, there is a gap between modern methods of numerical modelling of low-current gas discharges and engineering approaches, which is desirable to reduce.

Time-dependent solvers give detailed information on spatio-temporal distributions of plasma parameters and are indispensable for studies of discharges with fast temporal variations, such as high-frequency discharges, pulsed discharges, streamer and spark discharges, etc., e.g., [1, 2]. On the other hand, some discharges are quasi-stationary: DC and low-frequency (e.g., 50 Hz) discharges, where the applied voltage varies in time much slower than the ions drift. As an example, taking typical mobilities of 2 $\times 10^{-4}\,\mathrm{m^2\,V^{-1}\,s^{-1}}$ for ions in atmospheric pressure air, at the temperature of 300 K, and a reduced electric field of 50 Td, one finds that the time of ion drift over a gap of 10 mm is about 0.04 ms, which is much shorter than the quarter-period of variation of the 50 Hz applied voltage (5 ms). Hence, breakdown in 50 Hz electric fields is preceded by a pre-breakdown discharge that is essentially quasi-stationary. As noted above, in the work [20] the DC inception field of corona in the spherical geometry is on average only $3-4\%$ higher or lower (for positive and negative corona respectively) when compared to the low-frequency AC field.

Up to now, such quasi-stationary discharges are simulated by means of time-dependent solvers: an initial state of a discharge is specified and its relaxation over time is followed until a steady state has been attained. An alternative is to use stationary solvers, which solve steady-state equations describing a stationary discharge by means of an iterative process unrelated to time relaxation. Stationary solvers offer important advantages in simulations of steady-state discharges. In particular, they are not subject to the Courant–Friedrichs–Lewy criterion or analogous limitations on the mesh element size and they allow decoupling of physical and numerical stability. The removal of limitations on the mesh element size allows one to speed up simulations, with huge improvement in some cases, by orders of magnitude, and is particularly important for modelling of discharges with strongly varying length scales, e.g., corona discharges, where a variation of the mesh element size by orders of magnitude is indispensable. The first step in this direction was taken in the work [57] by eliminating the constraint on the time step imposed by the electron drift time; however, the ion conservation equation included the time-dependent term, hence the constraint imposed by the ion drift time remained. Although no mention was made concerning the efficiency of simulations, the authors [42] solved stationary 1D equations within the scope of a simplified model.

In face of the above, it is beneficial to develop an approach for simulation of low-current discharges with the use of stationary solvers, being applicable not only to DC but also to low-frequency discharges. The main goals of this work are to develop such approach, to implement it as a part of a numerical model of low-current quasi-stationary discharges in high-pressure air, to validate the developed model against experimental data over a wide range of conditions, and to apply it to several problems of high scientific and technological interest. Firstly, the inception of discharges in high-pressure air will be investigated over a wide range of conditions. The method developed can be used as a predictor of the hold-off voltage in high-voltage devices, as well as to evaluate the sensitivity of the ignition voltage with respect to different factors (the kinetic scheme used, the photoionization, and the secondary electron emission from the cathode). The second problem to be studied is the effect that anode surface protrusions can have on pre-breakdown discharges in high-pressure air, which can be considered as an indirect evidence of the possible existence of microprotrusions on the electrode surface. The third problem concerns investigation of characteristics of DC corona discharges in a wide range of currents and gap widths.

The research leading to this thesis was conducted at the Department of Physics of Universidade da Madeira and at the Research Node of Instituto de Plasmas e Fusão Nuclear (Instituto Superior Técnico, Universidade de Lisboa, Lisbon, Portugal) at Universidade da Madeira, in collaboration with Professor George Naidis in the role of a consultant, of the Joint Institute for High Temperatures, Russian Academy of Sciences, Moscow, Russian Federation. The work was performed within activities of the research project PlasMa-M1420-01-0145-FEDER-000016, co-financed by the Operational Program of the Autonomous Region of Madeira 2014-2020. A part of the work was supported by a research grant from Corporate Technology of Siemens AG (Erlangen, Germany). A part of the work was performed in collaboration with colleagues of the Institute of High Current Electronics, Tomsk, Russian Federation. The most part of the thesis is a compilation of papers already published [5, 60–62]. The author of the thesis performed one of the simulation examples shown in [63], and this material is included in the thesis.

The text is organized in six chapters. The first chapter is this Introduction.

In chapter 2, the numerical model of low-current quasi-stationary discharges in high-pressure air, comprising equations of conservation and transport of charged species and the Poisson equation, is presented. A 'minimal' kinetic model of plasmachemical processes in low-current discharges in high-pressure air is used, which takes into account electrons, an effective species of positive ions, and three species of negative ions (O_2^-, O^-, and O_3^-). The mathematical problem formulated is solved with the use of stationary solvers, which offer important advantages in simulations of steady-state discharges compared to standard approaches that rely on time-dependent solvers.

In chapter 3, corresponding to [60], the model is validated by comparison between the computed discharge ignition voltage and several sets of experimental data on glow coronas, or sparkover when a corona discharge was not prior observed. A good agreement with the experiment has been obtained for positive coronas between concentric cylinders in a wide range of pressures and diameters of the cylinders. The sensitivity of the computation results with respect to different factors, e.g. the kinetic scheme used, the photoionization, and the secondary electron emission from the cathode, is illustrated. Inception voltages of negative discharges, computed using the values of the secondary electron emission coefficient of 10^{-4} to 10^{-3}, agree well with the experimental data. A simplified kinetic model for corona discharges in air, which does not include conservation equations for negative ion species, is proposed and validated. Modelling of positive coronas in rod-to-plane electrode configuration has been performed and the computed inception voltage was compared with experimental data.

Chapter 4, corresponding to [62], begins with an overview of deviations of measured breakdown voltage in parallel-plate gaps from Paschen's curve, observed in microgaps and at very high pressures, $p \gtrsim 5\,\mathrm{bar}$ ($5 \times 10^5\,\mathrm{Pa}$), which can be described in the same way as deviations of field electron emission from cold cathodes in vacuum from the Fowler-Nordheim formula, i.e., in terms of enhancement of electron emission. A simplified 1D modelling with account of field electron emission from the surface of the negative electrode is used to describe the deviations. An alternative explanation for deviations from Paschen's curve at very high pressures is specifically related to the supposed existence of microprotrusions on the electrode surfaces, which cause enhanced ionization of neutral gas in regions near protrusions; this alternative is explored by means of 2D numerical modelling. In particular, results of simulations are compared with deviations from the similarity law observed at very high pressures in corona inception and breakdown voltages for discharges on positive cylindrical electrodes of small radii [9, 64]: cathodic phenomena are irrelevant and enhanced ionization of neutral gas in regions near protrusions on the anode surface appears to be the only possible explanation. Conical or cylindrical protrusions on the surface of the inner electrode are studied. A qualitative agreement with the experiment in all the cases could be achieved for protrusion heights of the order of $50\,\mu$m.

In chapter 5, corresponding to [5, 61, 63], time-averaged characteristics of DC corona discharges are investigated of DC corona discharges between concentric cylinders and point-to-plane gaps in ambient air. A wide range of currents of both voltage polarities is investigated first in the case of 1D concentric cylinders, which is also typically found in the literature, and then in point-to-plane gaps with various gap widths where all relevant geometrical parameters of the point electrode are known. The simulation results are compared with experimental results. The validity of the classic Townsend-Kaptzov assumption, which states that the steady state electric field at the conductor surface remains at the corona onset value, is investigated in negative corona discharges in an axially symmetric wire-cylinder gap; contrary to a recent work [44], which disputed the mentioned assumption at high currents based in a recent nonintrusive measurement method, the electric field induced second harmonic generation (E-FISHG), it is shown that the electric field at the wire remains at the corona inception level, in agreement with the Townsend-Kaptzov assumption. For the case of point-to-plane gaps, comparisons between computed and experimental spatial distributions of the radiation intensity are also performed. Specific features of the numerical and experimental results at both polarities are discussed.

In chapter 6 conclusions of this work are given and possible directions of future research discussed.

All the modelling results included in this thesis were obtained using COMSOL Multiphysics.

Chapter 2

The model

The goal of the thesis to reduce the gap between engineering approaches and modern methods of numerical modelling of low-current gas discharges, led to the development of an approach for simulation of such discharges with the use of stationary solvers, applicable to DC and low-frequency discharges. The numerical model of low-current quasi-stationary discharges in air at pressures of the order of atmospheric and higher, used in this thesis, is presented in this chapter.

The outline of the chapter is as follows. The equations and boundary conditions included in the model are presented in section 2.1. In section 2.2, the kinetic scheme of plasmachemical processes is introduced. The relevant numerical aspects are discussed in section 2.3.

2.1 Equations and boundary conditions

The model comprises equations of conservation and transport of charged species, written in the drift-diffusion approximation, and the Poisson equation:

$$\nabla \cdot \mathbf{\Gamma}_\alpha = S_\alpha \quad (\alpha = e,\, O_2^+,\, O_2^-,\, O^-,\, O_3^-). \tag{2.1}$$

$$\varepsilon_0 \nabla^2 \phi = -e \sum_\alpha Z_\alpha n_\alpha. \tag{2.2}$$

$$\mathbf{\Gamma}_\alpha = -D_\alpha \nabla n_\alpha - Z_\alpha n_\alpha \, \mu_\alpha \nabla \phi. \tag{2.3}$$

Here subscript α identifies charged species; n_α, $\mathbf{\Gamma}_\alpha$, D_α, μ_α, S_α, and Z_α are, respectively, number density, density of transport flux, diffusion coefficient, mobility, net volume rate of production, and charge number of species α; ϕ is the electrostatic potential; e is the elementary charge; and ε_0 is the permittivity of free space. The charged species included in the model are the electrons, one species of positive ions, which are represented mostly by O_2^+, and the negative ions O_2^-, O^- and O_3^-. The conservation equations, Eq. (2.1), are written for the steady-state case. Equations of transport of charged species, Eq. (2.3), are written in the local-field approximation, i.e., with the electron transport and kinetic coefficients being assumed to depend only on the local reduced electric field. This assumption is valid when the macroscopic length scale is much larger than the relevant microscopic scale (mean free path for ions and electron energy relaxation length for electrons), and particularly for high pressure discharges where non-local effects tend to be less important due to the very frequent collisions between particles.

As an order-of-magnitude estimate, for atmospheric pressure air at ambient temperature, with critical field of about $25\,\mathrm{kV\,cm^{-1}}$, and considering a characteristic distance for ion diffusion (the scale over which the ion density changes) of 1 mm, the ratio between the diffusion and drift components of the ion flux is of the order of 10^{-5}. For this reason, diffusion of charged species along the direction of the electric field is a minor effect except in the vicinity of the electrodes, however it can be significant in the transversal direction. For completeness, diffusion should be included in the modelling, with advantages concerning numerical computations since in mathematical terms the density gradient, which appears in the diffusion term of conservation equations, yields to standard second order equations, easier to solve and couple with the rest of equations.

The source terms S_α in equations for electrons and positive ions include, in addition to terms describing production of these species in collisional processes, the photoionization term S_{ph}. The latter is evaluated by means of the three-exponential Helmholtz model [65]:

$$S_{ph}(\mathbf{r}) = \sum_{j=1}^{3} S_{ph}^{(j)}(\mathbf{r}), \tag{2.4}$$

with each of the terms satisfying the Helmholtz partial differential equation,

$$\nabla^2 S_{ph}^{(j)}(\mathbf{r}) - (\lambda_j p_{O_2})^2\, S_{ph}^{(j)}(\mathbf{r}) = -A_j p_{O_2}^2 I(\mathbf{r}) \quad (j = 1, 2, 3). \tag{2.5}$$

Here A_j and λ_j are constants (parameters of the three-exponential fit function) given in [65], p_{O_2} is the partial pressure of molecular oxygen, and $I(\mathbf{r})$ is the product of ξ the probability of ionization of a molecule at photon absorption and the local photon production rate. The latter is assumed to be proportional to the rate of ionization of neutral molecules by electron impact, $S_i(\mathbf{r})$, and $I\,(\mathbf{r})$ is written as

$$I(\mathbf{r}) = \xi \frac{p_q}{p + p_q} \frac{\nu_u}{\nu_1} S_i(\mathbf{r}), \tag{2.6}$$

where p is the neutral gas pressure, $p_q/\left(p + p_q\right)$ is a quenching factor that accounts for the probability of non-radiative de-excitation of nitrogen molecules due to collisions with other molecules, ν_u is the frequency of electron impact excitation of radiating states producing ionizing photons, and ν_1 is the electron impact ionization frequency.

Following [30, 66], the quenching pressure p_q is set equal to 30 Torr (4×10^3 Pa) and the product $\xi\nu_u/\nu_1$ is expressed in terms of the the reduced electric field E/N:

$$\xi\frac{\nu_u}{\nu_1} = 0.03 + \frac{15.7\,\mathrm{Td}}{E/N}. \tag{2.7}$$

Boundary conditions are written in the conventional form. At the cathode, the electrons are emitted from the surface with the effective secondary emission coefficient γ; the diffusion flux of the attracted particles (the positive ions) is neglected in comparison with the drift flux; the negative ions are repelled by the electric field and thus their number density is defined by the chaotic flux (note that a factor of 1/2 is used instead of the usual 1/4, since it appears to be more appropriate near an absorbing non-emitting surface, where the velocity distribution function is strongly anisotropic [67]); the electrostatic potential is set equal to zero; the rate of photoionization is set to zero:

$$(\mathit{\Gamma}_e)_n = -\gamma\left(\mathit{\Gamma}_{\mathrm{O}_2^+}\right)_n, \quad \frac{\partial n_{\mathrm{O}_2^+}}{\partial n} = 0, \quad (\mathit{\Gamma}_\alpha)_n = \frac{n_\alpha}{2}\sqrt{\frac{8kT_\alpha}{\pi m_\alpha}} \quad (\alpha = \mathrm{O}_2^-,\, \mathrm{O}^-,\, \mathrm{O}_3^-), \tag{2.8}$$

$$\phi = 0, \quad S_{ph}^{(j)} = 0. \tag{2.9}$$

Here and further k is Boltzmann's constant, m_α and T_α are the mass and temperature of species α, respectively, and n is a direction locally orthogonal to the boundary of the computation domain (the cathode surface, in this case) and directed outward of the domain.

At the anode, the diffusion flux of the attracted particles (the electrons and the negative ions) is neglected in comparison with the drift flux; the positive ions are repelled by the electric field and thus their number density is defined by the chaotic flux; the electrostatic potential is fixed at some value U; the rate of photoionization is set to zero:

$$\frac{\partial n_\alpha}{\partial n} = 0 \quad (\alpha = e,\, \mathrm{O}_2^-,\, \mathrm{O}^-,\, \mathrm{O}_3^-), \quad \left(\mathit{\Gamma}_{\mathrm{O}_2^+}\right)_n = \frac{n_{\mathrm{O}_2^+}}{2}\sqrt{\frac{8kT_{\mathrm{O}_2^+}}{\pi m_{\mathrm{O}_2^+}}}, \quad \phi = U, \quad S_{ph}^{(j)} = 0. \tag{2.10}$$

Results reported in this chapter refer to two corona discharge configurations: a one-dimensional corona between concentric cylinders and a two-dimensional corona in the rod-to-plane gaps. Boundary conditions at the boundaries limiting the computation domain need to be specified for the rod-to-plane configuration: the so-called natural boundary conditions (zero normal derivatives) for all dependent variables (n_α, ϕ, $S_{ph}^{(j)}$) were used.

It should be mentioned that slightly different forms of the boundary conditions have been used in chapters 4 and 5. In chapter 4, the boundary condition for electrons at the cathode takes into account, in addition to the secondary electron emission, electron losses to the cathode due to the chaotic motion, and field emission, being written as:

$$(\mathit{\Gamma}_e)_n = -\gamma \left(\mathit{\Gamma}_{O_2^+}\right)_n - \frac{n_e \bar{C}_e}{2} + \mathit{\Gamma}_{em}$$

Here $\bar{C}_e = \sqrt{8kT_e/\pi m_e}$ is the mean speed of the electrons, and $\mathit{\Gamma}_{em}$ is the flux density due to field emission.

In chapters 4 and 5, the number densities of the repelled particles (negative ions at the cathode and positive ions at the anode) were set equal to zero ($n_\alpha = 0$), instead of being defined by the chaotic flux. We note that the effect of this change on the solution was insignificant, which increases the reliability of the results, given that this boundary condition cannot be formulated in an exact way [67].

2.2 Kinetics

Concerning the kinetic scheme of plasmachemical processes, very complex and accurate models exist for describing the composition of air plasmas. For e.g., in [68] a kinetic model is proposed for ion–molecular processes involving charged particles of a humid air plasma produced by a fast electron beam, which includes more than 600 processes involving electrons and 41 positive and 14 negative ions, including hydrated ions. In addition, a significant amount of high-quality data for evaluation of transport and kinetic coefficients and solvers, generating these coefficients, e.g., LXCat [69] and [13], is available. However, the numerical implementation of such complex models is very time-consuming, and it is very hard to simulate, if even possible, by means of a finite element method comprising equations of conservation and transport of charged species with drift-diffusion approximation. In agreement with the goals expressed in Introduction, section 1.3, a 'minimal' kinetic model is presented and detailed in Appendix A. Briefly, the plasmachemical processes include: electron impact ionization (reaction 1, $e+M \to 2e+A^+$), two-body (dissociative) attachment (2, $e+O_2 \to O^- + O$), three-body attachment (3, $e + O_2 + M \to O_2^- + M$), photoionization (4, $M + h\nu \to e + A^+$), collisional detachment from O_2^- (5, $O_2^- + O_2 \to e + 2O_2$), associative detachment from O^- (6, $O^- + N_2 \to e + N_2O$), charge transfer from O^- to O_2^- (7, $O^- + O_2 \to O + O_2^-$), conversion of O^- to O_3^- (8, $O^- + O_2 + M \to O_3^- + M$), and ion-ion (9, $A^+ + B^- \to$ products) and electron-ion recombination (10, $A^+ + e \to$ products). The transport and kinetic coefficients were evaluated as explained in Appendix A. The modelling of this thesis is aimed primarily at computing the discharge ignition voltage and the neutral gas is still cold at the discharge ignition, hence the neutral gas temperature is set equal to 300 K.

2.3 Numerical aspects

The numerical implementation is based on the use of stationary solvers, which, as already discussed in the Introduction, offer important advantages in simulations of quasi-stationary discharges compared to time-dependent solvers. The computational platform COMSOL Multiphysics® was used. The following interfaces were employed: Electrostatics (the Poisson equation (2.2)), Coefficient Form (the Helmholtz equations), and Transport of Diluted Species, so-called TDS (the species conservation equations (2.1), supplemented with the transport equations (2.3), which were formulated in logarithmic variables, i.e., new dependent variables $N_\alpha = \ln n_\alpha$ have been introduced). The logarithmic formulation ensures that the number density of any of the species is never negative and is frequently used in the modelling of cold gas discharges. The species conservation equations were supplemented with the consistent streamline upwind Petrov-Galerkin weighted residual stabilization. As another stabilization means, artificial source terms C/n_α were added to S_α on the right-hand side (rhs) of equations (2.1). The constant C was scaled to ensure that these terms do not affect the solution, while still ensuring the convergence of the iterations. The reactions considered within the kinetic scheme were taken into account as production/loss terms in the TDS interface.

An important aspect of the developed approach for simulation of low-current discharges is computing the voltage corresponding to the initiation of a self-sustaining discharge (the ignition voltage) for each discharge geometry over a wide range of gas pressures. A natural control parameter in the modelling is the discharge voltage U. However, at low discharge currents I the discharge voltage remains virtually the same (and very close to the inception voltage) as current varies over orders of magnitude. In this situation, the discharge current is a more suitable control parameter than the voltage. Therefore, the model allowed both discharge voltage or current serving as a control parameter, with switching between these two parameters in an easy and seamless way. The latter was implemented with the use of the Weak Form interface in COMSOL Multiphysics. The solution computed for each value of the discharge voltage or current was used as an initial approximation for the computation with the next value; hence there is the need of finding a suitable initial approximation for the first computed solution, which is a delicate point when using stationary solvers. In this thesis, numerical simulation of each electrode configuration comprised the following procedure, as depicted in figure 2.1. The first step is to find a solution describing

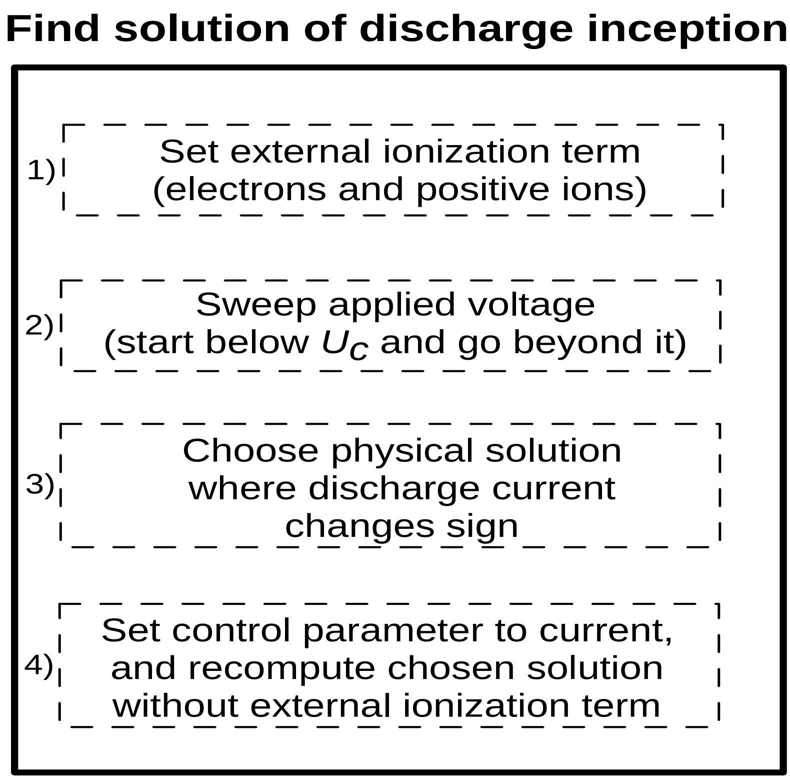

Figure 2.1: Flowchart of the resonance method summary, used to find a solution describing the discharge inception.

the discharge inception, using the eigenvalue approach developed in [63]. Briefly, a term describing an artificial external ionization source is added to equations (2.1) for the electrons and the positive ions. The effect of this term is the existence of a non-trivial solution (i.e., a solution with non-zero densities of the charged particles) for applied voltages below the inception voltage U_c. A steady-state solution is found for the applied voltage that is supposed to be just below U_c and the corresponding value I_0 of the discharge current is computed. After this first step, the control parameter is switched to the discharge current, which is fixed at $I = I_0$. The external ionization source term is then removed from the equations and the solution is recomputed. Thus the first steady-state solution, which describes the corona discharge for $I = I_0$, is obtained. The corresponding discharge voltage represents the inception voltage U_c. This solution can be used as the initial approximation for any subsequent simulations in which parameters of interest (e.g., the plasma pressure, in chapters 3 and 4, or the discharge current, in chapter 5) are varied.).

Chapter 3

Simulation of discharge inception in high-pressure air

3.1 Introduction

This chapter contains the first example of application of the developed approach for simulation of low-current discharges in high-pressure air. The developed numerical model, based on the use of stationary solvers, is validated by comparison of inception voltage of low-current discharges, computed in a wide range of conditions, with experimental data on inception of glow coronas, or sparkover when a corona discharge was not prior observed. The model gives the minimum voltage required for discharge ignition, corresponding to the condition of reproducibility of the charged species inside the discharge gap. The problems of stability and transitions between the corona modes and the inception of a pulse corona can be treated with the use of the presented plasmachemical model and a combination of stationary and time-dependent solvers as described in [70]; eigenvalue solvers may be helpful as well.

Corona discharges occur in strongly non-uniform fields at voltages insufficient to cause the breakdown. In negative corona discharges, the primary electrons are generated mainly by the secondary electron emission from the cathode. The electric field in positive coronas is very weak at the cathode, meaning that secondary electron emission is a minor process. Additionally, the emitted electrons will be attached to oxygen molecules in the drift zone before arriving to the anode. Therefore, the primary electron generation in positive coronas is ensured by photoionization. This process consists of highly energetic photons ionizing neutral molecules in the gas near the edge of the active zone.

The outline of the chapter is as follows. In section 3.2, results of computation of discharge ignition voltage in the concentric-cylinders configuration are given and compared with the experiment. The sensitivity of the computation results with respect to different factors is illustrated. A simplified model with local kinetics of negative ions is presented in section 3.3. In section 3.4, results on inception voltage of positive coronas in the rod-to-plane electrode configuration are given. Concluding remarks are given in section 3.5.

Results reported in this chapter were published in [60].

3.2 Corona between concentric cylinders

A number of experiments on inception of glow corona in air are reported in the literature; e.g., [8, 71–75]. Typical electrode configurations are concentric cylinders and point-to-plane. Results of computation of inception of corona between concentric cylinders under conditions of experiments [71, 72] are reported in this section. Experimental results on the inception voltage U_c in this geometry are conventionally reported in terms of the corona inception field strength E_c, which is related to the inception voltage as

$$E_c = \frac{U_c}{r_0 \ln (R/r_0)}, \tag{3.1}$$

where r_0 and R are the radii of the inner and outer cylinders, respectively. The same relation is used in order to determine the inception field in the modelling. The discharge current I was set equal to 1 nA per centimeter of the cylinder length, which is sufficiently small for the discharge voltage computed to be independent of I and thus to be considered as the corona inception voltage U_c. The effective secondary electron emission coefficient γ was set equal to zero unless specified otherwise.

In the case of positive corona, where the smaller electrode (the inner cylinder) plays the role of anode and the larger electrode (the outer cylinder) is a cathode, the discharge is generally stable and the reproducibility of experimental data is better than for negative coronas. Therefore, positive glow coronas are more suitable for validation of quasi-stationary theoretical models.

In figure 3.1, values of the reduced inception field of a positive corona computed in a wide range of conditions are plotted as a function of pr_0 along with experimental data [71, 72]. The agreement between computed and measured inception field is quite good, except for a small deviation between the dashed line and squares appearing in the range $pr_0 \gtrsim 0.1$ atm cm (which corresponds to the pressure range from 10 to 35 atm (1.01×10^6 to 3.55×10^6 Pa)).

There is a visible difference in figure 3.1 in the range $pr_0 < 0.1$ atm cm (1.01×10^4 Pa cm) between the experimental data [71] for the same pr_0 referring to the two different r_0 values. This effect is caused by a decrease of photoionization rate with

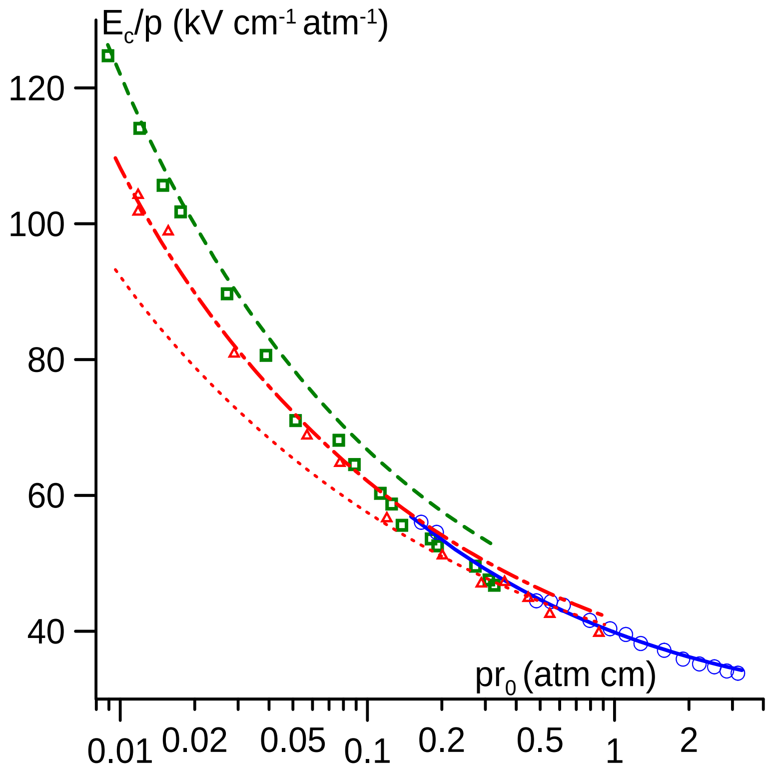

Figure 3.1: Reduced inception field at the surface of positive wire electrode. Circles and solid line: experimental data [72] and the corresponding modelling, $p = 1\,\mathrm{atm}$, $2R = 58.1\,\mathrm{cm}$, varying inner cylinder diameter $2r_0$. Triangles and dash-dotted line: experimental data [71] and the corresponding modelling, $2r_0 = 0.239\,\mathrm{cm}$, $2R = 9.75\,\mathrm{cm}$, varying pressure. Squares and dashed line: experimental data [71] and the corresponding modelling, $2r_0 = 0.0178\,\mathrm{cm}$, $2R = 9.75\,\mathrm{cm}$, varying pressure. Dotted line: modelling with the normal derivative of the rate of photoionization set to zero at the electrodes, $2r_0 = 0.239\,\mathrm{cm}$, $2R = 9.75\,\mathrm{cm}$, varying pressure.

growth of pressure, originating in collisional quenching of nitrogen radiating states (a detailed discussion of this topic is given in [30]). Let us consider an illustrative example. At $pr_0 = 0.03\,\mathrm{atm\,cm}$ ($3.04 \times 10^3\,\mathrm{Pa\,cm}$), the gas pressure and the value of E_c/p are $3.37\,\mathrm{atm}$ ($3.41 \times 10^5\,\mathrm{Pa}$) and $88.93\,\mathrm{kV\,cm^{-1}\,atm^{-1}}$ for $2r_0 = 0.0178\,\mathrm{cm}$ and $0.25\,\mathrm{atm}$ ($2.53 \times 10^4\,\mathrm{Pa}$) and $81.01\,\mathrm{kV\,cm^{-1}\,atm^{-1}}$ for $2r_0 = 0.239\,\mathrm{cm}$. The value of E_c/p for $2r_0 = 0.0178\,\mathrm{cm}$ was recomputed with the pressure equal to $3.37\,\mathrm{atm}$ except in the evaluation of the photoionization term S_{ph}, where it was set equal to $0.25\,\mathrm{atm}$. The obtained E_c/p value was $83.23\,\mathrm{kV\,cm^{-1}\,atm^{-1}}$, which is much closer to the above-cited value of $81.01\,\mathrm{kV\,cm^{-1}\,atm^{-1}}$. Thus, the effect of pressure on the reduced inception field (at given pr_0), observed in the experiments, could hardly be explained without photoionization.

Modelling was performed also for the case where the boundary condition $S_{ph}^{(j)} = 0$

for the rate of photoionization at the inner cylinder or at both electrodes was replaced with the zero-derivative condition $\partial S_{ph}^{(j)}/\partial n = 0$, which amounts to neglecting losses of photons to the inner cylinder or both electrodes. The results of the two sets of modelling were quite close, meaning that the loss of photons on the outer electrode is a minor effect, which, of course, could be expected. These results are depicted in figure 3.1 by the dotted line. One can see that values of the inception field are sensitive to the choice of the boundary condition for photoionization at the anode for pressures $p \lesssim 1\,\mathrm{atm}$ ($1.01 \times 10^5\,\mathrm{Pa}$). For higher values of pressure, the effect of the boundary condition for photoionization at the anode is attenuated.

In figure 3.2, the experimental data [72] and the corresponding modelling results, which are shown in figure 3.1 by the open circles and the solid line, are replotted as functions of the diameter of the anode $2r_0$. The dashed line corresponds to E_c computed without account of detachment (reactions 5 and 6 in Table A.1 of Appendix A). The dash-dotted line in figure 3.2 depicts computations without account of attachment (reactions 2 and 3 of the same table). One can see that the disregard of detachment results in an increase of the inception voltage as it should. On the other hand, the dash-dotted line, computed without account of both attachment and detachment, is close to the solid one, which suggests that the detachment approximately compensates the attachment.

The above results refer to the secondary electron emission coefficient γ equal to zero. A relevant question is how sensitive the results are with respect to the value of γ. In figure 3.3, the reduced inception field computed with different values of γ for conditions of the experiment [71] is shown along with the experimental data. Note that the line corresponding to $\gamma = 0$ would coincide, to the graphical accuracy, with the (solid) line corresponding to $\gamma = 10^{-6}$ and therefore is not shown in the graph. As expected, the reduced inception field decreases with increase of γ. Good agreement with the experiments is seen for γ not exceeding 10^{-4}. Note that real values of γ in air seem to be of this order of magnitude for low E/p values at the cathode surface [76].

Also shown in figure 3.3 are simulations performed for $\gamma = 10^{-6}$ without account of photoionization. As expected, the disregard of photoionization causes an increase of the reduced inception field. The effect is stronger for low values of pr_0; for the same value of pr_0, the effect is stronger for lower pressures (figure 3.3a). There is an appreciable deviation of the inception field computed without account of photoionization from the experimental data.

The reduced inception field, computed without account of photoionization for two values of the secondary electron emission coefficient, $\gamma = 10^{-4}$ and 10^{-6}, is shown in figure 3.4. One can see that the effect of secondary electron emission turns more pro-

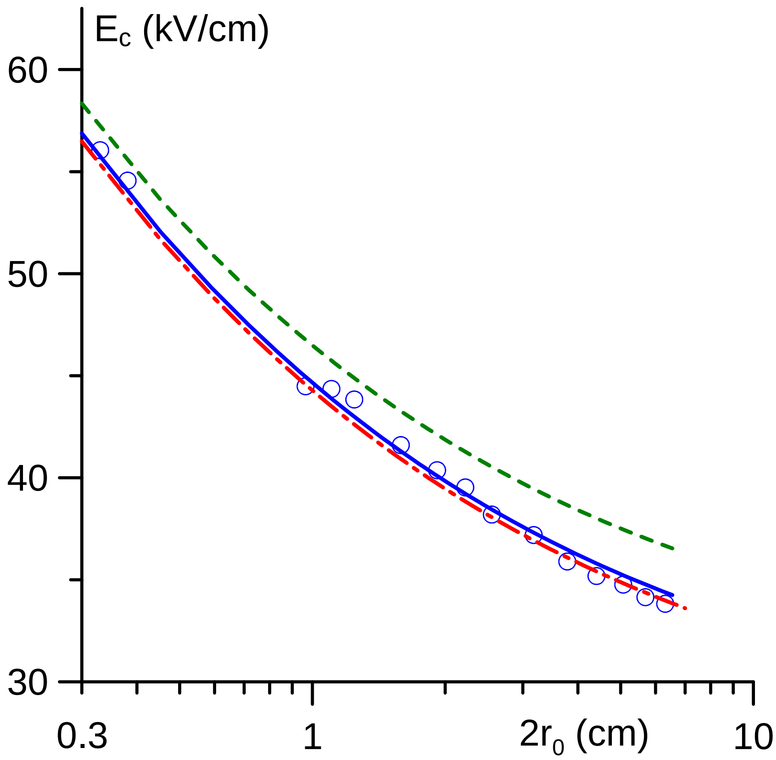

Figure 3.2: Inception field at the surface of positive wire electrode in atmospheric-pressure air. $2R = 58.1\,\mathrm{cm}$, varying inner cylinder diameter $2r_0$. Lines: computations with various kinetic schemes. Solid: kinetic scheme of table 1. Dashed: kinetic scheme without account of detachment process. Dash-dotted: kinetic scheme of table 1 with rates of attachment (reactions 2 and 3) set to zero. Circles: experimental data [72].

nounced if the photoionization is neglected, as it should. For $\gamma = 10^{-4}$, the deviation of the computed inception field from the experimental data is not very large. On the other hand, the reduced electric field, computed as a function of pr_0 without account of photoionization, does not reveal a dependence on pressure for both $\gamma = 10^{-6}$ and $\gamma = 10^{-4}$ (the solid and dashed lines in figure 3.4 are quite close, as well as the dotted and dash-dotted ones). One can conclude once again that the effect of pressure on the reduced inception field (at a given pr_0 value), observed in the experiments, could hardly be explained without photoionization.

The above results refer to positive coronas. In the case of negative coronas, a steady-state regime does not usually occur and current pulses are superposed on a DC current component, although the pulse component decreases with increasing voltage. Due to high electric fields at the surface of the smaller electrode, values of the secondary electron emission coefficient appropriate for negative coronas are higher than those for positive coronas and the secondary electron emission is likely to play a role.

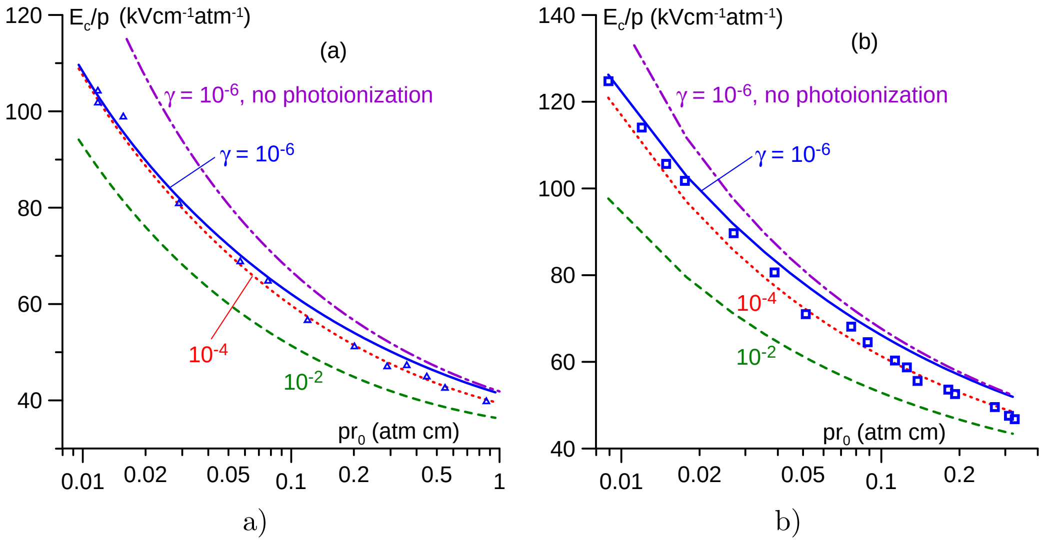

Figure 3.3: Reduced inception field at the surface of positive wire electrode. $2R = 9.75\,\text{cm}$, varying pressure. Lines: modelling with different values of the secondary electron emission coefficient γ. Dash-dotted: modelling with $\gamma = 10^{-6}$ without account of photoionization. Points: experimental data [71]. (a) $2r_0 = 0.239\,\text{cm}$. (b) $2r_0 = 0.0178\,\text{cm}$.

Hence, characteristics of negative corona depend on the cathode material, through the secondary electron emission coefficient, and on the state of the cathode surface. There is also a problem of identification of corona inception voltage in the experiment; e.g., [71]. Therefore, negative coronas are not suitable for validation of quasi-stationary models of corona discharges. On the other hand, the scatter of experimental data may be reduced by means of appropriate filtering, and it would be of interest to compare such filtered data with computation results.

In figure 3.5, experimental data on negative corona inception field, reported in [71], are shown. Note that in the experiments [71] the corona electrodes with the diameters of 0.0178 cm and 0.239 cm were made of tungsten and stainless steel, respectively. Also shown is the inception field computed using two values of the secondary electron emission coefficient γ, taken in agreement with [77]. One can see that the computed reduced negative corona inception field, considered as a function of pr_0, does not reveal a visible dependence on r_0 (or, equivalently, pressure), in agreement with the experiment. This contrasts the case of positive coronas, treated above, and is a consequence of the role of photoionization being minor for negative coronas. The same set of γ values, independent of pressure, allows one to evaluate the negative corona inception field, for both electrode radii and materials, in agreement with the experiment.

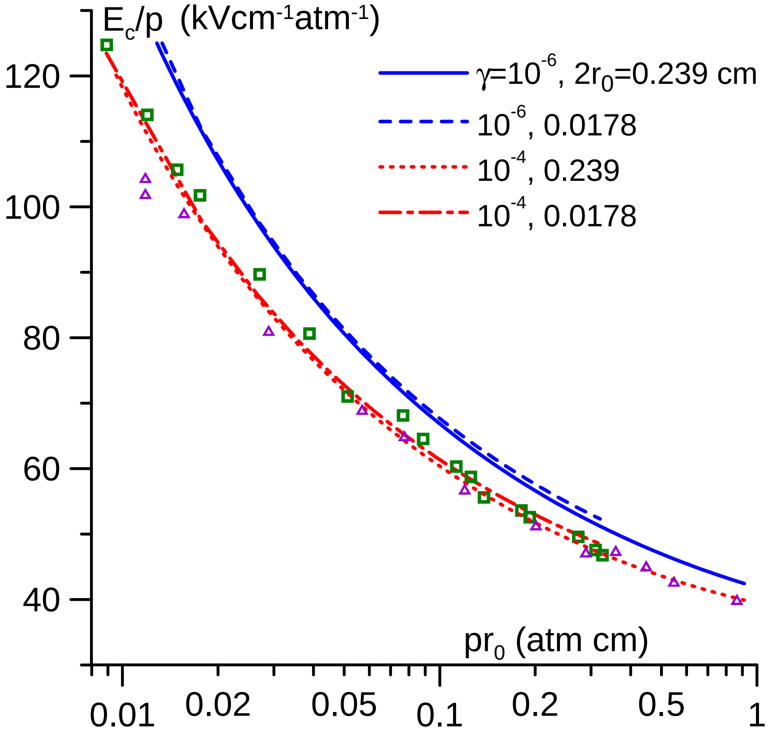

Figure 3.4: Reduced inception field at the surface of positive wire electrode. $2R = 9.75\,\mathrm{cm}$, varying pressure. Lines: modelling without account of photoionization with different values of the secondary electron emission coefficient γ and wire diameter $2r_0$. Points: experimental data [71] for $2r_0 = 0.239\,\mathrm{cm}$ (triangles) and $2r_0 = 0.0178\,\mathrm{cm}$ (squares).

3.3 Model with local kinetics of negative ions

In figure 3.6, frequencies of ion-molecule reactions, (reactions 5-8 in Table A.1 of Appendix A), are shown as functions of the reduced electric field. The frequencies are defined in the usual way, $\nu_5 = k_5 n_{\mathrm{O}_2}$, $\nu_6 = k_6 n_{\mathrm{N}_2}$, $\nu_7 = k_7 n_{\mathrm{O}_2}$, $\nu_8 = k_8 n_{\mathrm{O}_2} N$. The data shown in the figure refer to the plasma pressure $p = 1\,\mathrm{atm}$ ($1.01 \times 10^5\,\mathrm{Pa}$); for other pressures the frequencies ν_5 to ν_7 will be scaled proportionally to p and ν_8 proportionally to p^2. Note that the critical reduced electric field in the framework of the kinetic model considered is around 100 Td.

Let us consider also characteristic times of drift of the ions O_2^- and O^-: $t_i = l/\mu_i E$, where $i = \mathrm{O}^-$, O_2^- and l is a local characteristic length scale. Under conditions considered, l is of the order of $100\,\mu\mathrm{m}$ to $1\,\mathrm{mm}$ in the active zone and of $1\,\mathrm{cm}$ to $10\,\mathrm{cm}$ in the drift zone. The inverse of the characteristic times for $l = 1\,\mathrm{mm}$ are shown in figure 3.6.

The ions O^- are produced in reaction 2 and destroyed in reactions 6-8. One can see

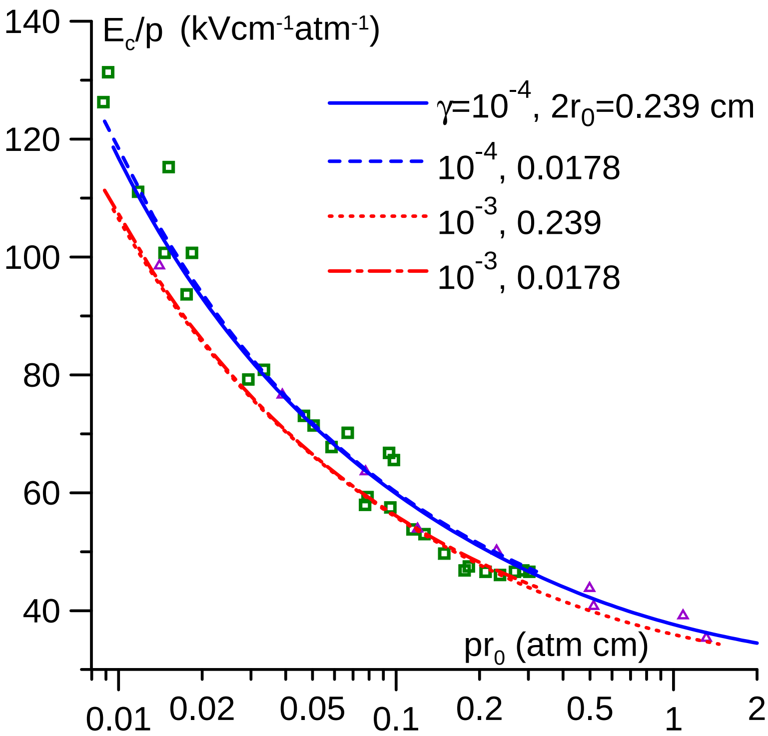

Figure 3.5: Reduced inception field at the surface of negative wire electrode. $2R = 9.75\,\text{cm}$, varying pressure. Lines: modelling with different values of the secondary electron emission coefficient γ and wire diameter $2r_0$. Points: experimental data [71] for $2r_0 = 0.239\,\text{cm}$ (triangles) and $2r_0 = 0.0178\,\text{cm}$ (squares).

from figure 3.6 that the sum of frequencies of these reactions, $\nu_6+\nu_7+\nu_8$, significantly exceeds $1/t_{\mathrm{O}^-}$. Hence, the left-hand side of the equation of conservation, equation (2.1), of the ions O^- may be neglected and this equation to the first approximation assumes the form of the equation of local balance

$$\nu_2 n_e = (\nu_6 + \nu_7 + \nu_8)\, n_{\mathrm{O}^-}. \tag{3.2}$$

The ions O_2^- are produced in reactions 3 and 7 and destroyed in reaction 5. One can see that the inequality $\nu_5 \gg 1/t_{\mathrm{O}_2^-}$ holds in the active zone and in the adjacent section of the drift zone. In this domain, the equation of conservation of ions O_2^- to the first approximation assumes the form of the equation of local balance

$$\nu_3 n_e + \nu_7 n_{\mathrm{O}^-} = \nu_5 n_{\mathrm{O}2^-}. \tag{3.3}$$

Using relations (3.2) and (3.3), one can show that

$$\nu_2 n_e + \nu_3 n_e - \nu_5 n_{\mathrm{O}_2^-} - \nu_6 n_{\mathrm{O}^-} = \frac{\nu_2 \nu_8}{\nu_6 + \nu_7 + \nu_8} n_e. \tag{3.4}$$

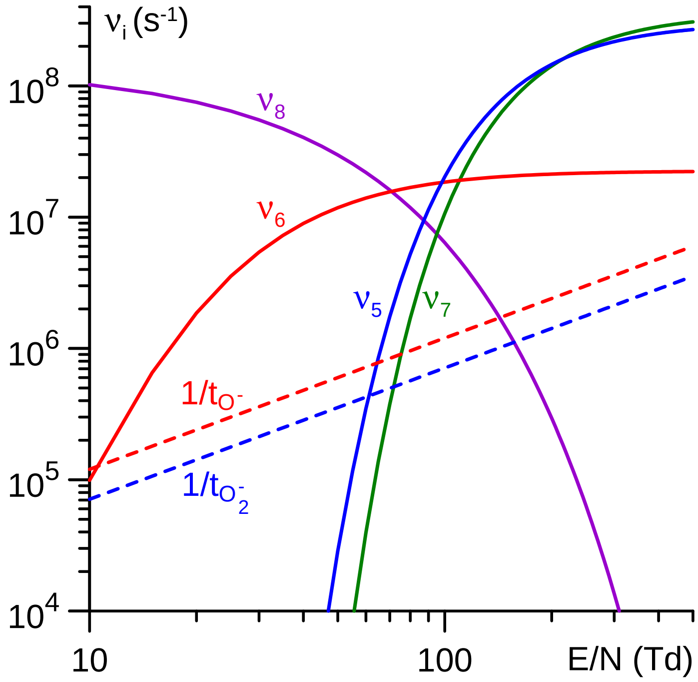

Figure 3.6: Frequencies of ion-molecular reactions (ν_5 - collisional detachment from O_2^-, ν_6 - associative detachment from O^-, ν_7 - charge transfer from O^- to O_2^-, ν_8 - conversion of O^- to O_3^-), and the inverse of the characteristic times of drift of the ions O_2^- and O^- as functions of the reduced electric field, $p = 1\,\text{atm}$.

The quantity on the rhs of relation (3.4) has the meaning of the effective attachment rate, which accounts for dissociative and three-body attachment, collisional detachment from O_2^-, associative detachment from O^-, charge transfer from O^- to O_2^-, and conversion of O^- to O_3^-. Using the Townsend coefficient η_2 of the two-body (dissociative) attachment, reaction 2, one can introduce also the effective Townsend ionization coefficient

$$\alpha_{\text{eff}} = \alpha - \eta_2 \frac{\nu_8}{\nu_6 + \nu_7 + \nu_8}. \tag{3.5}$$

The effective ionization coefficient defined by Eq. (3.5) is shown in figure 3.7 as a function of reduced field for two values of the plasma pressure $p = 1$ atm (1.01×10^5 Pa) and 10 atm (1.01×10^6 Pa). The critical reduced field, at which the effective ionization coefficient vanishes, equals 91 Td for $p = 1\,\text{atm}$ and 101 Td for $p = 10\,\text{atm}$ and increases with pressure. The reason for the latter is an increase in conversion of O^- ions to stable ions O_3^- at higher pressures. Note that values of critical reduced field obtained in [78] are 93 Td for $p = 1\,\text{atm}$ and 109 Td for $p = 10\,\text{atm}$. While the former value is close to the above-cited value obtained in this thesis, the difference in the values for $p = 10\,\text{atm}$ is more appreciable.

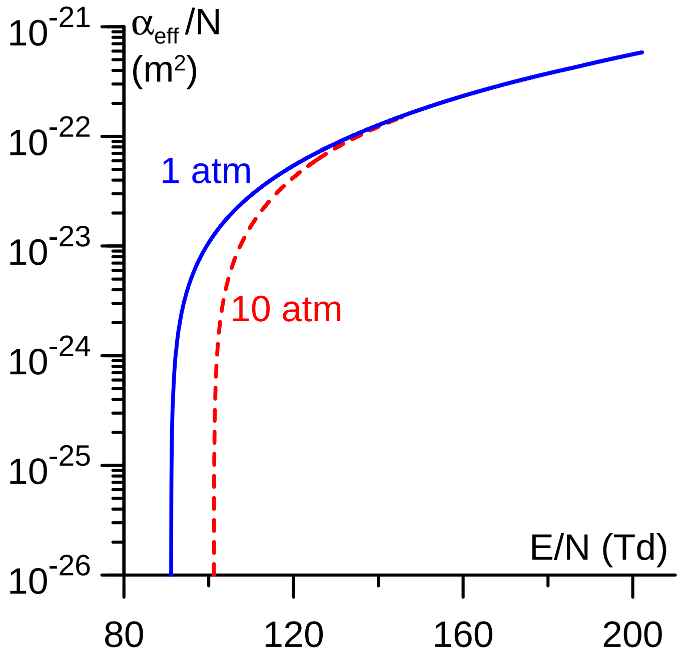

Figure 3.7: Effective ionization coefficient defined by Eq. (3.5) for two values of the plasma pressure $p = 1$ atm and 10 atm.

Thus, we have obtained a simplified model, which does not include equations of conservation of negative ion species and accounts for attachment and ion-molecular reactions by means of the effective attachment rate in the conservation equation for electrons: the model with local kinetics of negative ions. Simulations for the whole range of conditions of experiments [72] and [71], performed with the use of this model and with the use of the full model (including the conservation equations for all negative ion species), gave values of the inception field that are very close to each other (within 1% or so). This attests to the possibility of modelling discharge inception using the model with local kinetics of negative ions, with advantages in terms of computational costs.

In principle, the model with local kinetics of negative ions may be used also for evaluation of the ionization integral $K = \int \alpha_{\text{eff}}\, dr$ (the integration is extended over the active zone). As an example, we note that the ionization integral, evaluated for the inception voltage of positive corona under conditions of the experiment [71] with $2r_0 = 0.239\,\text{cm}$, varies from 6.7 for $p = 0.08\,\text{atm}$ $(8.11 \times 10^3\,\text{Pa})$ to 12.8 for $p = 17\,\text{atm}$ $(1.72 \times 10^6\,\text{Pa})$; values that agree well with estimates [30]. The ionization integral at inception of negative corona varies much less; for example, for $\gamma = 10^{-4}$ and $2r_0 = 0.239\,\text{cm}$ it equals 8.7 for $p = 0.08\,\text{atm}$ and 8.1 for $p = 17\,\text{atm}$. These values are not very different from $\ln\left(1 + \gamma^{-1}\right) \approx 9.2$, as could be expected. (Note that the

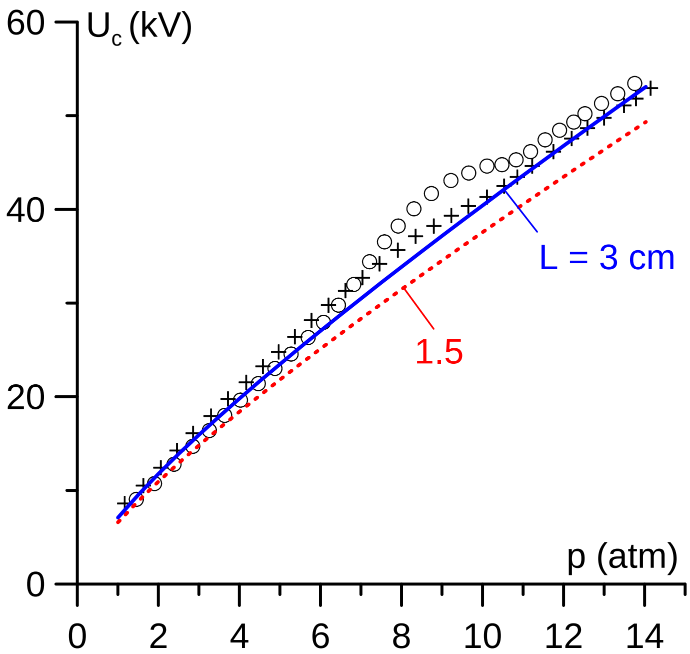

Figure 3.8: Positive corona inception voltage in rod-to-plane configuration. Hemispherically-tipped rod, diameter of 0.094 cm, 1 cm gap, plate diameter of 3.49 cm. Lines: modelling with different values of the rod length L. Points: experimental data [8] (two separate series of experiments).

difference can be due to ion currents being non-negligible at the edge of the active zone.)

3.4 Positive corona in rod-to-plane configuration

The computed inception voltages of the positive corona in the rod-to-plane configuration in air under the conditions of the experiments [8, 74] are shown in figures 3.8 and 3.9. (The simulations have been performed for the discharge current $I = 1\,\text{nA}$.)

The parameters of the experimental geometry, reported in [8, 74], are the rod and plate (cathode) diameters and the rod-to-plane distance (width of the discharge gap); the rod length is omitted. The latter is a typical situation: there seems to be no experimental publications where the rod length would be indicated.

For this reason, the modelling results shown in figures 3.8 and 3.9 refer to different values of the rod length L. These results show that, while the effect of the rod length on the inception voltage is not very strong, it is still quite appreciable, especially for large discharge gaps. Good agreement with the experimental data reported in [8, 74] is obtained for $L = 3\,\text{cm}$.

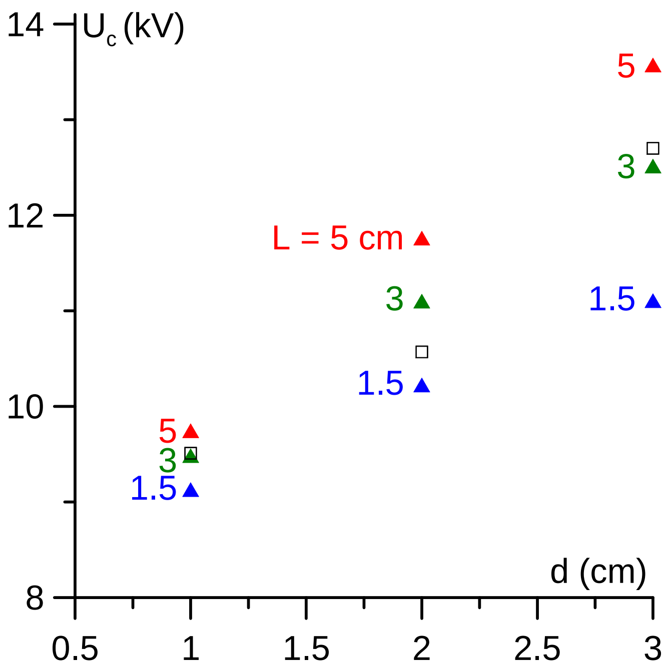

Figure 3.9: Positive corona inception voltage in rod-to-plane configuration. d: the gap width. Hemispherically-tipped rod, diameter of 2 cm, plate diameter of 7 cm, $p = 1$ atm. Triangles: modelling with different values of the rod length L. Squares: experimental data [74].

3.5 Concluding remarks

The first example of application of the developed approach for simulation of low-current discharges in high-pressure air was given. The model is implemented as a part of a numerical model of low-current quasi-stationary discharges in high-pressure air based on the use of stationary solvers, which offer important advantages in simulations of quasi-stationary discharges.

The numerical model developed is validated by a comparison of inception voltage of low-current discharges, computed in a wide range of conditions, with several sets of experimental data. A good agreement with experimental data has been obtained for positive coronas between concentric cylinders in a wide range of pressures and diameters of the cylinders, which attests to the suitability of the kinetics employed. The sensitivity of the computation results with respect to different factors is illustrated: the kinetic scheme used; the photoionization and a boundary condition for the photoionization rate at solid surfaces; the secondary emission from the cathode. It is shown, in particular, that the effect of pressure on the reduced inception field (at given pr_0), observed in the experiments, could hardly be explained without photoionization.

Computed ignition voltages of negative coronas depend on the value of the secondary electron emission coefficient γ, assumed in the modelling. The voltage computed with γ of 10^{-4} to 10^{-3} agrees well with the experimental data.

A simplified kinetic model for corona discharges has been proposed and validated. The simplified model does not include conservation equations for negative ion species and accounts for ion-molecular reactions by means of the effective attachment rate in the conservation equation for electrons. The ionization integral evaluated with the use of this model at corona inception voltage varies significantly for positive coronas; in the case of negative coronas, the ionization integral varies much less and is not very different from $\ln\left(1+\gamma^{-1}\right)$, as could be expected.

The computed inception voltage of positive glow coronas in the rod-to-plane electrode configuration qualitatively agrees with experimental data. The modelling results show that the inception voltage is affected by the rod length, a parameter omitted in experimental papers. A good quantitative agreement with the experiment can be obtained by variation of the rod length in the modelling.

Chapter 4

Effect of surface protrusions on pre-breakdown discharges in high-pressure air

4.1 Introduction

In this chapter, the model of plasmachemical processes in low-current discharges in high-pressure air is used for analysis of deviations from the similarity law, observed at high and very high pressures in experiments on discharge ignition and breakdown in corona-like configurations.

It is well known that current-voltage characteristics of field electron emission from cold cathodes in vacuum follow approximately the Fowler-Nordheim formula with the applied electric field being multiplied by the so-called field enhancement factor β, which is of the order of 10^2 or higher; e.g., reviews [79–81] and references therein. Various mechanisms for the enhancement have been postulated, the most popular being amplification of the applied (average) electric field by microprotrusions present on the cathode surface. The conventional problem with this hypothesis is that in order to explain the aforementioned values of the enhancement factor, the microprotrusions are assumed to be quite slender (needle-like), and such protrusions are not normally seen on electrode surfaces; e.g., section 3.1 of [79] and [81]. Another popular mechanism is a local reduction of the work function of the cathode material, caused by, e.g., lattice defects or adsorbed atoms. However, this effect seems to be insufficient to explain the observed values of the field emission current; e.g., [81, 82]. Other interesting hypotheses proposed in the literature include 'nonmetallic' electron emission mechanism [79] and enhancement of field emission by waves confined to the metal surface (plasmons) [81]. Thus, there is still no widely accepted understanding, in spite of several decades of

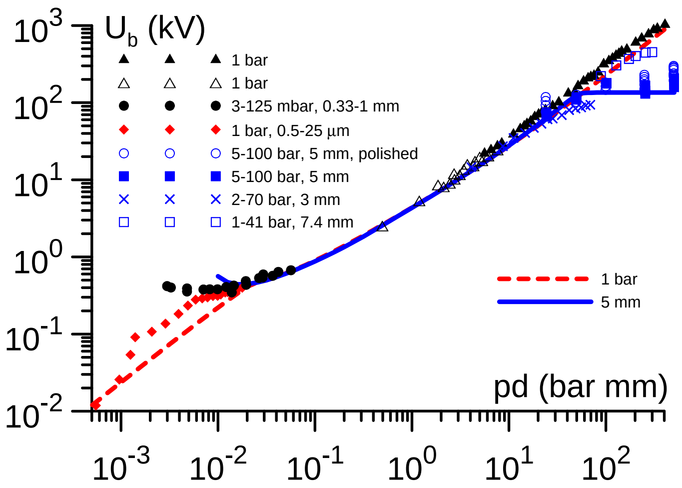

Figure 4.1: Breakdown voltage in uniform field in air for various air pressures p and gap widths d. Full triangles, open triangles, full circles: data from figure C1 of [22] (figure 5.23 of the book [10]). Diamonds: data from figure 6 of [83]. Open circles, full squares: data from figure 7 of [34]. Crosses: data from figure 15 of [84]. Open squares: data from figure 6 of [64]. Lines: modelling with account of enhanced field emission with $\beta = 50$. Adapted from [85].

active research, and this hinders the prevention of the vacuum breakdown in technical devices, e.g., in particle accelerators.

The effect of enhanced field emission from the cathode surface was considered also in gas discharge physics, in particular, in connection with deviations of measured breakdown voltage of parallel-plate gaps from Paschen's law. An example is shown in figure 4.1. Triangles and full circles represent measurements in medium gaps and pressures and constitute the well-known Paschen curve. Diamonds represent measurements in microgaps at atmospheric pressure; the breakdown voltage is substantially lower than the voltage determined by Paschen's law. Open circles, squares, and crosses represent measurements at very high pressures, which are substantially lower than the voltage determined by Paschen's law as well. Note that the experimental data [34] have been obtained in a concentric-cylinder geometry, rather than in the parallel-plate geometry as all the other data shown in figure 1; however, the cylinder radii (90 mm and 95 mm) were much larger than the gap width, thus the non-uniformity of the electric field was negligible.

Deviations from the Paschen curve occurring at atmospheric pressure in microgaps are important for operation of microelectromechanical and nanoelectromechanical systems and are under intensive investigation; e.g., [35, 49, 86–93]. Such deviations are conventionally described by introducing a field enhancement factor β into the Fowler–Nordheim field emission equation and estimating β by fitting experimental data on gas breakdown; e.g., values $\beta = 50$ and $\beta = 55$ are considered in [94] and [35, 49], respectively. As an example, results of computations [85] of the self-sustainment (breakdown) voltage with $\beta = 50$ are shown by the dashed line in figure 4.1 for $p = 1$ bar (1×10^5 Pa) over a wide range of gap widths d. (Note that the computations [85] have been performed by means of a model of low-current discharges in air, similar to the model described in chapter 2, but using parallel-plate geometry. The electron emission current was set equal to sum of the field emission current, evaluated with the electric field at the cathode surface enhanced by a factor of β and the work function of 4.5 eV, and the secondary electron emission with the effective coefficient of 10^{-4}. The voltage corresponding to the initiation of a self-sustaining discharge was computed, which for the parallel-plate geometry is usually assumed to coincide with the breakdown voltage.) As expected, the computed breakdown voltage follows Paschen's law for $d \gtrsim 20\,\mu$m and is below the Paschen values for smaller gap widths, in qualitative agreement with the experimental data.

Note that the field enhancement factor used in such-type macroscopic modelling is not the same as the one determined by fitting field electron emission currents from cold cathodes in vacuum by Fowler-Nordheim plots, which refers not to the entire cathode surface but rather to an 'emission area', extracted from the Fowler–Nordheim plot (e.g., [95]). On the other hand, the field enhancement factor determined by fitting field electron emission currents by the Fowler-Nordheim plots is usually much higher than the above-mentioned value of around 50, which should to a certain extent compensate the difference between the areas.

Deviations from the Paschen curve occurring at very high pressures, seen in figure 4.1 in the range $pd \gtrsim 50$ bar mm (5×10^6 Pa mm), have been known for several decades [84, 94, 96]: as the air pressure p in high-voltage air insulation systems increases, the breakdown voltage first increases proportionally to p, then the increase slows down and starting from pressures of the order of 10 atm (1.01×10^6 Pa) becomes very slow. Recent surge of interest in this topic [34, 97] is motivated by the possibility to use high-pressure air as a replacement for SF_6 for high-voltage insulation, due to removal of SF_6 from industrial applications for environmental reasons.

The early authors [84, 94, 96] hypothesized that the reason of these deviations is the field emission from the negative electrode enhanced by microononuniformities. Assuming this hypothesis, one can try to describe this effect in the same way as indicated above for the case of microgaps, i.e., by introducing a field enhancement factor β into the electron emission equation. As an example, the solid line in figure 4.1 depicts the breakdown voltage computed with $\beta = 50$ for $d = 5$ mm over a wide range of pressures. As expected, the breakdown voltage follows Paschen's law for $p \lesssim 10$ bar (1×10^6 Pa) and saturates for higher pressures, in qualitative agreement with the experimental data. It should be stressed that the value $\beta = 50$, used in these computations, is the same as the value of β that gave the qualitative agreement with the experiment for microgaps (the dashed line). We note for completeness that in the range $pd \lesssim 10^{-2}$ bar mm (1×10^3 Pa mm) the breakdown voltage computed for $d = 5$ mm (the solid line) is higher than values given by the experimental Paschen's law (full circles). This can be attributed to the local-field approximation, used in the modelling for evaluation of the transport and kinetic coefficients of electrons, loosing its validity: d is no longer large compared with the electron energy relaxation length and the electron distribution function has to be described by a non-local model [98–101].

The saturation of the breakdown voltage for pressures $p \gtrsim 10$ bar (1×10^6 Pa) may be understood as follows in the framework of this hypothesis. Field emission comes into play for cathodes with a work function of $3-4$ eV at a local field strength at the cathode surface exceeding 10^9 V m^{-1}. For $\beta = 50$, this corresponds to an average field of the order of 2×10^7 V m^{-1} and to a breakdown voltage of the order of $200(d/\text{cm})$ kV. For $d = 5$ mm, this gives the breakdown voltage of the order of 100 kV, comparable with the value of 130 kV at which the solid line in figure 4.1 reaches saturation. It is interesting to note that modelling for the gap $d = 0.5$ mm gave the saturation voltage of 13 kV, which, on the one hand, agrees in order of magnitude with the above simple estimate, and on the other hand means that the computed breakdown voltage starts deviating from the Paschen law at lower pd values than the data for the 5 mm gap shown by the solid line. Similarly, modelling for $p = 10$ bar gave a line which is shifted by an order of magnitude in the direction of higher pd with respect to the dotted line, computed for 1 bar, and approaches the Paschen curve at a larger pd, significantly to the right of the minimum. Thus, both a decrease in the gap width d and an increase in pressure p narrow the range of applicability of the Paschen law.

Another early author [64] made strong arguments explaining the saturation of the breakdown voltage at high pressures not by field emission (or at least not only by field emission), but rather by the enhanced ionization of neutral gas molecules in regions of increased electric field near the protrusions on the surface of the positive or negative electrodes. Recent workers [34, 97] supported this hypothesis by evaluation of the ionization integral.

Thus, the deviations of measured breakdown voltage of parallel-plate gaps from Paschen's curve, observed in microgaps and at very high pressures, may be described in the same way as deviations of field electron emission from cold cathodes in vacuum from the Fowler-Nordheim formula, i.e., in terms of enhancement of electron emission that may occur due a variety of reasons, such as amplification of the applied electric field by microprotrusions present on the cathode surface, local reduction of the work function of the cathode material, 'nonmetallic' electron emission mechanism, plasmons. There is an alternative explanation for deviations from Paschen's curve at very high pressures, and this explanation is specifically related to the supposed existence of microprotrusions on the electrode surfaces: enhanced ionization of neutral gas in regions near protrusions.

The situation may be clarified by considering deviations from the similarity law observed at very high pressures in corona inception and breakdown voltages for discharges on positive cylindrical electrodes of small radii [9, 64]: cathodic phenomena are irrelevant and enhanced ionization of neutral gas in regions near protrusions on the anode surface appears to be the only possible explanation. In this chapter, the measurements [9, 64] are analyzed from this point of view by means of numerical modelling. It is shown that the deviations from the similarity law, observed in the experiment, may indeed be attributed to enhanced ionization of air molecules in regions of enhanced electric field near microprotrusions on the anode surface. Given the absence of any other plausible explanation, this conclusion may be considered as an indirect evidence of the existence of microprotrusions on the electrode surface. Moreover, analysis of the experimental data allows estimating dimensions of the microprotrusions in conditions of these experiments.

The outline of this chapter is as follows. Results of computation of the ignition voltage (voltage corresponding to the initiation of a self-sustaining discharge) in high-pressure air under conditions simulating the measurements [9, 64] for positive polarity are reported and discussed in section 4.2. The effect of protrusions and the potential effect of field emission on the ignition voltage in the case of negative polarity is discussed in section 4.3. Conclusions are summarized in section 4.4.

Results reported in this chapter were published in [62].

4.2 Ignition field on positive corona with different types of protrusions

The aim of modelling of this chapter is to study qualitatively the effect of microprotrusions, present on the surface of the inner electrode, over the discharge ignition voltage under conditions of experiments with concentric cylinder electrodes in high to very high pressure air, reported in [9, 64]. While in the previous chapter, on discharge inception between concentric cylinders, the logarithmic formulation of the species conservation equations was used, which is a frequent choice in the modelling of cold gas discharges, the original formulation, where the dependent variables are the species number densities, was used in this chapter. The reason for this is that the original formulation has been found to be much more efficient for the steady-state modelling required for the computation of the discharge ignition voltage, reported in this chapter. Note that it was the use of the original formulation that made possible the above-described change in the boundary condition for the number densities of the negative ions at the cathode and of the positive ions at the anode.

The modelling allowed to compute the voltage corresponding to the initiation of a self-sustaining discharge (the ignition voltage) for each discharge geometry over a wide range of gas pressures. The initial step for each geometry was to find the ignition voltage for one pressure value using the eigenvalue approach developed in [63]. After that, the control parameter was switched from the discharge voltage to the discharge current and the gas pressure was gradually varied until the whole range of pressure values of interest has been covered. The solution computed for each value of gas pressure was used as an initial approximation for the computation with the next value. The discharge current was kept fixed at this stage and it was ensured that the current is sufficiently low not to affect the computed voltage.

If the electrodes were smooth, the concentric cylinder geometry could be simulated using a one-dimensional (1D) model. 3D models are, strictly speaking, required in order to study the effect of protrusions on the surface of the inner cylinder, except for a special case of protrusions having the shape of long ridges parallel to the cylinder axis, where a 2D model is sufficient. However, multidimensional modelling in the general case requires resolving a thin ionization zone along the entire surface of the inner electrode, and this makes 3D models heavy computationally, so their use for a qualitative investigation is unwarranted.

In this chapter, concentric sphere electrodes are considered with a single cylindrical or conical protrusion on the surface of the inner electrode. Due to the axial symmetry, the modelling is 2D and therefore not too heavy. Since different protrusions come into play under different conditions, the presence of several microprotrusions acting in close proximity is unlikely. (This may be untrue for arrays of identical protrusions, as explained in the beginning of section 4.4 below.) On the other hand, microprotrusions that are not located close to each other do not interact. Since the electric field distributions in the vicinity of small protrusions of the same geometry on cylindrical and spherical electrodes are close to each other, the assumed computational geometry should allow studying the influence of protrusions at least qualitatively.

Results reported in this chapter refer to conical protrusions with a 60° full aperture angle and a spherical tip with a radius of $2\,\mu$m and cylindrical protrusions of a radius of $2\,\mu$m and a (half-)spherical tip of the same radius, both of which are schematically shown in figure 4.2. The protrusion height is several tens of micrometers in both cases. It should be stressed that while the cylindrical protrusion is slender and in line with protrusions usually considered in the modelling of vacuum breakdown (e.g., [102]), the

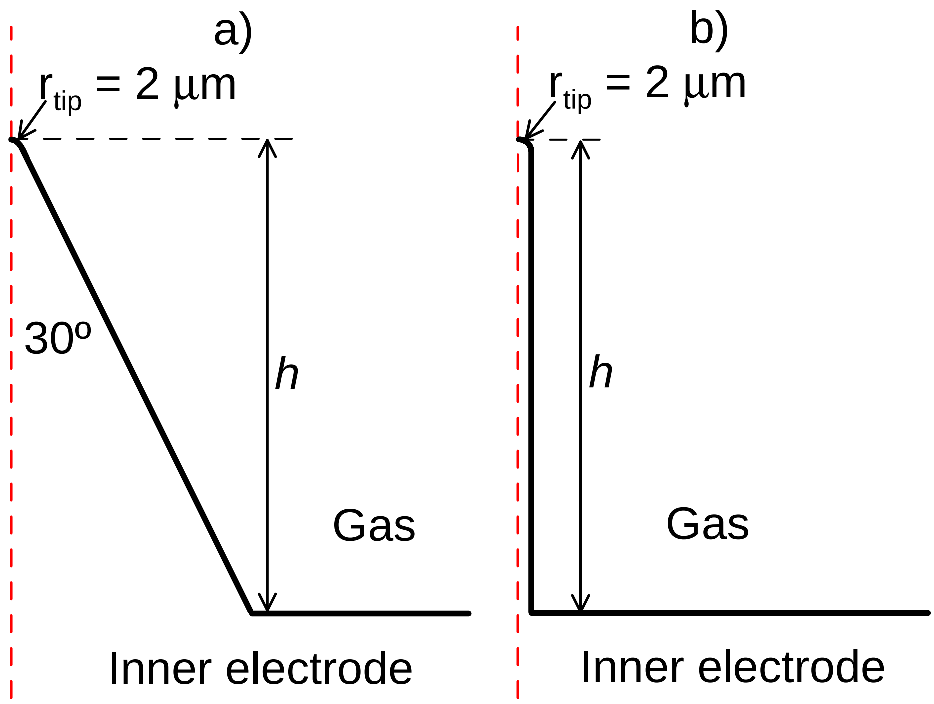

a) b)

Figure 4.2: Schematic representation of the conical (a) and cylindrical (b) protrusions.

conical protrusion, proposed in [103], is not slender and the electric field amplification is due to high values of the ratio of the height of the protrusion to the tip radius.

Let us designate by r_0 and R the radii of the inner and outer electrodes, respectively. The results reported in this chapter simulate experiments with the following values of these parameters: $r_0 = 1.2\,\mathrm{mm}$, $R = 48.75\,\mathrm{mm}$ and $r_0 = 3.18\,\mathrm{mm}$, $R = 48.75\,\mathrm{mm}$, which are geometries studied experimentally in [9], and $r_0 = 6.35\,\mathrm{mm}$, $R = 13.5\,\mathrm{mm}$, which is a geometry studied experimentally in [64]. In the modelling, the radius of the inner sphere was chosen equal to the radius of the inner cylinder in the experiment being simulated. The radius of the outer sphere was chosen equal to the radius of the outer cylinder in the modelling of the experiment [64]. In the modelling of the experiment [9], the radius of the outer sphere was chosen such that the width of the discharge gap be equal to $10\,\mathrm{mm}$, instead of about $46 - 48\,\mathrm{mm}$ as in the experiment. This reduction of the computation domain allowed reducing the number of elements of the numerical mesh. On the other hand, this reduction did not introduce a significant error, since the effect of the radius of the outer electrode on the ignition field is weak, which is well known (e.g., R does not appear in Peek's formula for the ignition field

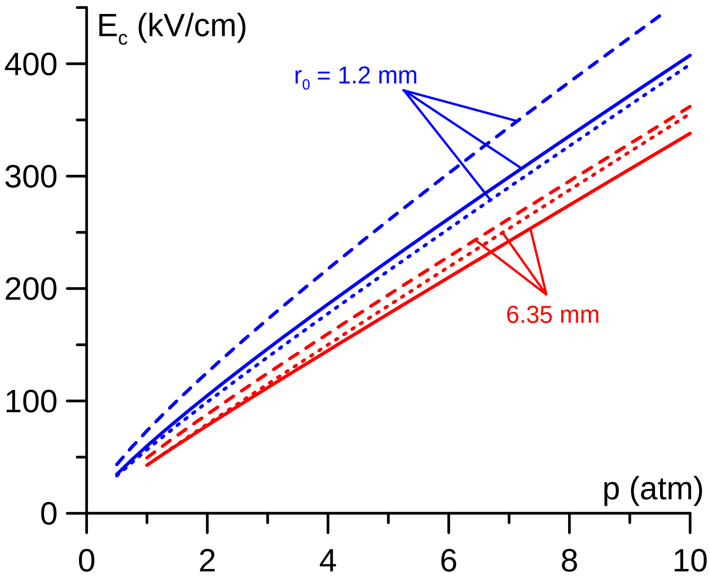

Figure 4.3: Ignition field on a positive electrode without protrusions for two values of the electrode radius r_0. Solid: modelling, concentric cylinder electrodes. Dotted: empirical Peek's formula for the ignition field of a positive corona discharge between concentric cylinder electrodes. Dashed: modelling, concentric sphere electrodes.

of a positive corona discharge between concentric cylinder electrodes) and was verified in the modelling of this chapter.

The comparison parameter is E_c the macroscopic ignition electric field at the inner electrode, defined as $E_c = U_c / [r_0 \ln (R/r_0)]$ for concentric cylinders and $E_c = U_c / [r_0 (1 - r_0/R)]$ for concentric spheres, where U_c is the ignition voltage.

Let us start with verifications for the case without protrusions. The solid lines in figure 4.3 represent the ignition field on a positive electrode between concentric cylinder electrodes, computed by means of the model used in this thesis without account of protrusions, for two of the above-mentioned geometries: $r_0 = 1.2\,\text{mm}$, $R = 48.75\,\text{mm}$ and $r_0 = 6.35\,\text{mm}$, $R = 13.5\,\text{mm}$. The dotted lines depict the corona ignition field at the surface of a positive inner cylinder (wire) given by equation (1) of [9], which is one of variants of empirical Peek's formula. The solid and dotted lines are very close to each other for both geometries; an additional validation of the model.

The dashed lines in figure 4.3 represent the ignition field calculated for concentric sphere electrodes with $r_0 = 1.2\,\text{mm}$, $R = 11.2\,\text{mm}$ and $r_0 = 6.35\,\text{mm}$, $R = 13.5\,\text{mm}$. The difference between the ignition fields computed for the concentric sphere and cylinder electrodes is relatively small. As expected, the difference is smaller for the wider electrode, $r_0 = 6.35\,\text{mm}$; cf., e.g., figure 4 of [29].

The effect of protrusions for the case of positive polarity is illustrated by figures 4.4-

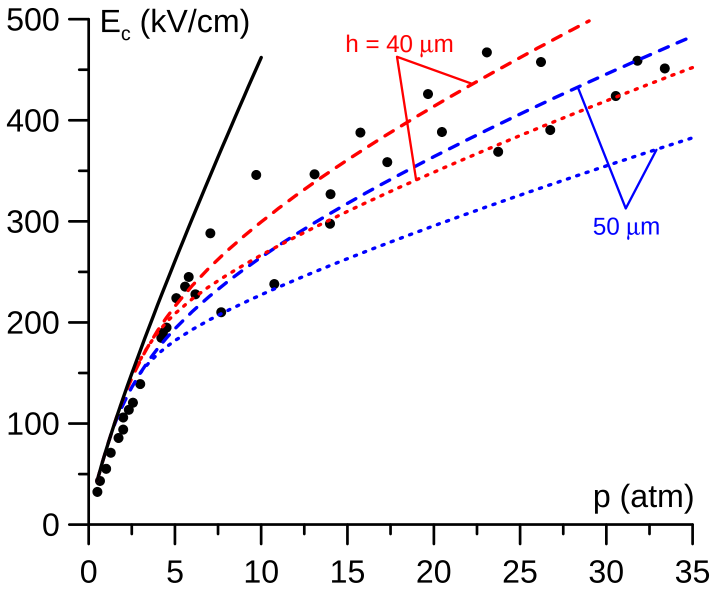

Figure 4.4: Ignition field on a positive electrode, $r_0 = 1.2\,\mathrm{mm}$. Lines: modelling without account of protrusions (solid) and with account of a conical (dashed) or cylindrical (dotted) protrusion of height h. Points: experiment [9].

4.6. The lines in these figures were computed for concentric sphere electrodes without account of protrusions (solid) or with account of a conical or cylindrical protrusion of a height h on the inner electrode (dashed and dotted, respectively). The points in figures 4.4 and 4.5 represent the discharge ignition field estimated from the experimental corona-starting voltage reported in [9], in the pressure range $p \lesssim 5\,\mathrm{atm}$ ($5.07 \times 10^5\,\mathrm{Pa}$), where a preceding corona discharge was observed prior to sparkover, and from the sparkover voltage [9] for higher pressures, where a preceding corona discharge was not observed. The points in figure 4.6 represent the discharge ignition field estimated from the experimental breakdown voltage [64].

Figures 4.4-4.6 refer to the ignition field on positive electrodes of different radii. In all the cases, the computed ignition field is close to the experimental values in the pressure range of $0.5 - 3\,\mathrm{atm}$ ($5.07 \times 10^4 - 3.04 \times 10^5\,\mathrm{Pa}$), where the effect of protrusions is negligible and the similarity law and Peek's formula hold. As expected, the presence of a protrusion results in a reduction of the macroscopic ignition field due a higher local electric field and, consequently, substantially increased ionization in the vicinity of the protrusion. The effect comes into play at pressures of the order of $5\,\mathrm{atm}$ ($5.07 \times 10^5\,\mathrm{Pa}$). As expected, the larger the assumed protrusion height h, the lower the computed ignition field is. A cylindrical protrusion produces a stronger effect than a conical protrusion of the same height, although the difference is not very substantial. A qualitative agreement with the experiment in all the cases is achieved

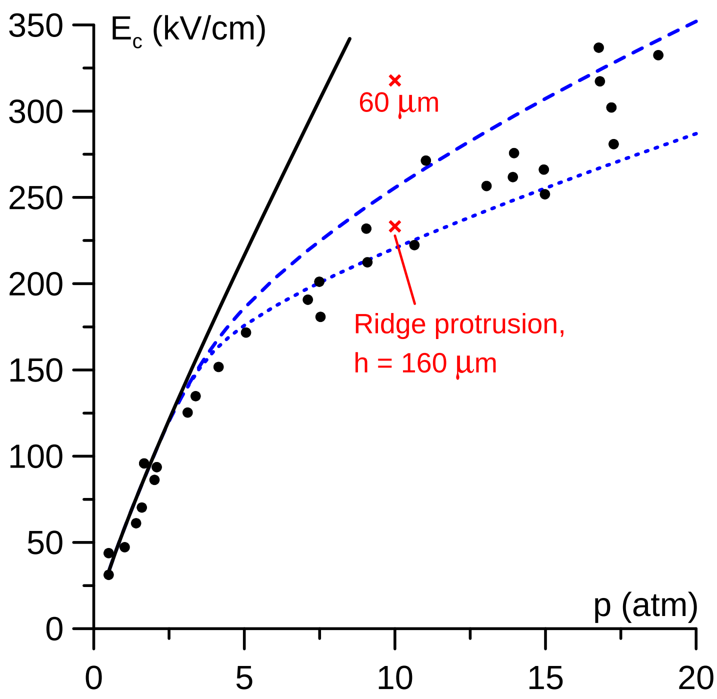

Figure 4.5: Ignition field on a positive electrode, $r_0 = 3.18\,\mathrm{mm}$. Lines: modelling without account of protrusions (solid) and with account of a conical (dashed) or cylindrical (dotted) protrusion of a height of $50\,\mu\mathrm{m}$. Crosses: modelling, concentric cylinder electrodes with a ridge protrusion of height h. Points: experiment [9].

for protrusion heights of the order of $50\,\mu\mathrm{m}$. Such values seem rather high, however there is no other explanation in sight at present.

For comparison purposes, also shown in figure 4.5 are results of simulations for concentric cylinder electrodes with a long ridge at the surface of the inner cylinder, parallel to the cylinder axis. These simulations were 2D as well, but performed in the Cartesian coordinates (x, y), rather than in the cylindrical coordinates (r, z) as the simulations for concentric sphere electrodes with a conical or cylindrical protrusion. The ridge had a $60\,^\circ$ full aperture angle and a cylindrical rounding of a radius of $2\,\mu\mathrm{m}$ at the tip, i.e., the transversal (perpendicular to the cylinder axis) cross section of the ridge was the same as the axial cross section of the conical protrusion. The crosses in figure 4.5 refer to two values of the ridge height, $60\,\mu\mathrm{m}$ and $160\,\mu\mathrm{m}$. One can see that ridge protrusions must have a bigger height than conical ones for a comparable effect.

The experimental data [64] shown in figure 4.6 manifest saturation of the breakdown field in the range $p \gtrsim 30\,\mathrm{atm}$ ($3.04 \times 10^6\,\mathrm{Pa}$), whereas the modelling does not. However, one should note that the author [64] mentioned that the measurements were uncertain at higher pressures and a reproducible breakdown voltage measurement was hard to perform.

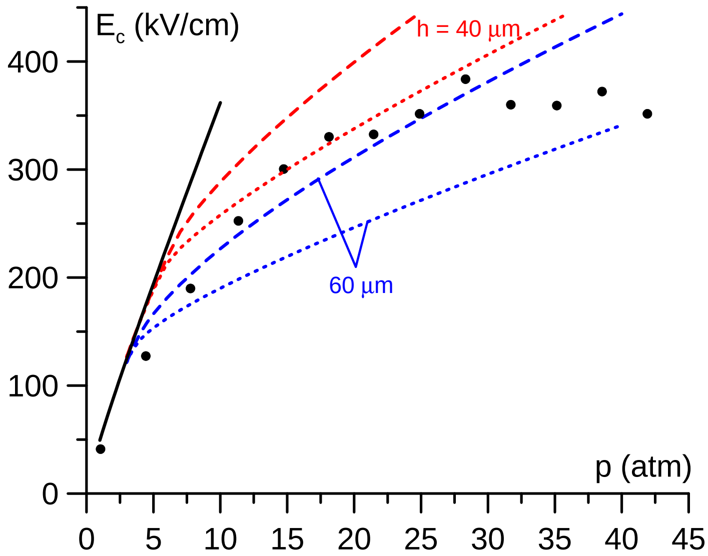

Figure 4.6: Ignition field on a positive electrode, $r_0 = 6.35\,\mathrm{mm}$. Lines: modelling without account of protrusions (solid) and with account of a conical (dashed) or cylindrical (dotted) protrusion of height h. Points: experiment [64].

The effect of protrusions over the computed distribution of discharge parameters along the electrode surface is illustrated by figure 4.7. The simulation conditions are the same as those of figure 4.5 with a conical protrusion of a height of $50\,\mu$m. For the atmospheric pressure (figure 4.7a), the discharge is distributed along the electrode surface in a more or less uniform way; in other words, the effect of the protrusion is minor. The discharge ignition field is adequately described by Peek's formula. As pressure increases, the discharge starts concentrating in the vicinity of the protrusion (figure 4.7b) and the ignition field is lower than the value given by Peek's formula.

Although high values of the ratio of the protrusion height to the tip radius are required for electric field amplification and hence represent a necessary condition for the deviations from the similarity law at high pressures observed in [9, 64], this condition alone is not sufficient: the protrusion height must be not too small, otherwise the electric field decays at very small distances from the protrusion tip and sufficient ionization is not produced. An example is shown in figure 4.8. Here z is the distance measured along the discharge axis from the protrusion tip, E/N is the reduced electric field, shown by solid lines, and $K = \int_0^z \alpha_{\mathrm{eff}}\, dz$ is the ionization integral (α_{eff} is evaluated using the data in Appendix A), shown by dashed lines. Data for two conical protrusions of different heights h with the same aspect ratio h/r_{tip} are shown. For the protrusion with $h = 50\,\mu$m, the computed ignition field, $E_c \approx 364\,\mathrm{kV\,cm^{-1}}$, is shown in figure 4.4 and agrees with the experiment as seen in the latter figure. The total (evaluated along the ionization zone) ionization integral is contributed by the region

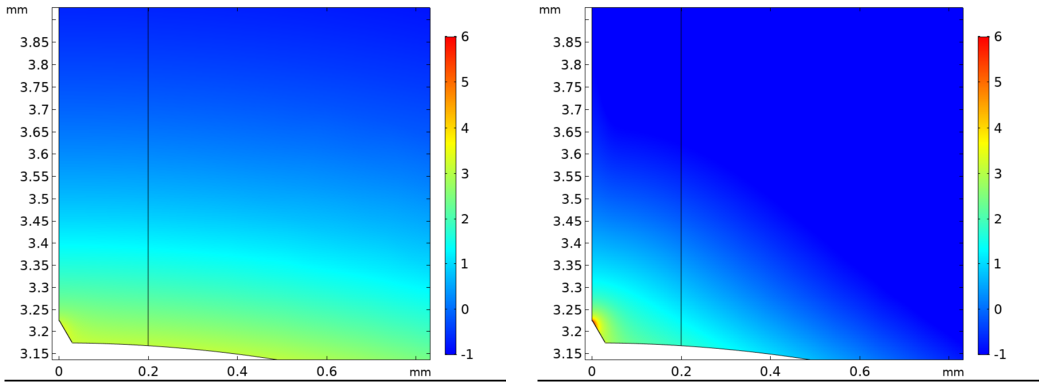

a) b)

Figure 4.7: Bidimensional distribution of the logarithmic density of the negative ions O_2^- in the vicinity of a conical protrusion of a height of $50\,\mu$m at the surface of a positive electrode. Density in m^{-3}. Discharge current 10^{-14} A, $r_0 = 3.18$ mm. (a): $p = 1$ atm. (b): $p = 5$ atm.

of z of the order of r_{tip} ($= 2\,\mu$m). For the protrusion with $h = 5\,\mu$m, the electric field is higher at the protrusion tip but decays in space faster, therefore the contribution of the region of z of the order of r_{tip} ($= 0.2\,\mu$m) to the total ionization integral is no longer dominating. Unsurprisingly, the computed ignition field, $E_c \approx 836\,\mathrm{kV\,cm^{-1}}$, is much higher than the experimental value shown in figure 4.4.

It is seen from figure 4.8 that the total ionization integral characterizing the ignition of corona-like discharges strongly depends on the geometry. This is an interesting illustration of the limitation of the method for evaluation of ignition potential by assuming a prescribed value for the ionization integral, which is routinely used as a substitute for numerical modelling similar to the one used in this thesis.

4.3 Ignition field on negative polarity and the effect of field emission

For completeness, let us consider the effect of protrusions in the case of negative polarity (the inner cylinder being the cathode). The experimental data from [64] for the negative polarity under conditions comparable to those of figure 4.6 are shown in figure 4.9. As in the previous section, the lines were computed for concentric sphere electrodes without account of protrusions (solid) or with account of a conical protrusion of a height of $60\,\mu$m on the inner electrode (dashed, dotted, and dash-dotted lines), for various values of the secondary electron emission coefficient γ. The points represent

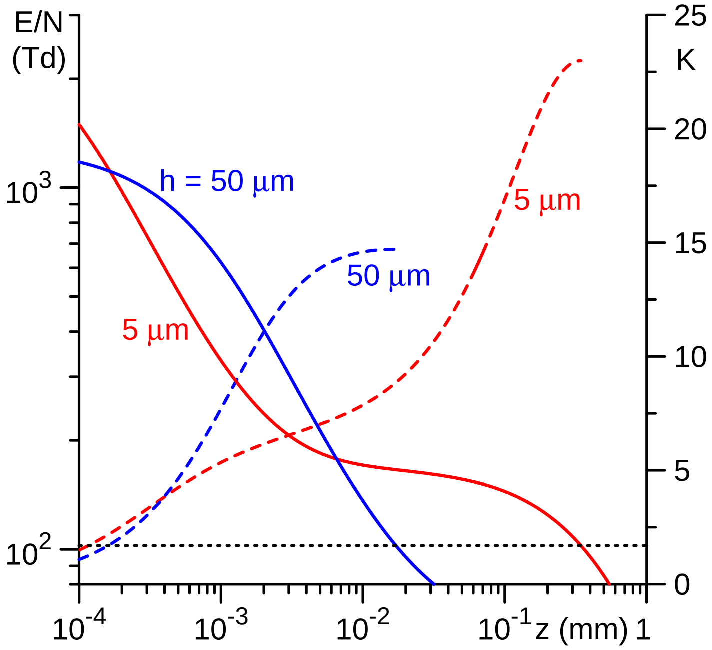

Figure 4.8: Distributions of the reduced electric field (solid) and the ionization integral (dashed) along the discharge axis. Dotted: critical field. Positive inner electrode, $r_0 = 1.2\,\text{mm}$, $p = 20\,\text{atm}$, conical protrusions with $h = 50\,\mu\text{m}$, $r_{tip} = 2\,\mu\text{m}$ and $h = 5\,\mu\text{m}$, $r_{tip} = 0.2\,\mu\text{m}$.

the discharge ignition field estimated from the experimental breakdown voltage [64].

One can see that the deviations from the similarity law for the negative polarity are qualitatively similar to those for the positive polarity, however at high pressures the breakdown voltage for the negative polarity is, somewhat surprisingly, higher than for the positive polarity. Note that a similar effect has been observed in conditioning experiments described in [104]: at application of DC high voltage to a plane-plane gap with a 4 mm diameter sphere at one of the electrodes in air at pressure of 30 bar (3×10^6 Pa), the first breakdown voltages for a positive potential at the sphere were considerably lower than the corresponding values for the negative polarity.

In the case of negative polarity, primary electrons are supplied to the ionization zone at the inner electrode by the electron emission from the electrode surface, rather than by photoionization as in the case of positive polarity. Two electron emission mechanisms need to be considered: secondary electron emission and field emission. The modelling shown in figure 4.9 was performed for various values of the effective coefficient of secondary electron emission without account of the field emission. The ignition field on the negative electrode varies with γ as one could expect, and the presence of the protrusion significantly enhances this variation. The latter can be understood as follows. In the case without protrusions, the electric field at the cathode

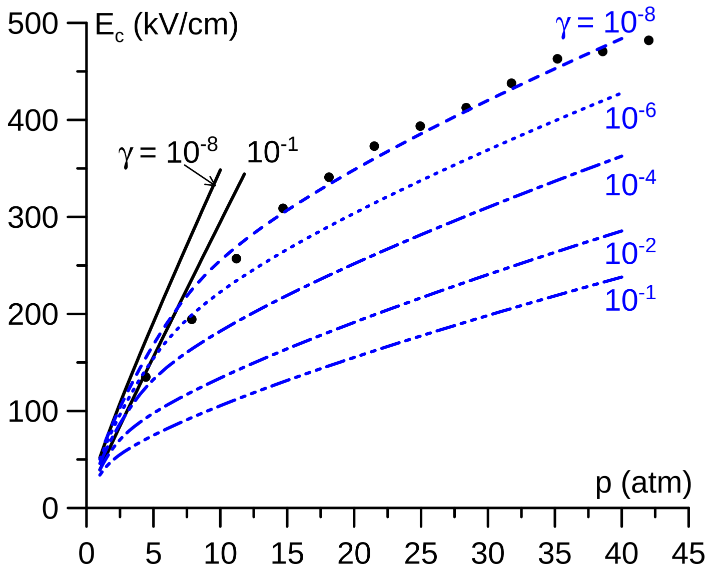

Figure 4.9: Ignition field on a negative electrode, $r_0 = 6.35\,\mathrm{mm}$. Lines: modelling without account of protrusions (solid) and with account of a conical protrusion of a height of $60\,\mu\mathrm{m}$ (dashed, dotted, and dash-dotted lines), for various values of the secondary electron emission coefficient γ. Points: experiment [64].

surface is close to the critical field, i.e., the field value at which the electron impact ionization is just sufficient to balance the electron attachment. The electron impact ionization rate coefficient grows very rapidly with the increasing electric field in this field range, and minor discharge voltage variations are sufficient to compensate significant variations in the number of primary electrons, caused by variations in γ. In the case with the protrusion, the electric field at the protrusion is appreciably higher than the critical field; the field dependence of the electron impact ionization rate coefficient in this field range is less strong, hence variations in the discharge voltage, caused by variations in γ, are more significant.

The maximum average electric field at the surface of the negative electrode under conditions of the experiment [64] is $5 \times 10^7\,\mathrm{V\,m^{-1}}$; cf. figure 4.9. The electric field at the tip of a protrusion of a height of $50\,\mu\mathrm{m}$, given by the axially symmetric electrostatic simulations, is higher by the factor of approximately 20 or 27 for the conical or cylindrical protrusions, respectively, and thus is close to $10^9\,\mathrm{V\,m^{-1}}$. The latter value is too low for the field emission to be appreciable. Indeed, the field emission current evaluated from the axially symmetric numerical modelling for conditions of figure 4.9 for $p = 40\,\mathrm{atm}$ ($4.05 \times 10^6\,\mathrm{Pa}$) is by six orders of magnitude lower than the secondary electron emission current even for the lowest γ value considered $\gamma = 10^{-8}$. Thus, the enhancement factor is not high enough or, equivalently, the aspect ratio is not sufficient for appreciable field emission. One can conclude that in these conditions the effect of the enhanced ionization of air molecules in regions of amplified electric field near microprotrusions at the cathode surface comes into play for lower values of the aspect ratio than the field emission.

As mentioned above, deviations from the similarity law for the negative and positive polarities, observed in the experiment [64], are qualitatively similar. Comparing computation results shown in figures 4.9 and 4.6, one can conclude that the effect produced by the account of the microprotrusion in the modelling for the cases of negative and positive polarities is qualitatively similar as well, in agreement with the experimental data. The fact that the experimental breakdown voltage for the negative polarity at high pressures is higher than for the positive polarity, means in terms of the modelling that the effective secondary electron emission coefficient at the surface of the negative electrode is smaller than 10^{-6}, which is a typical value characterizing photoionization in this pressure range. Indeed, the value of γ, which ensures the best agreement with the experiment in figure 4.9, is $\gamma = 10^{-8}$. On the other hand, this value is unusually low. This point clearly requires further experimental investigation. One could imagine, as a possible reason, a decrease of γ with increasing pressure, for example, due to the deposition of neutral gas molecules on the metal surface, or since cluster ions with a large number of water molecules, formed at high pressures, do not produce secondary electrons as efficiently as light ions.

4.4 Summary and concluding remarks

The voltage corresponding to the initiation of a self-sustaining discharge was computed in corona-like discharge configurations with microprotrusions on the surface of the inner electrode over a wide range of pressures by means of 2D numerical modelling. In particular, the model describes, in a natural way, the enhanced ionization of air molecules in regions of amplified electric field near the microprotrusion. The aim of the modelling is to find out if the latter mechanism may be responsible for the deviations from the similarity law at high pressures, observed in the experiment.

The model was applied to conditions of corona inception and breakdown experiments on concentric cylinders over a wide pressure range described in [9, 64]. An axially symmetric geometry consisting of concentric sphere electrodes with a single cylindrical or conical microprotrusion on the surface of the inner electrode was considered. Since different protrusions come into play under different conditions, the presence of several microprotrusions acting in close proximity is unlikely. (Note that this reasoning does not apply to arrays of identical protrusions, nevertheless it is interesting to mention in this connection the recent experiments [105], which showed little effect of the number of protrusions in the array for the case of SF_6 but a more appreciable effect for the case CO_2; figures 7-8 and 12-13 of [105], respectively. This is an interesting point that may need to be revisited in the future.) On the other hand, microprotrusions that are not located close to each other do not interact. Therefore, the assumed computational geometry with a single protrusion should be sufficient for a qualitative study while avoiding 3D modelling, which is demanding and unwarranted at this stage. The reported results refer to conical protrusions with a 60° full aperture angle and a spherical tip with a radius of $2\,\mu$m and cylindrical protrusions of a radius of $2\,\mu$m with a half-spherical tip, the protrusion heights being of several tens of micrometers in both cases. While the cylindrical protrusion is slender, the conical protrusion is not and the electric field amplification is due to high values of the ratio of the height of the protrusion to the tip radius.

For lower pressures, in the range of $0.5 - 3$ atm ($5.07 \times 10^4 - 3.04 \times 10^5$ Pa), the discharge is not appreciably affected by the presence of the protrusion and is distributed along the surface of the inner electrode in a more or less uniform way. The computed ignition field is close to the experiment and to values given by empirical Peek's formula and increases with p approximately proportionally, in agreement with the similarity law. For higher pressures, the discharge concentrates in the vicinity of the protrusion and the increase of the computed ignition field with pressure slows down, in agreement with the experimental data. The protrusion heights necessary to achieve a qualitative agreement with the experiment are of the order of $50\,\mu$m in all the cases.

In the case where the inner electrode is positive, the enhanced ionization of air molecules in regions near microprotrusions on the electrode surface appears to be the only possible explanation for the deviations from the similarity law at high pressures, observed in the experiments [9, 64]. The qualitative agreement of the simulation results with the experiment can be considered as indirect evidence of the existence of microprotrusions and indicates what height of microprotrusion is necessary to produce the effect: on the order of tens of micrometers. The protrusions need not necessarily be slender; e.g., conical protrusions with a large (60°) aperture angle and a small tip curvature radius produce a similar effect. Ridge protrusions produce a similar effect as well, however a bigger height or a smaller tip curvature radius is required. This aspect is important since protrusions that are not slender appear to be more realistic than needle-like ones.

It should be stressed that, although high values of the ratio of the protrusion height to the tip radius are required for electric field amplification and hence represent a necessary condition for the deviations from the similarity law at high pressures observed in [9, 64], this condition alone is not sufficient: the protrusion height must be not too small, otherwise the electric field decays at very small distances from the protrusion tip and sufficient ionization is not produced. Thus, while the above-mentioned values of microprotrusion height of several tens of micrometers may appear rather high, there seems to be no other explanation at present.

The enhanced ionization of air molecules in regions near protrusions on the electrode surface explains also the deviations from the similarity law at high pressures observed in the experiments [64] in the case where the inner electrode is negative. Another mechanism that may play a role in this case is the enhanced electron emission from the cathode surface; the same mechanism which causes deviations from the Fowler-Nordheim formula in experiments on field electron emission from cold cathodes in vacuum and which may occur due a variety of reasons, such as amplification of the applied electric field by microprotrusions on the cathode surface, local reduction of the work function of the cathode material, 'nonmetallic' electron emission mechanism, plasmons. In this work, the enhancement of the field emission due to the amplification of the electric field was estimated and it was found that in the range of values of the protrusion aspect ratio where the enhanced ionization of air molecules in the gas phase comes into play the field emission is still insignificant.

Modelling results in this chapter show that the experiments on positive corona discharge ignition and breakdown at high and very high pressures can serve as a useful, albeit inevitably indirect, source of information about microprotrusions on the surface of electrodes. Unfortunately, the experimental information available is clearly insufficient. One of important questions to be answered is the relation between the deviations from the similarity law and the degree of polishing of the inner electrode. Note that experimental results reported in [9] refer to four values of the inner cylinder radius: 0.089 mm, 0.216 mm, 1.20 mm, and 3.18 mm. Deviations from the similarity law, found in the modelling with the same protrusion height of 50 μm, were comparable for all the four values. The deviations found in the experiment [9] were comparable for the radii of 1.20 mm and 3.18 mm (cf. figures 4.4 and 4.5 above), were significantly smaller for 0.216 mm, and still smaller for 0.089 mm. Of course, microprotrusions on different cylinders need not be the same; in particular, it is unclear if 50 μm protrusions are likely to occur on a wire of a radius of 89 μm. Hopefully, the relation between the deviations from the similarity law and the degree of polishing of the inner electrode will be addressed in future experiments.

Chapter 5

Study of time-averaged characteristics of positive and negative DC corona discharges in atmospheric air

5.1 Introduction

In this chapter, the model of plasmachemical processes in low-current discharges in high-pressure air is used for investigation of time-averaged characteristics of DC corona discharges in ambient air. As mentioned earlier, the approach involves the use of stationary solvers instead of time-dependent ones. The latter kind of solvers are standard tools in the modelling of corona discharges, as well as in gas discharge modelling in general. Time-dependent computations give detailed information on spatiotemporal distributions of plasma parameters and are indispensable for studies of pulsed coronas; for example, computational studies of pulsed regimes of DC corona discharges in point-plane air gaps in the framework of non-stationary approaches are reported in recent works [55, 56, 106, 107]. Time-dependent solvers can be used also for the computation of time-averaged characteristics of DC corona discharges in the framework of stationary corona discharge models; e.g., [57, 108]. However, such solvers are highly, and in many cases, prohibitively, computationally intense. Therefore, stationary characteristics of DC corona discharges are calculated in most cases by means of various approximate methods; e.g., [36, 57, 75, 109–112].

An alternative to using time-dependent solvers for stationary corona discharge models is to employ stationary solvers, which solve steady-state equations describing the stationary discharge by means of an iterative process unrelated to time relaxation. Stationary solvers offer important advantages in simulations of steady-state discharges. In particular, they are not subject to the Courant–Friedrichs–Lewy criterion or analogous limitations on the mesh element size, which allows one to dramatically speed up simulations.

In chapters 3 and 4, stationary solvers were used for the computation of inception of corona discharges. In this chapter, the same method is used to calculation of time-averaged characteristics of DC positive and negative corona discharges in a wide current range. Somewhat surprisingly, it seems that experimental data on corona discharges reported in the literature beyond the simplest one-dimensional wire-cylinder configuration are insufficient for an accurate quantitative comparison, since not all relevant geometrical parameters are indicated. Therefore, special experiments have been performed on point-to-plane coronas in a wide current range of currents of both polarities.

The outline of this chapter is as follows. The computed current-voltage characteristics of DC corona discharges in ambient air, in both 1D concentric cylinders and point-to-plane gaps for both polarities, are reported and discussed in section 5.2. For point-to-plane gaps, various values of the discharge gap have been used and spatial distributions of the radiation intensity are compared with experimental results. This section also presents an investigation of the validity of the classic Townsend-Kaptzov assumption in negative corona discharges in an axially symmetric wire-cylinder gap. Conclusions are summarized in section 5.3.

Results reported in this chapter were published in [5, 61, 63].

5.2 Current-voltage characteristics in different geometries

5.2.1 Model validation in 1D concentric cylinders

A wide range of discharge currents needs to be computed in the framework of the model presented in the previous chapters. Let us start with verifications of the model for the simplest case of 1D concentric cylinders. The CVCs of positive and negative corona discharges in atmospheric-pressure air, computed by means of the model described in the previous chapters, are shown in figure 5.1. Also shown are time-averaged CVCs obtained experimentally in [42]. The agreement between the modelling and the experiment is quite good. Although not shown, qualitatively good agreement was also achieved with other experimental data, e.g. with the work [44].

The CVCs shown in figure 5.1 have been computed by means of stationary solvers in the framework of the approach described in section 2. Alternatively, the CVC of the

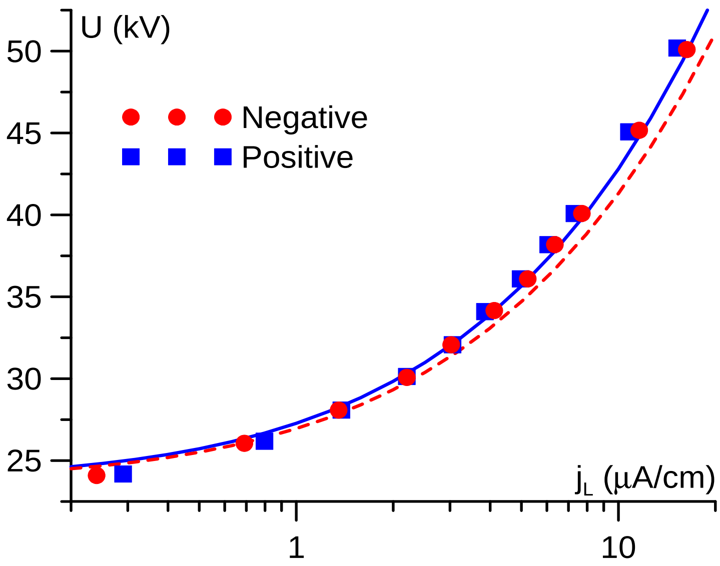

Figure 5.1: Current-voltage characteristic of positive and negative coaxial corona discharges in concentric-cylinder geometry. Air, 1 atm, inner electrode radius 0.070 cm, outer electrode radius 10.35 cm. Lines: modelling. Points: experiment [42]. Solid line, squares: positive corona. Dashed line, circles: negative corona. j_L: linear current density.

positive corona could also be computed by means of time-dependent solvers, which are the usual tool in gas discharge modelling. However, the switching from a stationary solver to a time-dependent one causes a very significant increase of the computation time, which can be by several orders of magnitude, specifically in 2D modelling as will be shown further in the conclusions of this chapter.

5.2.2 The Townsend-Kaptzov assumption in negative wire-cylinder gap

As mentioned previously, the classic Townsend-Kaptzov assumption states that the steady state electric field at the conductor surface remains at the corona onset value. Note that this assumption can be traced back to the foundational work of Townsend of 1914 [37] and is a cornerstone of the corona discharge theory. Recently, the authors [44] reported results of measurement of electric field inside negative corona discharges in an axially symmetric wire-cylinder gap, performed using the modern electric field induced second harmonic generation (E-FISHG) method. Based on these results, it was concluded that the electric field at the wire surface is proportional to the current density of the corona discharge with a negative constant of proportionality or, in other words, appreciably decreases with increasing current, contrary to the classic

Kaptzov assumption. The experimental results [44] are of importance since constitute a significant advance and may be used, in particular, for validation of various corona discharge models. Moreover, the distribution of the electric field in the drift region, given by numerical modelling in the framework of a steady-state one-dimensional (1D) model shown in section 2, is in a good agreement with experimental values given in [44], which shows that this model provides a reasonably accurate averaged description of a negative wire-cylinder corona and, in particular, justifies the use of this model for the interpretation of experiment as done in [44]. However, it is shown here that the conclusion that the electric field at the wire surface decreases with increasing current stems from a misinterpretation and there are no reasons to doubt the validity of the Townsend-Kaptzov assumption.

Values of the electric field reported in [44] have been measured in the range of axial distances r from 0.25 cm to 2.5 cm, while the wire radius was $r_0 = 0.1$ cm. In order to estimate the electric field value at the surface of the wire, the measurements were extrapolated with the use of the well-known approximate equation (e.g., [1, 37, 43]) describing the distribution of the electric field in coaxial wire-cylinder corona discharge gaps:

$$E^2(r) = \frac{I_l}{2\pi\varepsilon_0\mu}\left(1 - \frac{r_0^2}{r^2}\right) + \left(\frac{E_0 r_0}{r}\right)^2. \tag{5.1}$$

Here I_l is the corona current per the unit length, μ is the mobility of the ions that are believed to dominate current transfer in the drift region (mobility of the negative ions was assumed in [44]), and $E_0 = E(r_0)$ is the electric field at the wire surface. Based on this extrapolation, the authors in [44] estimated E_0. For example, the value of E_0 obtained for $I = 0.45\,\mathrm{mA}$, which was the highest discharge current reported in [44], was approximately 44 $\mathrm{kV\,cm^{-1}}$. The distribution of the electric field in the discharge gap calculated by means of Eq. (5.1) with the use of this value and μ equal to 2.2 $\mathrm{cm^2\,V^{-1}\,s^{-1}}$ is depicted by the dashed line in figure 5.2.

There is a problem with these data that can be explained as follows. The value of E_0 at inception, given in [44], is approximately 63 $\mathrm{kV\,cm^{-1}}$ and the corresponding value of the ionization integral K (that is, the integral of the effective ionization coefficient over the ionization region), evaluated in terms of the Laplacian distribution of the electric field, is 9.58. For $I = 0.45\,\mathrm{mA}$, the value of K, evaluated with the use of Eq. (5.1) with the above-mentioned value $E_0 = 44$ $\mathrm{kV\,cm^{-1}}$, is 1.85, i.e., much lower, and hence, the condition of reproducibility of charges in the ionization region is grossly violated; such discharge would not be self-sustained.

One should suspect that Eq. (5.1) cannot be used for extrapolation in these conditions. Another indication in the same direction is suggested by figure 5.2: the slope of the electric field distribution, given by Eq. (5.1), is different from that revealed by

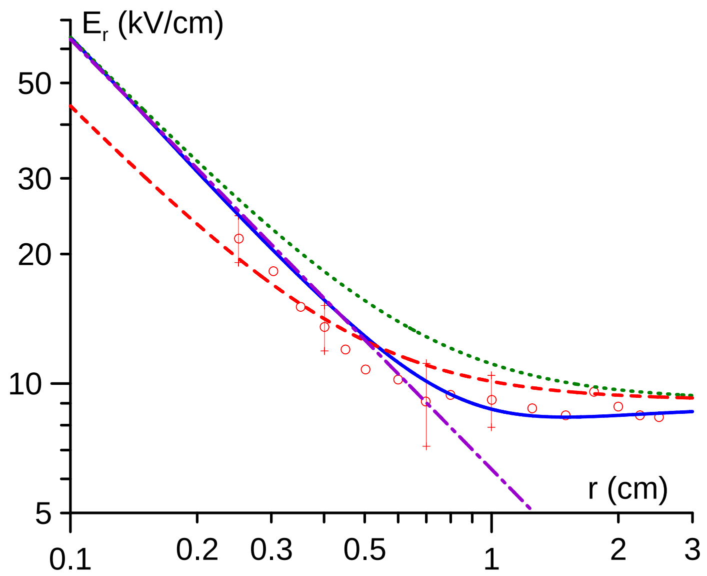

Figure 5.2: Electric field distributions in the gap evaluated under various approximations, $I = 0.45\,\text{mA}$. Points: experiment [44]. Solid: modelling. Dashed: Eq. (5.1), E_0 from [44]. Dotted: Eq. (5.1), E_0 from modelling. Dash-dotted: Laplacian field.

the experimental data.

Equation (5.1) is an approximate relation obtained from the ion transport equation coupled with the Poisson equation, and in order to analyze its validity, one should resort to a more accurate theoretical model, comprising these and other relevant equations. A number of such models are described in the literature. Here, the model described in section 2 was used. The results below refer to $r_0 = 0.1\,\text{cm}$, the inner radius of the cylinder equal to 3 cm, and the secondary electron emission coefficient equal to 10^{-5}. The computed distribution of the electric field in the gap is in good agreement with the experimental data in [44], as exemplified by the solid line in figure 5.2, and the computed values of the inception field and discharge voltages for different currents conform to the experimental values, given in [44], to the accuracy within approximately 3%. This attests to the suitability of the used model for the discharge conditions considered.

The computed contributions to the current transport of the electrons, positive ions, and negative ions are shown in figure 5.3 for $I = 0.45\,\text{mA}$. It is seen that the main contribution in the range $r = 0.2 - 0.6\,\text{cm}$ is made by the electrons, with their mobility being by several orders of magnitude higher than that of the ions. It follows that Eq. (5.1) with the negative ion mobility does not describe correctly the electric field distribution in the region $r \geq 0.2\,\text{cm}$. The latter is indeed the case, as shown by figure 5.2: the distribution of the electric field given by Eq. (5.1) and depicted by the

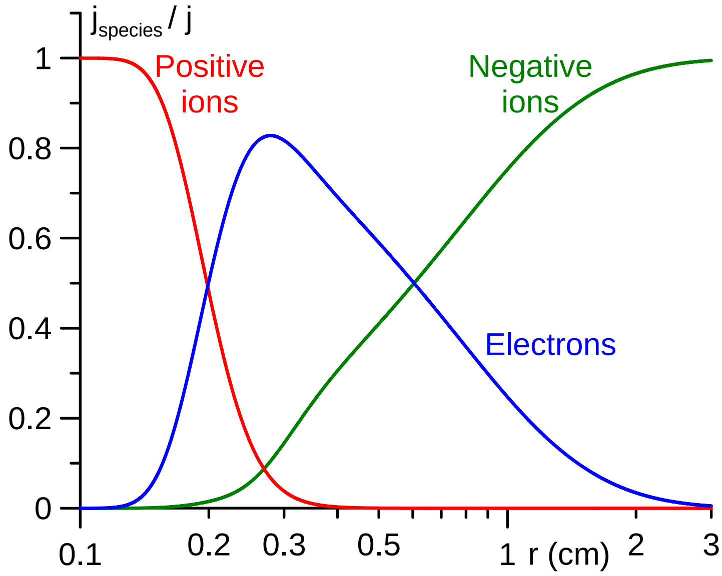

Figure 5.3: Contributions of various charged species to the current transport, $I = 0.45\,\mathrm{mA}$.

dotted line deviates for $r \geq 0.2\,\mathrm{cm}$ from the solid line, which represents the modelling results. It is unsurprising that, therefore, no choice of E_0 allows bringing Eq. (5.1) into agreement with experimental data obtained over a wide range of r values, as exemplified by the dashed line in figure 5.2.

This explains why Eq. (5.1) cannot be used for the extrapolation of the experimental data to the wire surface. In fact, such extrapolation gives values of the surface electric field that are significantly lower than those given by the modelling, as exemplified in figure 5.2. Note that the field at the wire surface, given by the modelling, varies by not more than approximately 1% over the whole current range considered. In other words, the electric field at the wire remains at the corona inception level, in agreement with the Townsend-Kaptzov assumption. This is consistent with the fact that the computed electric field in the ionization region is very close to the Laplacian field at the inception (dotted-dashed line in figure 5.2), i.e., is not perturbed by the space charge.

It is well known that the negative DC corona in air frequently operates in a pulsed regime: the current waveform reveals the so-called Trichel pulses. Moreover, negative wire coronas are in many cases three-dimensional: bright spots appear on the wire surface. These spots, which are sometimes called 'tufts', represent a self-organization phenomenon and do not necessarily appear on the whole wire; e.g., Fig. 10 in [113] and its discussion. Neither the images of the negative corona wire nor the waveforms of the corona current are given in [44], and it is possible that the Trichel pulses and tufts were present in these experiments. If the latter is the case, the agreement between the modelling and experimental data seen in figure 5.2 shows that a steady-state 1D model provides a reasonably accurate averaged description of current transfer in the drift region of a pulsed negative wire-cylinder corona, sufficiently far away from the highly transient near-cathode layer. In particular, this justifies the use of the steady-state 1D model for the interpretation of measurements performed in the drift region, as done in [44].

It is useful to emphasize that while the dependence of the wire surface field on the DC corona discharge current in axially symmetric wire-cylinder gaps is weak, in other corona configurations, e.g. in point-plane gaps, the field at the stressed electrode can vary substantially with the current due to a redistribution of the current density over the electrode surface with increase in the applied voltage. This topic requires special consideration.

It has been shown that the agreement between modelling results and experiments of [42] and [44], for the case of 1D concentric cylinders, is quite good (shown in figures 5.1 and 5.2 respectively). The model will now be applied in studying the time-averaged characteristics of DC corona discharges in point-to-plane gaps in ambient air. A wide range of currents of both voltage polarities with various gap widths, where all relevant geometrical parameters of the point electrode are known, is investigated.

Two formulations of the species conservation equations have been tested: the original formulation, where the dependent variables are the species number densities, and the logarithmic formulation, where the dependent variables are logarithms of the species number densities. The original formulation has been found to be much more efficient for the steady-state modelling, and was used in all the simulations reported here. Calculations of the set of solutions describing a wide range of corona voltages/currents for each gap were performed separately for the positive and negative polarities. For each polarity, the first step was to find a solution describing the corona inception, as described in [63]. The second step was a series of computations with the corona current serving as a control parameter and being gradually increased. When the corona voltage has increased by about 200 V with respect to the inception voltage, the control parameter was switched to the corona voltage U and the computation proceeded with U being gradually increased until the whole range of current values of interest has been covered.

5.2.3 Experimental setup for point-to-plane coronas

Somewhat surprisingly, it seems that experimental data on corona discharges reported in the literature beyond the simplest one-dimensional wire-cylinder configuration are

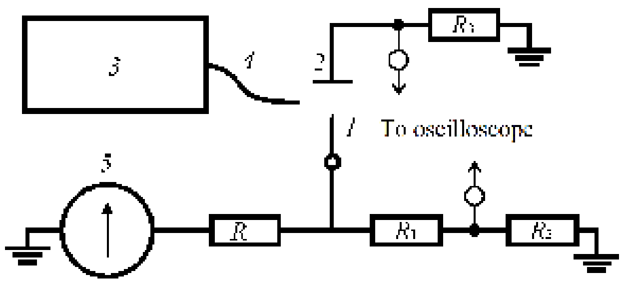

Figure 5.4: The experimental design: 1 - needle, 2 - plane electrode, 3 - spectrometer with a light guide 4 or a camera, 5 - a DC voltage source. R is the resistance limiting the discharge current; R_1 and R_2 are the resistances of the voltage divider; R_3 is the resistance of the current shunt.

insufficient for an accurate quantitative comparison: not all relevant geometrical parameters are indicated. For example, the rod length is a parameter omitted in experimental publications on corona discharges in the rod-to-plane configuration, e.g. works [8, 74], which can affect appreciably the inception voltage as seen in section 3.4.of chapter 3. As another example, one can mention wire coronas: they are very sensitive to the environment (e.g., [114]), meaning that the electrostatic boundary conditions are not well defined.

Therefore, special experiments have been performed (as mentioned before, not by the author of the thesis.) on point-to-plane coronas in a wide current range of currents of both polarities. The experimental setup was analogous to those typically used for studying corona discharges in point-plane gaps. It consists of needle and flat electrodes, power source, and recording equipment, and is shown in figure 5.4. A DC voltage source 5 is connected to the needle 1 through a resistance of $R = 18\,\mathrm{M\Omega}$. The polarity of the voltage source could be either positive or negative and the source can smoothly change the voltage U from 1 to 25 kV. In series with the plane electrode, the shunt is switched on through a resistance of $R_3 = 1\,\mathrm{k\Omega}$. The voltage across the gap is measured using a high voltage probe formed by the resistances R_1 and R_2. The electrode with a small radius of curvature is made of a 50 mm long copper needle with a diameter of 3 mm, having a tip radius of 0.2 mm (see figure 5.5). The plane electrode is mounted at a distance from the tip of the needle varying from 5 to 14 mm.

The measured parameters were the corona current, the voltage at the tip, and the radiation intensity distribution. The variation of voltage and current with time was recorded using a TDS 3034 oscilloscope (Tektronics, Inc.), a high-voltage probe, and a shunt. Moreover, when recording the discharge current, its average value was determined using the corresponding recording mode of the TDS 3034 oscilloscope. The average discharge current for each point was determined within 40 μs at a constant

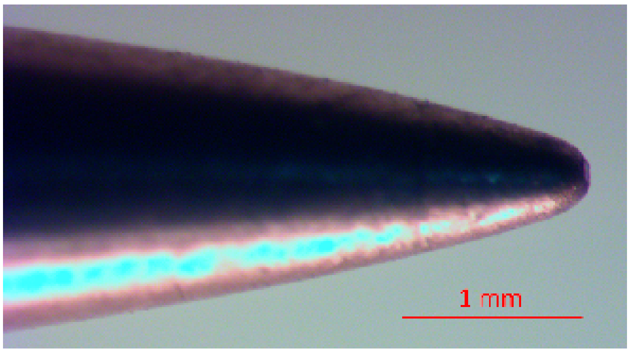

Figure 5.5: The needle electrode.

voltage across the gap, the value of which was set with an accuracy better than 1%. The voltage change during measurements of the average current also did not exceed 1%. Note that individual short pulses that were generated during $40\,\mu$s, in particular Trichel pulses, were taken into account when measuring the average corona discharge current. However, the generation of individual short pulses did not have a noticeable effect on the average corona discharge current.

Photos of the corona discharge were obtained with a Canon PowerShot SX 60 HS digital camera in the single-shot mode with an exposure time of 15 s. Corona emission spectra were recorded using an assembly that included a collimating lens with a focal length of 30 mm, an optical fiber with a known transmission spectrum, and an HR2000 + ES spectrometer (Ocean Optics, Inc.) based on a multi-channel CCD line Sony ILX511B (operating range $200 - 1100$ nm, spectral half-width of the hardware function ~ 1.33 nm).

The experiments were conducted in ambient atmospheric air under normal conditions. As the current-voltage characteristics (CVCs) are influenced by variation of pressure and humidity of ambient air, depending on weather conditions, the CVCs were measured during one day, in a time interval as short as possible.

5.2.4 Results on point-to-plane coronas

The computed (lines) and measured (points) CVCs of corona discharges both for positive and negative polarities of the tip electrode are shown in figure 5.6 for several values of the gap width d (i.e., the point-to-plane distance). Experimental points shown by triangles, closed circles, squares, and diamonds were obtained in the same day at the temperature of 21 °C, pressure of 747 mmHg (9.96×10^4 Pa), and air humidity of about 50%. For negative corona in one of the gaps, $d = 8$ mm, also shown are experimental data (open circles) measured in a different day at different atmospheric conditions: the temperature of 20 °C, pressure of 740 mmHg (9.87×10^4 Pa), and humidity of about

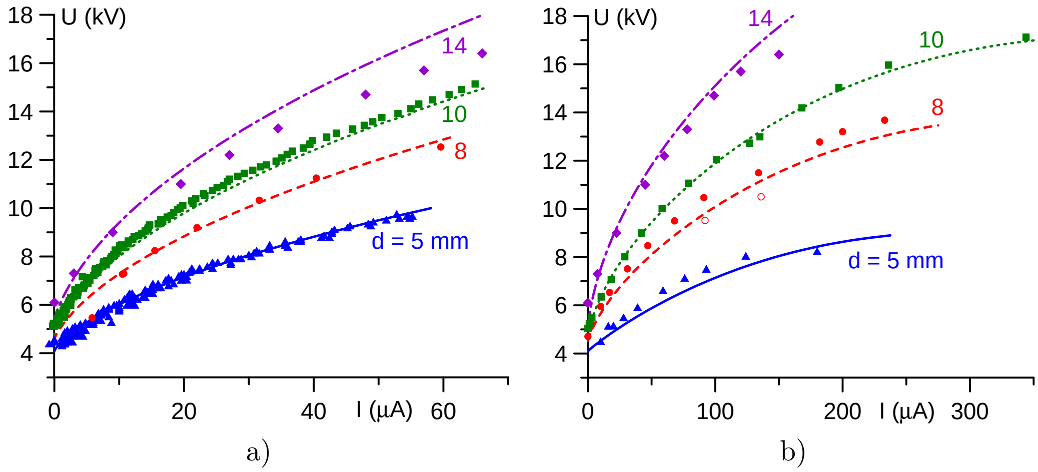

Figure 5.6: Current-voltage characteristics of positive (a) and negative (b) corona discharges in point-to-plane geometry for various values of the point-to-plane distance d. Air, 1 atm, Points: experiment. Lines: modelling.

60%.

The secondary electron emission coefficient in the modelling was set equal to 10^{-4}; a value which allowed to obtain the ignition corona voltage in agreement with the experiment. Note that the effect of variations of the secondary electron emission coefficient on inception of positive and negative corona between concentric cylinders was investigated in chapter 3 and it was seen that the agreement with experiment was lost for values of the secondary electron emission coefficient higher than 10^{-4}.

In all the cases, the calculated values agree well with the measured data. Note that the coefficient of determination R^2 equals 0.989, 0.967, 0.994, and 0.897 for the gaps of 5, 8, 10, and 14 mm, respectively, in the case of positive corona and 0.920, 0.975, 0.999 and 0.967 in the case of negative corona. (Here the coefficient of determination is defined as $R^2 = 1 - SS_{res}/SS_{tot}$, where SS_{res} is the residual sum of squares and SS_{tot} is the total sum of squares, so that $R^2 = 1$ corresponds to the exact match between the modelling and the experiment.)

A comparison of CVCs of positive and negative coronas shows that their inception voltages, for the same gap d, are rather close. However, the current I_n in a negative corona is two to three times higher than the current I_p in a positive corona at the same applied voltage U, the ratio I_n/I_p decreasing with increase in d. Note that a similar effect of the gap width variation has been observed in the experiment [40]. Note also that the differences in current for different corona polarities reported in the recent experiment [115] were smaller than in this work, which is consistent with the longer

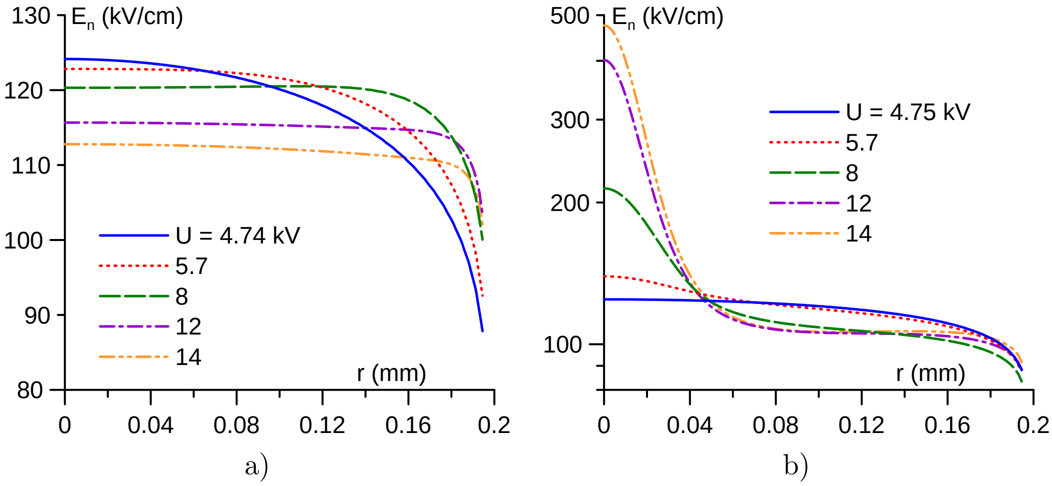

Figure 5.7: Distributions of the normal electric field along the needle surface at various applied voltages in positive (a) and negative (b) corona discharges. $d = 10\,\mathrm{mm}$.

gap being used in [115] (20 mm).

Results of simulation show a substantial difference in spatial distributions of time-averaged electric field inside positive and negative corona discharges. Distributions of the normal electric field E_n along the needle surface for both polarities, $d = 10\,\mathrm{mm}$, and various applied voltages are shown in figure 5.7. Here r is the distance to the discharge axis. In the case of positive coronas (figure 5.7a), the profiles broaden with increase in U and the electric field E_0 at the tip (at $r = 0$) decreases slightly. An opposite trend takes place in negative coronas (figure 5.7b), where an increase in U results in a substantial (up to four times in the voltage range considered) increase of E_0 and appearance of a pronounced maximum close to the axis. Note that similar profiles of E have been obtained in simulations [108] of positive and negative DC air coronas in a sphere-plane gap.

Distributions of the axial electric field E_z along the axis are shown for both polarities, various applied voltages, and $d = 10\,\mathrm{mm}$ in figure 5.8. Here z is the distance from the tip of the needle electrode. In the case of positive corona (figure 5.8a), the electric field in the ionization region (the region where E exceeds the critical field, of about $25\,\mathrm{kV\,cm^{-1}}$, which corresponds to equality of ionization and attachment coefficients) depends on U rather weakly, while the electric field in the drift region increases with increasing U. Such pattern is similar to that in corona discharges in axially symmetric wire-cylinder gaps [1]. Note that the computed electric field in the ionization region being virtually independent of the applied voltage is consistent with the classic Kaptzov assumption. This assumption, which states that the steady state electric field at

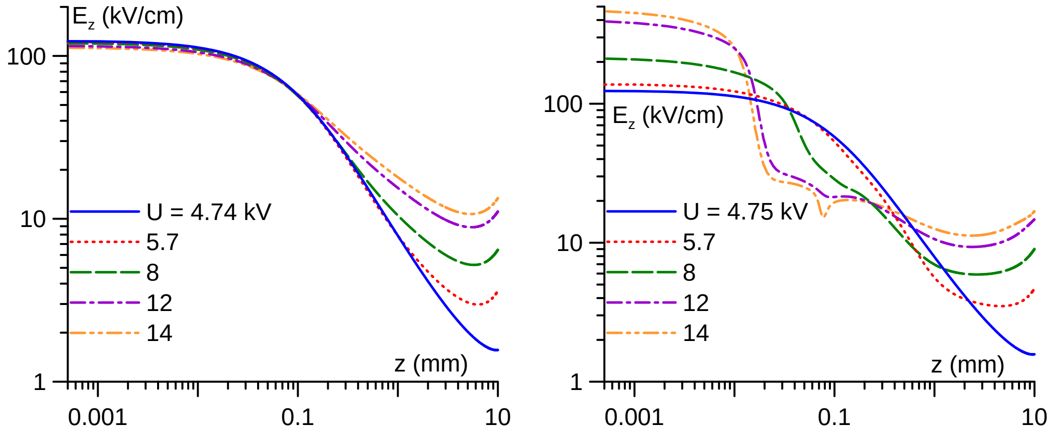

Figure 5.8: Distributions of the axial electric field along the discharge axis at various applied voltages in positive (a) and negative (b) corona discharges.

the wire surface in a (one-dimensional) wire-cylinder gap remains at the corona onset value, is widely used in the corona discharge theory and can be traced back to a classic work of Townsend of 1914 [37]. It is remarkable that in the case considered here this assumption is valid in a two-dimensional geometry.

The computed axial distribution of the electric field in the negative corona (figure 5.8b) is quite different. The electric field in the ionization region increases appreciably with increasing discharge voltage. Thus, the Townsend-Kaptzov assumption is not valid in this case. The width of the ionization region decreases substantially with increase in U. At high voltages, a local minimum in E at the outer boundary of the ionization region is formed. Note that the ionization integral, evaluated along the discharge axis over the ionization region, varies with voltage between 7.7 and 9.2, i.e., not very strongly.

Figure 5.9 shows the distributions of normalized densities $j(\theta)/j(0)$ and $j_{el}(\theta)/j(0)$ of the total and electron currents over the plane electrode, in negative corona discharges at the current $I = 100\,\mu$A, in two gaps, with the widths of 5 and 14 mm. Here θ is the angle between the axis and the line connecting the tip and the point of the plane being considered. The electron current gives a substantial contribution to the total current for both gaps. The ratio $j_{el}(0)/j(0)$ at the axis and the width of the $j_{el}(\theta)/j(0)$ distribution are larger in the smaller gap; a result that is easy to understand: fraction of the electrons that attach, during their drift from the ionization region to the plane electrode, to oxygen molecules is lower for the smaller gap, hence the contribution of electron current is higher.

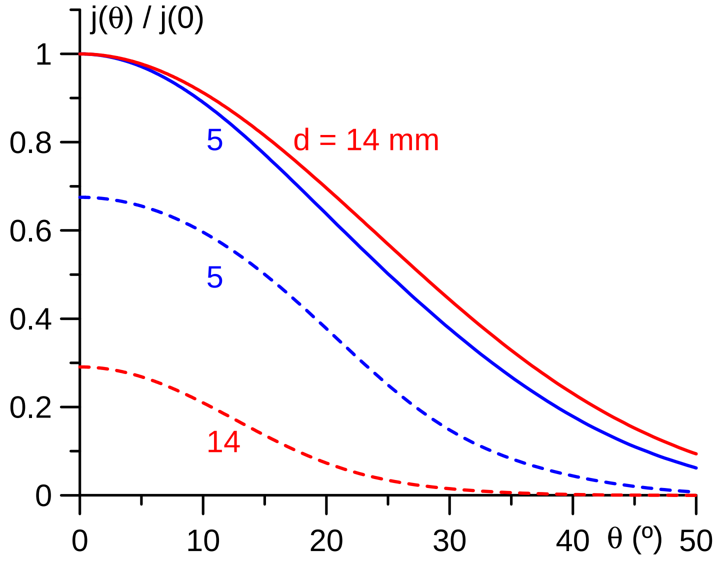

Figure 5.9: Distributions of normalized total (solid) and electron (dashed) current densities in negative corona discharges over the plane electrode.

The effect of shortening of the gap in the negative corona is demonstrated also in figure 5.10, where axial distributions of the normalized densities of the currents transported by the positive ions, $j_p(z)/j(z)$, the negative ions, $j_n(z)/j(z)$, and the electrons, $j_{el}(z)/j(z)$, are shown for $I = 100\,\mu$A. The current j_p dominates current transport in the ionization region, j_{el} gives the major contribution in a part of the drift zone adjacent to the ionization region, and j_n comes into play in the outer part of the drift zone. The distance l from the cathode where the values of j_n and j_{el} become comparable (the attachment length) is, for both gaps, of about 3 mm.

In long gaps, where $d/l \gg 1$, the corona current in the most part of the drift zone is transported by the negative ions. As the mobilities of the negative and positive ions are close to each other, the difference between the CVCs of negative and positive coronas for longer gaps is lower than for shorter ones, as seen in figure 5.6.

Spatial distributions of the intensity of visible radiation emitted by corona discharges differ substantially depending on the tip polarity. Figure 5.11 shows the computed distributions (on a logarithmic scale) of the excitation rate R_C of radiating nitrogen states N_2 (C), which are the main source of visible radiation emitted by air coronas for both polarities. It was evaluated as $R_C = K_C n_{N_2} n_e$, where K_C is the excitation rate constant, which is governed by the local reduced electric field value and was found with the use of the online version of the Bolsig+ solver [116] and the cross sections [117], n_e is the electron density, and n_{N_2} is the number density of the nitrogen molecules. Also shown in figure 5.11 are images of positive and negative coronas for

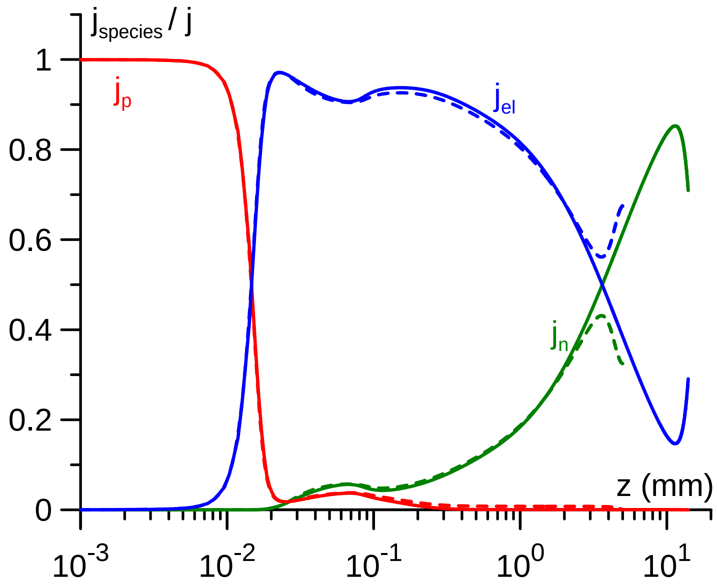

Figure 5.10: Distributions of normalized densities of the current transferred by the positive ions, the negative ions, and the electrons in negative corona discharges along the discharge axis. Dashed: $d = 5\,\mathrm{mm}$. Solid: $d = 14\,\mathrm{mm}$.

various applied voltages, recorded in the experiment.

According to both the computations and the experiment, radiating regions in the positive corona have smaller sizes than those in the negative corona for comparable applied voltages and are positioned closer to the needle. These polarity effects are caused by the differences in spatial distributions of n_e and E (governing R_C values) in the high-field zone near the tip. In particular, the maximum of n_e in the ionization regions of positive coronas occurs at the needle surface, so that R_C is the highest at the surface as well. In negative coronas, n_e increases in the direction to the plane electrode, reaching the maximum at the boundary between ionization and drift regions. As a result, the maximum of R_C in this case occurs at some distance from the tip. A peculiar spatial distribution of the radiation intensity in negative coronas, seen in the bottom two rows of figure 5.11, was obtained also in [108] and is governed by the specifics of n_e and E distributions. In particular, a radial constriction of the electric field at the tip (Fig. 4b) results in a constriction of the radiation intensity.

5.3 Summary and concluding remarks

The use of a stationary solver, which solves steady-state equations by means of an iterative process unrelated to time relaxation, allows one to develop a very fast and robust numerical model for evaluation of time-averaged characteristics of corona dis-

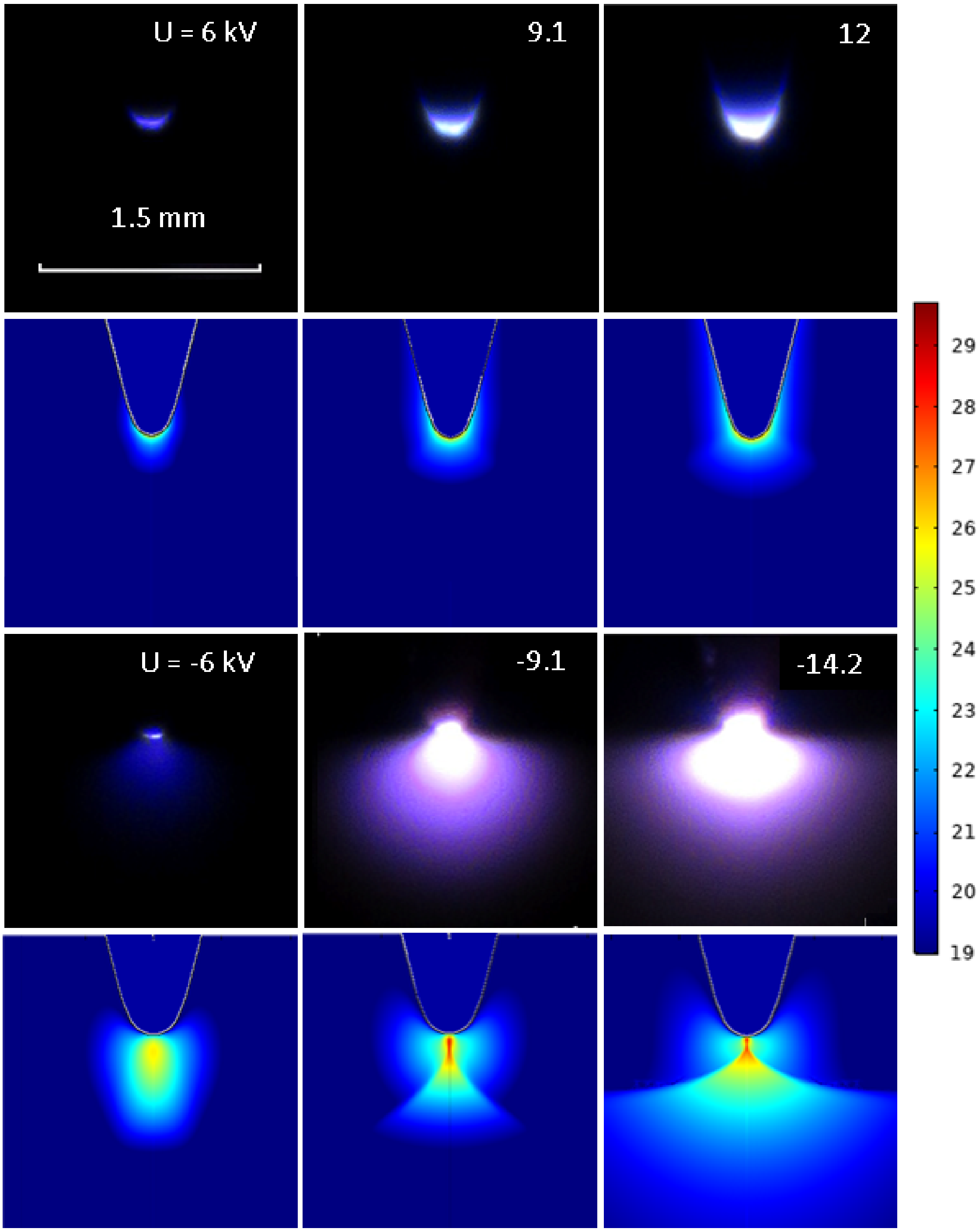

Figure 5.11: Images of point-to-plane corona discharges and computed distributions of the rate of excitation of radiating N_2 (C) levels (in $m^{-3}\,s^{-1}$, logarithmic scale). Air, 1 atm, point-to-plane distance 14 mm. Upper two rows: positive corona. Bottom two rows: negative corona.

charges. The same model of plasmachemical processes in low-current discharges in ambient air, detailed and employed in the previous chapters and involving positive and several negative ion species, is applied in particular to positive and negative DC corona discharges in point-plane gaps in air. A wide range of currents of both polarities and various gap lengths are investigated and the simulation results are validated by comparing the computed current-voltage characteristics and spatial distributions of the radiation intensity with the experimental data.

The calculated current-voltage characteristics are in good agreement with the measured data. This supports the choice of the set of ion mobilities that are used in the model, and detailed in Appendix A, with account of the possible formation of complex and cluster ions in the drift zone of corona discharges in air. Note that simulations performed with these mobility values give the current-voltage characteristics that are in good agreement with the experiment not only in 1D concentric cylinders and point-to-plane gaps, but also for other geometries of corona discharges in air [63]. The time-average electric field distribution in a negative corona discharge in an axially symmetric wire-cylinder gap in air, computed by means of this model, is in good agreement with the measurements [44], as shown in section 5.2.2.

Computational and experimental results show that average currents I_n in negative coronas are several times higher than the currents I_p in positive coronas for the same gap length and applied voltage, the ratio I_n/I_p being smaller in longer gaps. Calculated distributions, along the discharge axis and along the plane electrode, of contributions of electrons and negative ions to the total current density in negative coronas show that the fraction of the electrons that attach to O_2 molecules during the drift of electrons, produced in the ionization region, to the plane anode, is lower for smaller gaps, thus ensuring a higher contribution of the current transported by the electrons to the total current and hence a higher I_n/I_p ratio.

The spatial distributions of the intensity of the corona discharge radiation are computed. While only a thin region adjacent to the tip emits radiation in positive coronas, the radiating region in negative coronas is much wider and has a rather complex structure. For both polarities, specific features of the calculated distributions of radiation intensity are in a reasonable agreement with the experimental data.

One of the advantages that stationary solvers offer in simulations of steady-state discharges, when compared to standard approaches that rely on time-dependent solvers, is the fact that stationary solvers are not subject to the Courant-Friedrichs-Lewy criterion or analogous limitations on the mesh element size. The removal of limitations on the mesh element is particularly important for modelling of discharges with strongly varying length scales, as is the case of corona discharges. In the modelling of point-to-plane gaps the mesh element size varied from fractions of micrometer at the corona

U (kV)	I (μA)	SS	TDS
5.0	3.76	–	–
5.05	4.03	39 s	58 min
5.1	4.29	50 s	5 h20 min

Table 5.1: Computation of solutions for $U = 5.05$ and 5.1 kV starting from the solution for $U = 5$ kV . Positive corona, gap 5 mm . SS: stationary solver computation time. TDS: time-dependent solver computation time.

electrode surface to tens of micrometers far away from the corona electrode and the reduction of computation time was dramatic. An example is shown in Table 5.1. The task was to compute the solutions for $U = 5.05$ and 5.1 kV by means of stationary and time-dependent solvers, using as an initial approximation or initial condition, respectively, the previously computed solution for $U = 5$ kV. The mesh in all the computations was the same and included 14500 finite elements. The damping factor in all the computations and the time stepping in the time-dependent solver were set to automatic/default. The computation times shown in the table refer to a computer with a CPUs with four cores, having the clock rate of 4 GHz. Criterion for defining the computation time for the time-dependent solver was the discharge current to be within 10^{-3} of its final value, which happened within approximately 1 ms of the discharge development. One can see that the stationary solver is by several orders of magnitude faster than the time-dependent solver.

It is interesting to note that it was not possible to perform similar computations by means of the time-dependent solver for the negative corona, presumably because the glow negative corona is unstable. In this case, the time-dependent solver can be used to study the spatiotemporal evolution of the discharge, however it is not suitable for a direct calculation of time-averaged characteristics. This illustrates another useful feature of stationary solvers: they allow decoupling of physical and numerical stability. Further examples of manifestation of this feature in gas discharge modelling can be found in [46].

Chapter 6

Conclusions of the thesis

An approach for simulation of low-current quasi-stationary discharges in high-pressure air has been developed. This approach is applicable not only to DC but also to low-frequency (e.g., 50 Hz) electric fields, and bridges the gap between modern methods of numerical modelling and engineering approaches. Such approach is implemented as a part of a numerical model that allows determining the ignition and breakdown voltages, a very important matter for applications. In addition, it is also of theoretical interest since it is desirable to have first-principle based approaches complementing the empirical ones. A 'minimal' kinetic model of plasmachemical processes has been considered. The kinetic scheme takes into account electrons, an effective species of positive ions, and negative ions O_2^-, O^-, and O_3^-. The relevant kinetic and transport coefficients are explained and detailed in Appendix A. The implementation of the numerical model is based on the use of stationary solvers, which offer important advantages in simulations of quasi-stationary discharges.

The developed numerical model is validated by a comparison of inception voltage of glow corona discharges, computed in a wide range of conditions, with several sets of experimental data. A good agreement with experimental data has been obtained for positive coronas between concentric cylinders in a wide range of pressures and diameters of the cylinders, which attests to the suitability of the kinetics employed. The sensitivity of the computation results with respect to different factors is illustrated: the kinetic scheme used; the photoionization and a boundary condition for the photoionization rate at solid surfaces; the secondary emission from the cathode. Concerning the kinetic scheme, the disregard of detachment results in an increase of the inception voltage as it should. On the other hand, computations without account of both attachment and detachment suggest that the detachment approximately compensates the attachment. In what concerns photoionization, it is shown that the effect of pressure on the reduced inception field (at given pr_0), observed in the experiments, could hardly be explained without photoionization -.there is a decrease of photoionization rate with growth of pressure, originating in collisional quenching of nitrogen radiating states. There is an appreciable deviation of the inception field computed without account of photoionization from the experimental data, where the reduced inception field increases if photoionization is not taken into account. The use of the boundary condition $\partial S_{ph}^{(j)}/\partial n = 0$ for the rate of photoionization at the inner cylinder or at both electrodes does not change significantly the inception field, meaning that the loss of photons on the outer electrode is a minor effect, which is expected. The values of the inception field are sensitive to the choice of the boundary condition for photoionization at the anode for low pressures, where the use of $S_{ph}^{(j)} = 0$ is the only case producing good agreement with experiments. For higher values of pressure, the effect of the boundary condition for photoionization at the anode is attenuated. Finally, concerning the sensitivity of the computation results with respect to the secondary emission from the cathode, modelling for positive coronas shows, as expected, the decrease of reduced inception field with increase of γ. Good agreement with the experiments is seen for γ not exceeding 10^{-4}, which is the order of magnitude of real values of γ in air for low E/p values at the cathode surface [76]. In the case of negative coronas, due to high electric fields at the surface of the smaller electrode, values of the secondary electron emission coefficient appropriate for negative coronas are higher than those for positive coronas. The voltage computed with γ of 10^{-4} to 10^{-3}, taken in agreement with [77], agrees well with the experimental data. The computed reduced inception field, considered as a function of pr_0, does not reveal a visible dependence on r_0 (or, equivalently, pressure), in agreement with the experiment. This contrasts the case of positive coronas and is a consequence of the role of photoionization being minor for negative coronas. Modelling with the same set of γ values, independent of pressure, allows the evaluation of the negative corona inception field, for different electrode radii and materials, in agreement with the experiment.

A simplified kinetic model for corona discharges has been proposed and validated. The simplified model does not include conservation equations for negative ion species and accounts for ion-molecular reactions by means of the effective attachment rate in the conservation equation for electrons. The ionization integral evaluated with the use of this model at corona inception voltage varies significantly for positive coronas; in the case of negative coronas, the ionization integral varies much less and is not very different from $\ln\left(1+\gamma^{-1}\right)$, as could be expected.

The numerical model was extended to 2D simulations and the inception voltage of positive glow coronas in the rod-to-plane electrode configuration was computed. The simulation results qualitatively agree with experimental data and the modelling has shown that the inception voltage is affected by the rod length, a parameter omitted in experimental papers. A good quantitative agreement with the experiment can be obtained by variation of the rod length in the modelling.

The effect of microprotrusions on the surface of the inner electrode in corona-like discharge configurations was studied by means of 2D numerical modelling. The voltage corresponding to the initiation of a self-sustaining discharge was computed over a wide range of pressures. The model describes, in a natural way, the enhanced ionization of air molecules in regions of amplified electric field near the microprotrusion. The aim was to find out if the latter mechanism may be responsible for the deviations from the similarity law at high pressures, observed in the experiment. The model was applied to conditions of corona inception and breakdown experiments on concentric cylinders over a wide pressure range described in [9, 64]. An axially symmetric geometry consisting of concentric sphere electrodes with a single cylindrical or conical microprotrusion on the surface of the inner electrode was considered. Since different protrusions come into play under different conditions, the presence of several microprotrusions acting in close proximity is unlikely. (Note that this reasoning does not apply to arrays of identical protrusions, nevertheless it is interesting to mention in this connection the recent experiments [105], which showed little effect of the number of protrusions in the array for the case of SF_6 but a more appreciable effect for the case CO_2; figures 7-8 and 12-13 of [105], respectively. This is an interesting point that may need to be revisited in the future.) On the other hand, microprotrusions that are not located close to each other do not interact. Therefore, the assumed computational geometry with a single protrusion seemed to be sufficient for a qualitative study while avoiding 3D modelling, which is demanding and unwarranted at this stage. The reported results refer to conical protrusions with a 60° full aperture angle and a spherical tip with a radius of $2\,\mu$m and cylindrical protrusions of a radius of $2\,\mu$m with a half-spherical tip, the protrusion heights being of several tens of micrometers in both cases. While the cylindrical protrusion is slender, the conical protrusion is not and the electric field amplification is due to high values of the ratio of the height of the protrusion to the tip radius.

For pressures in the range of $0.5-3$ atm ($5.07\times10^4-3.04\times10^5$ Pa), the discharge is not appreciably affected by the presence of the protrusion and is distributed along the surface of the inner electrode in a more or less uniform way. The computed ignition field is close to the experiment and to values given by empirical Peek's formula and increases with p approximately proportionally, in agreement with the similarity law. For higher values of the pressure, the discharge concentrates in the vicinity of the protrusion and the increase of the computed ignition field with pressure slows down, in agreement with the experimental data. The protrusion heights necessary to achieve a qualitative agreement with the experiment are of the order of $50\,\mu$m in all the cases.

In the case where the inner electrode is positive, the enhanced ionization of air molecules in regions near microprotrusions on the electrode surface appears to be the only possible explanation for the deviations from the similarity law at high pressures, observed in the experiments [9, 64]. The qualitative agreement of the simulation results with the experiment can be considered as indirect evidence of the existence of microprotrusions and indicates what height of microprotrusion is necessary to produce the effect: on the order of tens of micrometers. The protrusions need not necessarily be slender; e.g., conical protrusions with a large ($60\,^\circ$) aperture angle and a small tip curvature radius produce a similar effect. Ridge protrusions produce a similar effect as well, however a bigger height or a smaller tip curvature radius is required. This aspect is important since protrusions that are not slender appear to be more realistic than needle-like ones. It should be stressed that, although high values of the ratio of the protrusion height to the tip radius are required for electric field amplification and hence represent a necessary condition for the deviations from the similarity law at high pressures observed in [9, 64], this condition alone is not sufficient: the protrusion height must be not too small, otherwise the electric field decays at very small distances from the protrusion tip and sufficient ionization is not produced. Thus, while the above-mentioned values of microprotrusion height of several tens of micrometers may appear rather high, there seems to be no other explanation at present.

The enhanced ionization of air molecules in regions near protrusions on the electrode surface explains also the deviations from the similarity law at high pressures observed in the experiments [64] in the case where the inner electrode is negative. Another mechanism that may play a role in this case is the enhanced electron emission from the cathode surface; the same mechanism which causes deviations from the Fowler-Nordheim formula in experiments on field electron emission from cold cathodes in vacuum and which may occur due a variety of reasons, such as amplification of the applied electric field by microprotrusions on the cathode surface, local reduction of the work function of the cathode material, 'nonmetallic' electron emission mechanism, plasmons. The enhancement of the field emission due to the amplification of the electric field was estimated and it was found that in the range of values of the protrusion aspect ratio where the enhanced ionization of air molecules in the gas phase comes into play the field emission is still insignificant.

Modelling has shown that the experiments on positive corona discharge ignition and breakdown at high and very high pressures can serve as a useful, albeit inevitably indirect, source of information about microprotrusions on the surface of electrodes. Unfortunately, the experimental information available is clearly insufficient. One of important questions to be answered is the relation between the deviations from the similarity law and the degree of polishing of the inner electrode. Note that experimental results reported in [9] refer to four values of the inner cylinder radius: 0.089 mm, 0.216 mm, 1.20 mm, and 3.18 mm. Deviations from the similarity law, found in the modelling with the same protrusion height of 50 μm, were comparable for all the four values. The deviations found in the experiment [9] were comparable for the radii of 1.20 mm and 3.18 mm (cf. figures 4.4 and 4.5 above), were significantly smaller for 0.216 mm, and still smaller for 0.089 mm. Of course, microprotrusions on different cylinders need not be the same; in particular, it is unclear if 50 μm protrusions are likely to occur on a wire of a radius of 89 μm. Hopefully, the relation between the deviations from the similarity law and the degree of polishing of the inner electrode will be addressed in future experiments.

The same numerical model was used for evaluation of time-averaged characteristics of corona discharges in a robust and very fast way. This is possible through the use of a stationary solver, which solves steady-state equations by means of an iterative process unrelated to time relaxation. The same model of plasmachemical processes in low-current discharges in ambient air, involving positive and several negative ion species, was applied in particular to positive and negative DC corona discharges in point-plane gaps in air. A wide range of currents of both polarities and various gap lengths were investigated and the simulation results were validated by comparing the computed current-voltage characteristics and spatial distributions of the radiation intensity with the experimental data.

The calculated current-voltage characteristics are in good agreement with the measured data. This supports the choice of the set of ion mobilities that are used in the model, and detailed in Appendix A, with account of the possible formation of complex and cluster ions in the drift zone of corona discharges in air. Note that simulations performed with these mobility values give the current-voltage characteristics that are in good agreement with the experiment not only in 1D concentric cylinders and point-to-plane gaps, but also for other geometries of corona discharges in air [63]. The time-average electric field distribution in a negative corona discharge in an axially symmetric wire-cylinder gap in air, computed by means of this model, is in good agreement with the measurements [44], as shown in section 5.2.2.

Computational and experimental results have shown that average currents I_n in negative coronas are several times higher than the currents I_p in positive coronas for the same gap length and applied voltage, the ratio I_n/I_p being smaller in longer gaps. Calculated distributions, along the discharge axis and along the plane electrode, of contributions of electrons and negative ions to the total current density in negative coronas show that the fraction of the electrons that attach to O_2 molecules during the drift of electrons, produced in the ionization region, to the plane anode, is lower for smaller gaps, thus ensuring a higher contribution of the current transported by the electrons to the total current and hence a higher I_n/I_p ratio.

The spatial distributions of the intensity of the corona discharge radiation were computed. While only a thin region adjacent to the tip emits radiation in positive coronas, the radiating region in negative coronas is much wider and has a rather complex structure. For both polarities, specific features of the calculated distributions of radiation intensity are in a reasonable agreement with the experimental data.

One of the advantages that stationary solvers offer in simulations of steady-state discharges, when compared to standard approaches that rely on time-dependent solvers, is the fact that stationary solvers are not subject to the Courant-Friedrichs-Lewy criterion or analogous limitations on the mesh element size. The removal of limitations on the mesh element is particularly important for modelling of discharges with strongly varying length scales, as is the case of corona discharges. In the modelling of point-to-plane gaps the mesh element size varied from fractions of micrometer at the corona electrode surface to tens of micrometers far away from the corona electrode and the reduction of computation time was dramatic. An example is given for point-to-plane positive corona in a gap of 5 mm. The computed solutions for $U = 5.05\,\mathrm{kV}$ by means of stationary and time-dependent solvers, using as an initial approximation or initial condition, respectively, the previously computed solution for $U = 5$ kV, took 39 s and 58 min respectively. For the solution $U = 5.1\,\mathrm{kV}$, the computation times for the stationary and time-dependent solvers were 50 s and 5 h20 min respectively. One can see that the stationary solver is by several orders of magnitude faster than the time-dependent solver. It is interesting to note that it was not possible to perform similar computations by means of the time-dependent solver for the negative corona, presumably because the glow negative corona is unstable. In this case, the time-dependent solver can be used to study the spatiotemporal evolution of the discharge, however it is not suitable for a direct calculation of time-averaged characteristics. This illustrates another useful feature of stationary solvers: they allow decoupling of physical and numerical stability. Further examples of manifestation of this feature in gas discharge modelling can be found in [46].

Inception of corona and time-averaged characteristics of corona discharges are only two examples of discharges that may be studied with the model developed in this thesis; one can hope that the model may also be used, with appropriate modifications, for investigation of discharges of other types, for instance, in the study of ionic wind thrust performance generated by electrohydrodynamic propulsion devices (e.g., [118, 119] and references therein).

Appendix A

Kinetic model

This appendix concerns the details of the 'minimal' kinetic model of plasmachemical processes in low-current discharges in high-pressure air used in this thesis. The kinetic scheme takes into account the electrons, one species of positive ions, which are represented mostly by O_2^+, and three species of negative ions, O_2^-, O^-, and O_3^-, and comprises the processes shown in Table A.1: electron impact ionization (reaction 1, $e + M \to 2e + A^+$), two-body (dissociative) attachment (2, $e + O_2 \to O^- + O$), three-body attachment (3, $e + O_2 + M \to O_2^- + M$), photoionization (4, $M + h\nu \to e + A^+$), collisional detachment from O_2^- (5, $O_2^- + O_2 \to e + 2O_2$), associative detachment from O^- (6, $O^- + N_2 \to e + N_2O$), charge transfer from O^- to O_2^- (7, $O^- + O_2 \to O + O_2^-$), conversion of O^- to O_3^- (8, $O^- + O_2 + M \to O_3^- + M$), and ion-ion (9, $A^+ + B^- \to$ products) and electron-ion recombination (10, $A^+ + e \to$ products). In reaction 4 of Table A.1, concerning photoionization, the reaction is first written in the point of view of the model, concerning the products generated (an electron and a positive ion), and then, in parenthesis, the reaction is written as the sequence of steps through which the physical process takes place.

The local-field approximation is employed, i.e., the electron transport and kinetic coefficients are assumed to be dependent on the local reduced electric field E/N only. (Here E is the electric field strength and N is the number density of gas molecules.)

The longitudinal and transversal electron diffusion coefficients were evaluated with the use of the online version of the Bolsig+ solver [116] and the cross sections [117]. The diffusion coefficients of all ion species are related to the mobilities through Einstein's relation, which requires the corresponding effective ion temperatures. One can consider an effective temperature T_i of an ion species i, which characterizes the mean kinetic energy of the chaotic motion of the ions and is defined by the equation $\frac{1}{2}m_i\overline{(\mathbf{v}_i - \mathbf{v}_{di})^2} = \frac{3}{2}kT_i$. Here $\mathbf{v}_i$, m_i, and $\mathbf{v}_{di}$ are the particle velocity, particle mass, and average (drift) velocity of species i. The temperature T_i may be evaluated by means of the Wannier formula in the form

$$\frac{3}{2}kT_i = \frac{3}{2}kT + \frac{1}{2}Mv_{di}^2, \tag{A.1}$$

e.g., Eq. (6-2-13b) on p. 276 of [120]. Here T is the gas temperature, and M is the particle mass of the neutral gas (in the case of air it is interpreted as a weighted average of N_2 and O_2 particle masses). The two components in Eq. (A.1) are the thermal energy acquired by collisions with the gas ($3kT/2$) and the part of the chaotic energy due to the drift motion ($Mv_d^2/2$). It is natural to use the effective temperature T_i while evaluating Einstein's relation for the species i. Both Einstein's relation and the Wannier formula are accurate in the case of ions with a constant mobility.

For evaluation of reaction rate constants, it is relevant to also evaluate the mean kinetic energy of relative motion of particles of species i and j, which is characterized by the effective reduced temperature T_{ij} and is defined by the equation $\frac{1}{2}m_{ij}\overline{(\mathbf{v}_i - \mathbf{v}_j)^2} = \frac{3}{2}kT_{ij}$, where $m_{ij} = m_i m_j / (m_i + m_j)$ is the reduced mass of the species. It can be shown that

$$\frac{3}{2}kT_{ij} = \frac{3}{2}k\frac{m_i T_j + m_j T_i}{m_i + m_j} + \frac{1}{2}m_{ij}\left(\mathbf{v}_{di} - \mathbf{v}_{dj}\right)^2. \tag{A.2}$$

The factor $(m_i T_j + m_j T_i) / (m_i + m_j)$ in the first term on the rhs of Eq. (A.2) is the so-called reduced temperature of the species i and j, so the physical meaning of this equation is clear.

Of special interest is the particular case of ion-neutral collisions, which is relevant for evaluation of rate constants of binary ion-neutral reactions. Setting in Eq. (A.2) $v_{dj} = 0$, $m_j = M$, and $T_j = T$, one obtains $T_{ij} = T_i$, which shows that Eq. (A.2) is consistent with the well-known fact that the mean kinetic energy of relative motion of ions and neutrals is characterized by the effective ion temperature. Another special case of particular interest is the one of collisions of positive and negative ions, which is relevant for evaluation of rate constants of binary ion-ion recombination reactions. In this case, one may replace the factor $(\mathbf{v}_{di} - \mathbf{v}_{dj})^2$ in Eq. (A.2) with $(v_{di} + v_{dj})^2$.

Thus, both Einstein's relation and rate constants of ion-neutral reactions are governed by the ion temperature T_i, which characterizes the mean kinetic energy of chaotic motion of the ions and may be evaluated by means of the Wannier formula in the form of Eq. (6-2-13b) on p. 276 of [120]; see Eq. (A.1) above. The rate constants of ion-ion recombination reactions are governed by the effective reduced temperature T_{ij}, which is expressed in terms of the ion temperatures T_i and T_j. Strictly speaking, the use of the effective ion temperature T_i or the reduced temperature T_{ij} for the evaluation of rate constants is justified in the case of binary reactions. However, in the absence of better alternatives it is natural to use these temperatures also in the case of three-body reactions, where the third body is a neutral particle, in the same way as the effective ion temperature is used for evaluation of rate constants of three-body ion-molecular reactions with the third body being a neutral particle.

The rates of electron impact ionization, reaction 1 in Table A.1, and two- and three-body attachment, reactions 2 and 3, are evaluated in terms of the Townsend coefficients, which are related to the corresponding reaction rate constants k_i by the conventional formulas

$$\alpha = \frac{k_1 N}{\mu_e E}, \quad \eta_2 = \frac{k_2 n_{O_2}}{\mu_e E}, \quad \eta_3 = \frac{k_3 n_{O_2} N}{\mu_e E}. \tag{A.3}$$

The Townsend ionization coefficient is evaluated by means of an expression approximating the experimental data compiled in [121] and recent experimental data [122]:

$$\frac{\alpha}{N} = \begin{cases} 1.64 \times 10^{-20} \exp\left[-\frac{680}{(E/N)}\right] \text{ m}^2, & \text{if} \quad E/N < 186 \text{ Td}, \\ \left[1 + \frac{6\times 10^6}{(E/N)^3}\right] 5 \times 10^{-20} \exp\left[-\frac{1010}{(E/N)}\right] \text{ m}^2, & \text{if} \quad E/N > 186 \text{ Td}. \end{cases} \tag{A.4}$$

In figures A.1 and A.2 the ionization rate constant and the Townsend ionization coefficient in air determined with the use of Eq. (A.4) are shown along with the experimental data from [122] and [121], respectively. Also shown in figure A.1 is the ionization rate constant determined with the use of the online version of the Bolsig+ solver [116] and the cross sections [117]. Note that a detailed discussion of the ionization rate constant for air at low reduced electric fields can be found in [123].

The Townsend coefficient of the two-body (dissociative) attachment, reaction 2 of Table A.1, is given by Eq. (A.5) which represents a modification of the expression for the rate constant given in [124], reaction 20 in Table A1 of [124]. (The factor of 0.8 was introduced to fit new experimental data [122]. The vibrational temperature in typical conditions of corona discharge does not significantly exceed the translational temperature, therefore the factor F in the expression [124], which accounts for gains in electron energy in collisions with vibrationally excited nitrogen molecules, or, in other words, for the effect of non-zero vibrational temperature, was dropped.)

$$\frac{\eta_2}{N} = 3.44 \times 10^{-23} \exp\left[-1.05\left|5.3 - \ln(E/N)\right|^3\right] \text{ m}^2 \tag{A.5}$$

In figure A.3 the rate constant of dissociative attachment, computed using Eq. (A.5), is shown along with recent experimental data [122]. Also shown in figure A.3 are values determined with the use of the online version of the Bolsig+ solver [116] and the cross sections [117]. It is seen that the approximation (A.5) is in reasonable agreement with the data [122], however one should keep in mind that the available experimental data have a significant scatter; e.g., figure 6 of [123].

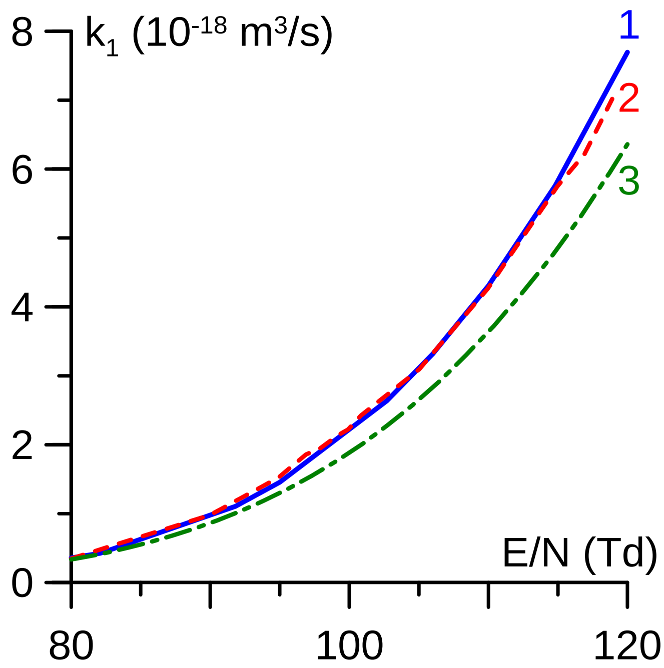

Figure A.1: Ionization rate constant. 1: evaluation with the use of equation (A.4). 2: experimental data for air from figure 5b of [122]. 3: evaluation with the use of the online version of the Bolsig+ solver [116] and the cross sections [117].

The mobility of the electrons μ_e was taken from [125] and is written as $\mu_e N = 3.74 \times 10^{24}(E/N)^{-0.25}\,(\mathrm{V\,m\,s})^{-1}$, where E/N is in Td. Concerning the evaluation of transport coefficients of the ion species, special care is required to study time-averaged characteristics of DC corona discharges: while values of ion mobilities do not affect appreciably the inception voltage of corona discharges, which is the parameter computed in chapters 3 and 4, values of ion mobilities in the drift zone do affect the corona current-voltage characteristics studied in chapter 5. The ions produced in air by the electron impact ionization are N_2^+ and O_2^+. However, the N_2^+ ions in air at pressures about 1 atm (1.01×10^5 Pa) and higher are rapidly converted into O_2^+. One channel of such conversion is the fast charge transfer reaction $N_2^+ + O_2 \rightarrow O_2^+ + N_2$. Another channel comprises a three-body conversion process of N_2^+ and N_2 molecules into the N_4^+ ions, followed by the charge transfer from N_4^+ to O_2. Ions O_2^+ are generated also by the photoionization, which is produced by UV radiation emitted by N_2 molecules excited by electron impact. Therefore, the positive ions in the ionization (active) zone are represented mostly by O_2^+.

The modelling of this thesis is aimed primarily at computing the discharge ignition voltage and the neutral gas is still cold at the discharge ignition, hence the neutral gas temperature is set equal to 300 K. If the reduced electric field E/N is sufficiently

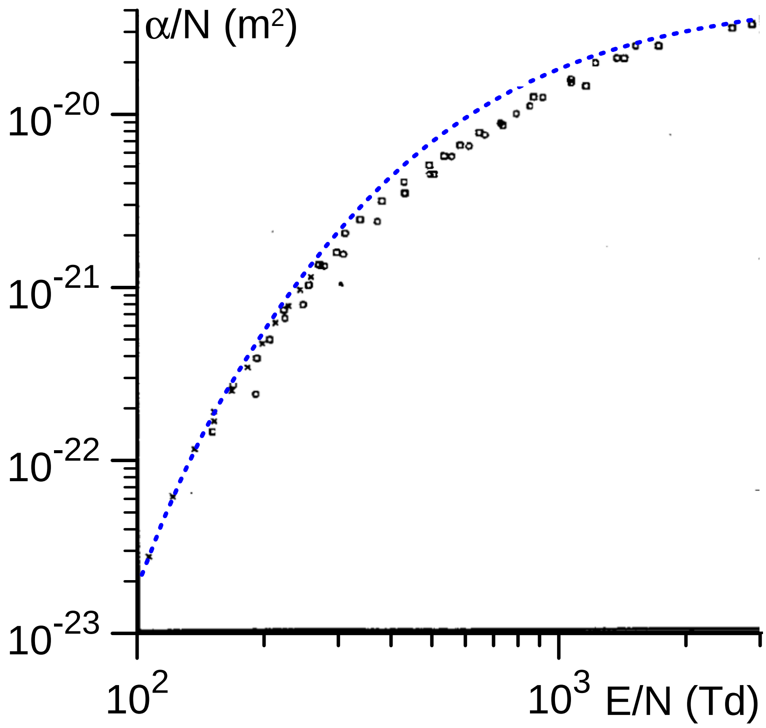

Figure A.2: Townsend ionization coefficient. Dotted: equation (A.4). Points: data from figure 4.4 of [121].

low and the effective ion temperature is not appreciably higher from the neutral gas temperature $T = 300\,\mathrm{K}$, then the O_2^+ ions may be converted into complex ions; e.g., [68]. In the case of humid air, also possible is the formation of cluster ions, comprising one or several H_2O molecules. This means that complex and cluster ions may appear in the drift zone of corona discharges in air, where the reduced electric field E/N is sufficiently low.

One can consider, as a characteristic example, complex ions O_4^+, which are created mostly in the reaction $O_2^+ + 2O_2 \to O_4^+ + O_2$ and destroyed in the reverse reaction. In [126], the reaction $O_2^+ + 2O_2 \to O_4^+ + O_2$, where O_2^+ ions are lost, has the rate constant $k_{167} = 2.4 \times 10^{-30} \left(\frac{300\,\mathrm{K}}{T_{O_2^+}}\right)^{3.2} \mathrm{cm}^6\,\mathrm{s}^{-1}$. The inverse reaction $O_4^+ + O_2 \to O_2^+ + 2O_2$, where O_2^+ ions are produced, has the rate constant $k_{227} = 3.3 \times 10^{-6} \left(\frac{300\,\mathrm{K}}{T_{O_4^+}}\right)^4 \exp\left(-\frac{5030\,\mathrm{K}}{T_{O_4^+}}\right) \mathrm{cm}^3\,\mathrm{s}^{-1}$. Using the equation for local balance, $n_{O_4^+} k_{227} n_{O_2} = n_{O_2^+} k_{167} n_{O_2} n_{O_2}$, one obtains

$$z = 1.78 \times 10^{-5} \frac{n_{O_2}}{N_0} \left(\frac{T_{O_4^+}}{300\,\mathrm{K}}\right)^4 \left(\frac{300\,\mathrm{K}}{T_{O_2^+}}\right)^{3.2} \exp\frac{5030\,\mathrm{K}}{T_{O_4^+}}, \tag{A.6}$$

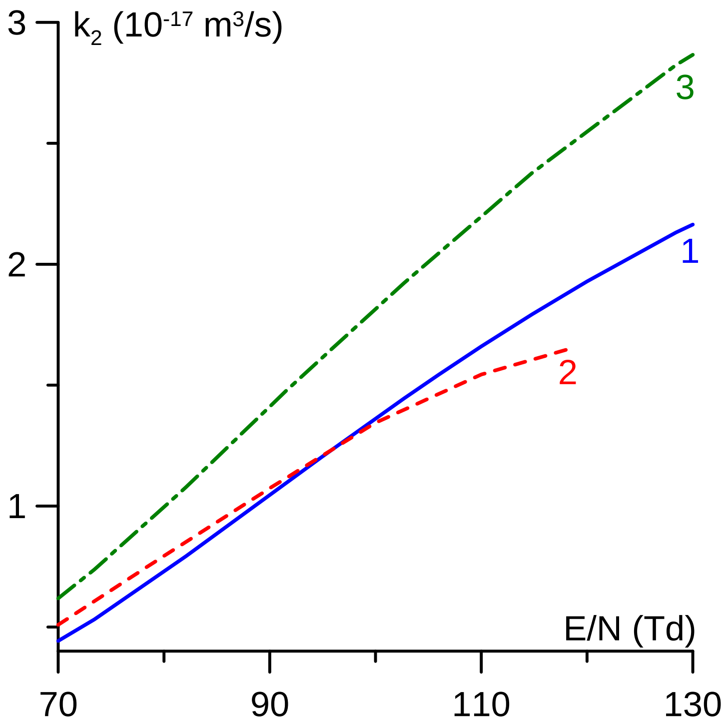

Figure A.3: Dissociative attachment rate constant. 1: evaluation with the use of equation (A.5). 2: experimental data for an N_2-O_2 mixture with 20% oxygen from figure 6b of [122], recalculated to the rate constant. 3: evaluation with the use of the online version of the Bolsig+ solver [116] and the cross sections [117].

where $z = n_{O_4^+}/n_{O_2^+}$, n_α and T_α are the number density and the temperature of species α, and $N_0 = 2.45 \times 10^{25}\ \mathrm{m}^{-3}$ is the standard gas number density (the number density corresponding to the pressure of 1 atm and the gas temperature of 300 K).

Complex ions O_4^+, O_4^-, and cluster ions, have typical mobilities in the range $2.0 - 2.4\,\mathrm{cm}^2\,\mathrm{V}^{-1}\,\mathrm{s}^{-1}$ [68]. Assuming the value of $2.3 \times 10^{-4}\,\mathrm{m}^2\,\mathrm{V}^{-1}\,\mathrm{s}^{-1}$ for the reduced mobility (the mobility rescaled to the standard number density) of ions O_4^+ in air [68], one obtains the following estimate from the Wannier formula (A.1): $T_{O_4^+} = T + 0.037(E/N)^2\mathrm{Td}^{-2}\,\mathrm{K}$. Assuming for the reduced mobility of the O_2^+ ions in air the value of $2.8 \times 10^{-4}\,\mathrm{m}^2\,\mathrm{V}^{-1}\,\mathrm{s}^{-1}$, which corresponds to the reduced mobility given in the Table IIb (p. 68) of compilation [127] for the reduced field of 100 Td, one obtains $T_{O_2^+} = T + 0.054(E/N)^2\mathrm{Td}^{-2}\,\mathrm{K}$.

It follows from Eq. (A.6) that, for the atmospheric pressure and $T = 300\,\mathrm{K}$, $z > 1$ for $E/N \lesssim 51$ Td and $z < 1$ for higher reduced fields; in particular, $z \approx 0.0063$ for $E/N = 100$ Td, which is an approximate value of the critical reduced field in air. This example suggests that the main positive ion species in the active zone of corona and corona-like discharges in air are the O_2^+ ions, with a typical value of the reduced mobility of $2.8 \times 10^{-4}\,\mathrm{m^2\,V^{-1}\,s^{-1}}$. Dominating positive ions in the drift zone are complex and, in the case of humid air, cluster ions, except in the region adjacent to the active zone where E/N approaches 100 Td, with typical reduced mobilities in the range $(2.0 - 2.5) \times 10^{-4}\,\mathrm{m^2\,V^{-1}\,s^{-1}}$ [68].

The dominating process in the active zone is the electron multiplication, which is not directly affected by the presence of positive ions. Hence, the relevant ones are values of the mobility of positive ions in the drift zone. In this work, the reduced mobility of an effective positive ion species is set equal to 2.2 $\times 10^{-4}\,\mathrm{m^2\,V^{-1}\,s^{-1}}$. Similarly, the reduced mobility of the ions O_2^- is also set equal to 2.2 $\times 10^{-4}\,\mathrm{m^2\,V^{-1}\,s^{-1}}$, reflecting the possible formation in the drift zone of the complex and, in the case of humid air, cluster ions [68, 128]. Although not dramatically, the set mobility for ions O_2^+ and O_2^- is slightly different from the values of 2.51 and $2.16\,\mathrm{cm^2\,V^{-1}\,s^{-1}}$, respectively, given in [68] for the individual mobilities of the corresponding ions.

The O^- ions are present mostly at high reduced electric fields, since at low fields these ions are rapidly destroyed by the detachment and converted into the ozone ions. According to [127], in Table IIf (p. 81), the reduced mobility of O^- varies between 3.66 and $5.24\,\mathrm{cm^2\,V^{-1}\,s^{-1}}$ over the reduced field range up to 100 Td (there is no data for higher reduced fields). In principle, such variations can be readily introduced in the numerical model. Since, however, a constant value is used for the mobility of O_2^- (and complex/cluster ions), and given that the above variation is not huge, a constant value of $5.2\,\mathrm{cm^2\,V^{-1}\,s^{-1}}$ is used for the reduced mobility of O^- in order to be consistent. According to [129], the reduced mobility of O_3^- varies between 2.5 and $3.1\,\mathrm{cm^2\,V^{-1}\,s^{-1}}$ over the reduced field range up to 100 Td, and varies between 3.1 and $2.9\,\mathrm{cm^2\,V^{-1}\,s^{-1}}$ over the reduced field range between 100 Td and 240 Td. In this work, the reduced mobility of O_3^- was set equal to 2.7 $\mathrm{cm^2\,V^{-1}\,s^{-1}}$, which is a value characteristic of reduced field of the order of 50 Td, where these ions are expected to be most abundant.

The approximations of rate constants of reactions 5-8 shown in Table A.1 were taken from Table 2 of [78]. For reaction 5 however, the rate constant was increased by the factor of 5 due to the following reason: collisional detachment from O_2^- is written in [78] in the form $O_2^- + M \rightarrow e + O_2 + M$, where M is any of the molecules N_2 and O_2; however, the contribution of the process $O_2^- + N_2$ is small [130], therefore the collisional detachment from O_2^- is written with account of collisions only with O_2. The approximations of rate constants of reactions 5-8 in Table A.1 are valid for variable gas temperature T, in contrast to the approximations given in Appendix of [78], which are valid for $T = 300\,\mathrm{K}$.

Ion-ion and electron-ion recombination are taken into account in reactions 9 and 10 of Table A.1 respectively. Due to the lack of sufficient experimental information, this cannot be done in an accurate way and should be considered rather as an order-of-magnitude estimate. The main mechanism of ion-ion recombination in air, reaction 9, at pressures of the order of 1 bar (1×10^5 Pa) and higher is ion-ion recombination with participation of neutral molecule(s), with the recombination coefficient in the range $(2 - 2.5) \times 10^{-12}\,\mathrm{m^3\,s^{-1}}$ [131]; the rate constant of binary ion-ion recombination is typically of the order of $10^{-13}\,\mathrm{m^3\,s^{-1}}$ (e.g., [126, 132]) and the contribution of this mechanism is small. Hence, at pressures of the order of 1 bar and higher, the coefficient of ion-ion recombination with participation of neutral molecule(s) may be estimated by means of the expression [133, 134]

$$\beta_{ii}^{-1} = (\beta_{i3} N)^{-1} + \beta_{iL}^{-1}, \tag{A.7}$$

where β_{i3} is the three-body recombination rate constant and β_{iL} is the Langevin recombination coefficient. This expression is separately evaluated for each pair of positive (A^+) and negative (O^-, O_2^-, O_3^-) ions. The Langevin recombination coefficient is related to μ_p and μ_n the mobilities of the recombining positive and negative ions by the formula $\varepsilon_0 \beta_{iL} = e\left(\mu_p + \mu_n\right)$. The value of the three-body recombination rate constant for $T = 300$ K and low reduced electric field is assumed equal to $1.5 \times 10^{-37}\,\mathrm{m^6\,s^{-1}}$ for all the three negative ion species; this value ensures a reasonably good agreement of the recombination coefficients for O_2^- and O_3^-, given by Eq. (A.7), with experimental data on the recombination coefficient in air in a wide range of pressures shown in figures 6 and 7 of [131], as can be seen in figures A.4a and A.4b respectively. With increase of the temperature, β_{i3} varies proportionally to T^{-3} [135]. Thus, one can set $\beta_{i3} = 1.5 \times 10^{-37}\,(300\,\mathrm{K}/T_{pn})^3\ \mathrm{m^6\,s^{-1}}$, where T_{pn} is the effective reduced temperature of species p and n given by Eq. (A.2).

Electron-ion recombination, reaction 10, can occur via three channels: dissociative recombination of molecular ions, recombination with participation of neutral molecules, and three-body recombination with the third body being an electron. The most effective dissociative electron-ion recombination process in air is the dissociative recombination of molecular ions O_2^+ and O_4^+. The rate constants of recombination of these ions are $\beta_{e2} = 2 \times 10^{-13}\,(300\,\mathrm{K}/T_e)^{0.7}\ \mathrm{m^3\,s^{-1}}$ [136] and $\beta_{e4} = 4 \times 10^{-12}\,(300\,\mathrm{K}/T_e)^{0.5}\ \mathrm{m^3\,s^{-1}}$ [137], respectively (here T_e is the electron temperature, which in this thesis was evaluated in terms of the electron mean energy with the use of the online version of the Bolsig+ solver [116] and the cross sections [117]). The total rate of electron-ion recombination, accounting for contributions of both these ion species, is $\beta_{e2} n_e n_{O_2^+} + \beta_{e4} n_e n_{O_4^+}$ and is represented in the considered model as $\beta_{ei} n_e n_{A^+}$, where $n_{A^+} = n_{O_2^+} + n_{O_4^+}$ and β_{ei} may be termed electron-ion recombination coefficient. One finds

$$\beta_{ei} = \frac{1}{1+z}\beta_{e2} + \frac{z}{1+z}\beta_{e4}, \tag{A.8}$$

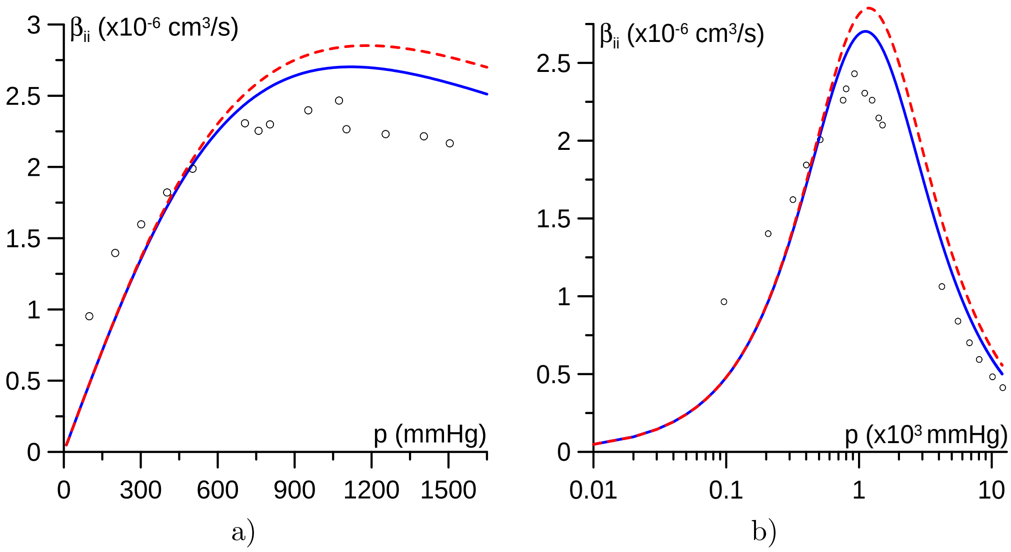

Figure A.4: Ion-ion recombination coefficient β_{ii}, evaluated with the use of equation (A.7). Solid: recombination with O_2^-. Dashed: recombination with O_3^-. Points: experimental data from figure 7 of [131]. a) Lower pressures; b) extended range of pressures.

where z is given by Eq. (A.6). The second term on the rhs of Eq. (A.8), which describes the contribution of O_4^+ to the total recombination rate, can be appreciable even in cases where z is much lower than unity, since the recombination rate constant for this ion is much higher than that for O_2^+; the latter is a typical situation: rate constants of dissociative recombination for complex and cluster ions are by an order of magnitude higher than for diatomic ions.

The coefficient of electron-ion recombination with participation of neutral molecules may be estimated by means of a formula similar to Eq. (A.7). The Langevin electron-ion recombination coefficient may be estimated in terms of the mobility μ_e of electrons, $\beta_{eL} = (e/\varepsilon_0)\,\mu_e$. Since the electron mobility is high (by two orders of magnitude higher than the ion mobility), the Langevin electron-ion recombination is negligible up to the gas pressures of about 100 bar (1×10^7 Pa). The three-body electron-ion recombination with the third body being a gas molecule has been studied in several gases, including CO_2 and H_2O. There are no data available on the three-body recombination of oxygen ions with electrons. In the experiment [138] on recombination of N_4^+ in nitrogen at $T_e = T$, the three-body process has not been observed up to the gas pressure of about 2 bar. It is also known (for CO_2) that the recombination coefficient for the three-body process decreases with increase of T_e much faster than that of the two-body process [139]. On the basis of this information, one can expect that the role of three-body electron-ion recombination with the third body being a gas molecule would not be very appreciable for air pressures up to several tens of bar, although this point requires future study. Thus, the electron-ion recombination with participation of neutral molecules will be neglected in this model.

The rate constant of the three-body electron-ion recombination with a third body being electron may be estimated as $1.4 \times 10^{-31}\,(T_e/300\,\mathrm{K})^{-4.5}\ \mathrm{m}^6\,\mathrm{s}^{-1}$ [140]. This process comes into play at high electron densities, typically those exceeding $10^{24}\,\mathrm{m}^{-3}$, and may be accounted for by adding the corresponding term to the expression (A.8) if appropriate.

Number	Reaction	Evaluation of reaction rate	Reference
1	$e + M \rightarrow 2e + A^+$	$^{a)}$ Equation (A.4)	see text
2	$e + O_2 \rightarrow O^- + O$	$^{a)}$ Equation (A.5)	see text
3	$e + O_2 + M \rightarrow O_2^- + M$	$^{a)}\ \frac{\eta_3}{N^2} = 1.6 \times 10^{-47}\,(E/N)^{-1.1}\ \mathrm{m}^5$	[125]
4	$M + h\nu \rightarrow e + A^+$ $\left(\begin{array}{c} e + N_2 \rightarrow e + N_2^* \\ N_2^* \rightarrow N_2 + h\nu \\ O_2 + h\nu \rightarrow e + O_2^+ \end{array}\right)$	$^{b)}$ Equations (2.4)-(2.6)	[65]
5	$O_2^- + O_2 \rightarrow e + 2O_2$	$^{c)}\ 6.2 \times 10^{-17} \exp\left[-\frac{9050}{T+0.305(E/N)^2}\right]\ \mathrm{m^3\,s^{-1}}$	see text
6	$O^- + N_2 \rightarrow e + N_2O$	$^{c)}\ 1.16 \times 10^{-18} \exp\left[-\frac{882}{T+0.436(E/N)^2}\right]\ \mathrm{m^3\,s^{-1}}$	[78]
7	$O^- + O_2 \rightarrow O + O_2^-$	$^{c)}\ 6.9 \times 10^{-17} \exp\left[-\frac{16200}{T+0.436(E/N)^2}\right]\ \mathrm{m^3\,s^{-1}}$	[78]
8	$O^- + O_2 + M \rightarrow O_3^- + M$	$^{c)}\ 1.3 \times 10^{-42} \exp\left[-\frac{T+0.436(E/N)^2}{1860}\right]\ \mathrm{m^6\,s^{-1}}$	[78]
9	$A^+ + B^- \rightarrow$ products	$^{d)}$ Equation (A.7)	
10	$A^+ + e \rightarrow$ products	$^{d)}$ Equation (A.8)	

Table A.1: Kinetic scheme and relevant kinetic data. $^{a)}$Townsend coefficient. $^{b)}$reaction rate. $^{c)}$reaction rate constant. T in K, E/N in Td. $^{d)}$recombination coefficient. A^+: the effective positive ion species. B^-: any of the negative ions O^-, O_2^-, O_3^-. M: any of the molecules N_2 and O_2.

Appendix B

Townsend relation

This appendix concerns the derivation of the so-called Townsend relation [37], which describes the approximate CVC of a low-current DC corona discharge between concentric cylinders with a wide gap. This derivation uses SI units and hence different numerical factors may appear when compared with [37], which used the CGS system of units.

Let us consider a corona discharge occurring between concentric cylinders, with the radius of the inner and outer cylinder being r_0 and R respectively. Let us assume that current is transported only by ions of species i. The current density $\mathbf{j}$ is given by $\mathbf{j} = e\mathbf{J}_i$, where $\mathbf{J}_i$ is the density of transport flux and e is the elementary charge. If one neglects diffusion, the ion flux within the cylinders is given by $J_{ir} = n_i \, \mu_i E_r$, where μ_i is the ions mobility, n_i its number density and E_r the radial electric field. Hence, the current density is given by $j_r = en_i \, \mu_i E_r$, and the current per unit cylinder length I_l across a surface of arbitrary radius r outside the active zone (a thin region in the vicinity of the sharper electrode where ionization occurs), is given by

$$I_l = 2\pi r j_r = 2\pi r e n_i \mu_i E_r. \tag{B.1}$$

As mentioned above, the space charge between the cylinders is mainly due to the ion species dominating the current in the drift zone, and thus the Poisson equation is given by

$$\frac{1}{r}\frac{d}{dr}\left(rE_r\right) = \frac{en_i}{\varepsilon_0}.$$

Here ε_0 is the permittivity of free space. Substituting n_i, given by Eq.(B.1), into Poisson's equation we have

$$\frac{d}{dr}\left(rE_r\right) = \frac{I_l}{2\pi\varepsilon_0 \mu_i E_r}.$$

Mutiplying Poisson's equation by rE_r and integrating along r yields the field distribution:

$$(rE_r)^2 = \frac{I_l}{2\pi\varepsilon_0\mu_i}r^2 + C.$$

The constant of integration is obtained for $r = r_0$ (at the surface of the inner cylinder), assuming that the field is given by the inception field $E_c = V_t/\left[r_0 \ln\left(\frac{R}{r_0}\right)\right]$ in terms of the ignition voltage V_t (the classic Townsend-Kaptzov assumption, which states that the steady state electric field at the conductor surface remains at the corona onset value E_c):

$$C = r_0^2 E_c^2 - \frac{I_l r_0^2}{2\pi\varepsilon_0\mu_i}.$$

Thus the field distribution is given by

$$(rE_r)^2 = r_0^2 E_c^2 - \frac{I_l}{2\pi\varepsilon_0\mu_i}r_0^2 + \frac{I_l}{2\pi\varepsilon_0\mu_i}r^2. \tag{B.2}$$

When $\frac{I_l}{2\pi\varepsilon_0\mu_i} \ll E_c^2$, Eq.(B.2) becomes

$$rE_r = r_0 E_c \left(1 + \frac{I_l r^2}{2\pi\varepsilon_0\mu_i r_0^2 E_c^2}\right)^{\frac{1}{2}}.$$

The CVC can be obtained by integration since the applied voltage $U = \int\limits_{r_0}^{R} E_r dr$:

$$U = \int\limits_{r_0}^{R} \frac{1}{r} r_0 E_c \left(1 + \frac{I_l r^2}{2\pi\varepsilon_0\mu_i r_0^2 E_c^2}\right)^{\frac{1}{2}} dr. \tag{B.3}$$

Using the substitution $x = \left(1 + \frac{I_l r^2}{2\pi\varepsilon_0\mu_i r_0^2 E_c^2}\right)^{\frac{1}{2}}$ we have:

$$U = r_0 E_c \left((1+\theta)^{\frac{1}{2}} - \left(1 + \frac{\theta r_0^2}{R^2}\right)^{\frac{1}{2}}\right)$$
$$+ \frac{1}{2} r_0 E_c \left\{ \ln\left(\frac{\left[(1+\theta)^{\frac{1}{2}} - 1\right]^2}{\theta}\right) + \ln\left(\frac{\left[\left(1 + \frac{\theta r_0^2}{R^2}\right)^{\frac{1}{2}} + 1\right]^2}{\frac{\theta r_0^2}{R^2}}\right)\right\}.$$

Here $\theta = \frac{R^2}{r_0^2}\frac{I_l}{2\pi\varepsilon_0\mu_i E_c^2}$. If one assumes $I_l \ll 2\pi\varepsilon_0\mu_i E_c^2$,

$$U = r_0 E_c \left\{(1+\theta)^{\frac{1}{2}} - 1 + \ln(2R) - \ln\left(r_0\left[(1+\theta)^{\frac{1}{2}} + 1\right]\right)\right\},$$

When θ is small, $(1+\theta)^{\frac{1}{2}} \approx 1 + \frac{\theta}{2}$, and thus

$$\ln\left(\frac{R}{r_0}\right)\left(\frac{U-V_t}{V_t}\right) = \frac{\theta}{2} - \ln\left(1+\frac{\theta}{4}\right).$$

Using the Maclaurin's series, one can use the approximation $\ln\left(1+\frac{\theta}{4}\right) \approx \frac{\theta}{4}$:

$$\ln\left(\frac{R}{r_0}\right)\left(\frac{U-V_t}{V_t}\right) = \frac{\theta}{4}$$

Substituting $\theta = \frac{R^2}{r_0^2}\frac{I_l}{2\pi\varepsilon_0\mu_i E_c^2} = \frac{R^2 I_l}{2\pi\varepsilon_0\mu_i\left(\frac{V_t}{\ln(R/r_0)}\right)^2}$ we finally have the expression for the CVC given by Townsend in 1914 [37]:

$$I_l = \frac{8\pi\varepsilon_0\mu_i V_t\left(U-V_t\right)}{R^2\ln\left(\frac{R}{r_0}\right)}.$$

Bibliography

[1] Yu. P. Raizer, *Gas Discharge Physics* (Springer, Berlin, 1991).

[2] M. A. Lieberman and A. J. Lichtenberg, *Principles of Plasma Discharges and Material Processing*, 2nd ed. (Wiley, New York, 2005).

[3] G. L. Weissler, Phys. Rev. **63**, 96 (1943).

[4] L. B. Loeb, Phys. Rev. **71**, 712 (1947).

[5] N. G. C. Ferreira, P. G. C. Almeida, M. S. Benilov, V. A. Panarin, V. S. Skakun, V. F. Tarasenko, and G. V. Naidis, IEEE Trans. Plasma Sci. **48**, 4080 (2020).

[6] M. Goldman and A. Goldman, in *Gaseous Electronics*, edited by M. Hirsh and H. J. Oskam (Academic Press, 1978) pp. 219 – 290.

[7] H. C. Pollock and F. S. Cooper, Phys. Rev. **56**, 170 (1939).

[8] T. R. Foord, Proc. IEE - Part II: Power Engineering **100**, 585 (1953).

[9] M. Robinson, J. Appl. Phys. **40**, 5107 (1969).

[10] E. Kuffel, W. S. Zaengl, and J. Kuffel, *High Voltage Engineering*, 2nd ed. (Newnes, Oxford, 2000).

[11] F. W. Peek, *Dielectric phenomena in high-voltage engineering* (McGraw-Hill Book Company, Inc., New York, 1929).

[12] L. C. Pitchford, L. L. Alves, K. Bartschat, *et al.*, Plasma Processes Polym. **14**, 1600098 (2017).

[13] A. T. del Caz, V. Guerra, D. Gonçalves, M. L. da Silva, L. Marques, N. P. ao, C. D. Pintassilgo, and L. L. Alves, Plasma Sources Sci. Technol. **28**, 043001 (2019).

[14] M. J. Kushner, J. Phys. D: Appl. Phys. **38**, 1633 (2005).

[15] J. van Dijk, K. Peerenboom, M. Jimenez, D. Mihailova, and J. van der Mullen, J. Phys. D: Appl. Phys. **42**, 194012 (2009).

[16] A. Pedersen, in *Electrical Insulation and Dielectric Phenomena, 1989. Annual Report., Conference on* (IEEE, 1989) pp. 21–58.

[17] A. Hopf, M. Rossner, F. Berger, and A. Kuchler, in *2020 IEEE Electrical Insulation Conference (EIC)* (IEEE, Virtual Event, 2020) pp. 118–123.

[18] F. W. Peek, Trans. Am. Inst. Electr. Eng. **XXXIII**, 923 (1914).

[19] W. S. Zaengl and H. U. Nyffenegger, in *Proceedings, 3rd International Conference on Gas Discharges* (1974) pp. 302–305.

[20] J.-R. Riba, A. Morosini, and F. Capelli, Energies (2018).

[21] F. Paschen, Ann. Phys. **273**, 69 (1889).

[22] T. W. Dakin, G. Luxa, G. Oppermann, J. Vigreux, G. Wind, and H. Winkelnkemper, Electra **32**, 61 (1974).

[23] J. S. E. Townsend, *Electricity in Gases* (Oxford, Clarendon Press, 1915).

[24] H. Raether, *Electron avalanches and breakdown in gases*, Butterworths advanced physics series (Butterworths, London, 1964).

[25] J. M. Meek and J. D. Craggs, *Electrical breakdown of gases*, Wiley series in plasma physics (John Wiley and Sons, Ltd, United States, 1978).

[26] R. Hackam and G. Raju, IEEE T. Electr. Insul. **8**, 142 (1973).

[27] N. Malik, IEEE T. Electr. Insul. **16**, 463 (1981).

[28] K. Petcharaks, in *11th International Symposium on High Voltage Engineering, 1999* (IET, 1999) pp. 19–22.

[29] J. J. Lowke and F. D'Alessandro, J. Phys. D: Appl. Phys. **36**, 2673 (2003).

[30] G. V. Naidis, J. Phys. D: Appl. Phys. **38**, 2211 (2005).

[31] P. Ortega, R. Diaz, F. Heilbronner, and F. Ruhling, J. Phys. D: Appl. Phys. **40**, 7000 (2007).

[32] S. Pancheshnyi, in *31st International Conference on Phenomena in Ionized Gases (ICPIG), Granada 2013* (2013).

[33] S. Pancheshnyi, in *31st International Conference on Phenomena in Ionized Gases (ICPIG), Granada 2013* (2013).

[34] M. Seeger, P. Stoller, and A. Garyfallos, IEEE Trans. Dielectr. Electr. Insul. **24**, 1582 (2017).

[35] A. M. Loveless and A. L. Garner, IEEE Trans. Plasma Sci. **45**, 574 (2017).

[36] N. Monrolin, O. Praud, and F. Plouraboué, Phys. Plasmas **25**, 063503 (2018).

[37] J. S. Townsend, London, Edinburgh, and Dublin Philos. Mag. J. Sci. **28**, 83 (1914).

[38] C. S. Fazel and S. R. Parsons, Phys. Rev. **23**, 598 (1924).

[39] P. Giubbilini, J. Appl. Phys. **64**, 3730 (1988).

[40] G. F. L. Ferreira, O. N. Oliveira, and J. A. Giacometti, J. Appl. Phys. **59**, 3045 (1986).

[41] X. Meng, H. Zhang, and J. Zhu, J. Phys. D: Appl. Phys. **41**, 065209 (2008).

[42] Y. Zheng, B. Zhang, and J. He, Phys. Plasmas **22**, 023501 (2015).

[43] A. Aliat, C. T. Hung, C. J. Tsai, and J. S. Wu, J. Phys. D: Appl. Phys. **42**, 125206 (2009).

[44] Y. Cui, C. Zhuang, and R. Zeng, Appl. Phys. Lett. **115**, 244101 (2019).

[45] R. S. Sigmond, J. Appl. Phys. **53**, 891 (1982).

[46] P. G. C. Almeida, M. S. Benilov, M. D. Cunha, and J. G. L. Gomes, Plasma Processes Polym. **14**, 1600122 (2017).

[47] B. Bagheri, J. Teunissen, U. Ebert, M. M. Becker, S. Chen, O. Ducasse, O. Eichwald, D. Loffhagen, A. Luque, D. Mihailova, J. M. Plewa, J. van Dijk, and M. Yousfi, Plasma Sources Sci. Technol. **27**, 095002 (2018).

[48] R. Morrow, J. Phys. D: Appl. Phys. **30**, 3099 (1997).

[49] W. Zhang, T. S. Fisher, and S. V. Garimella, J. Appl. Phys. **96**, 6066 (2004).

[50] Yu. Akishev, M. Grushin, I. Kochetov, V. Karal'nik, A. Napartovich, and N. Trushkin, Plasma Sources Sci. Technol. **14**, S18 (2005).

[51] B.-J. Lee, H. Rahaman, K. Frank, L. Mares, and D.-L. Biborosch, in *Proc. 28th ICPIG (Prague, July 2007)*, edited by J. Schmidt, M. Šimek, S. Pekárek, and V. Prukner (Institute of Plasma Physics AS CR, ISBN 978-80-87026-01-4, Prague, 2007) pp. 900–902.

[52] Y. Park, R. K. Jha, C. Park, S. B. Rhee, J. H. Lee, C. G. Park, and S. H. Lee, IEEE Trans. Power Delivery **33**, 2856 (2018).

[53] P. Sattari, G. S. P. Castle, and K. Adamiak, IEEE Trans. Ind. Appl. **46**, 1699 (2010).

[54] P. Sattari, C. F. Gallo, G. S. P. Castle, and K. Adamiak, J. Phys. D: Appl. Phys. **44**, 155502 (2011).

[55] T. N. Tran, I. O. Golosnoy, P. L. Lewin, and G. E. Georghiou, J. Phys. D: Appl. Phys. **44**, 015203 (2010).

[56] P. Dordizadeh, K. Adamiak, and G. S. P. Castle, J. Phys. D: Appl. Phys. **48**, 415203 (2015).

[57] L. Liu and M. Becerra, J. Phys. D: Appl. Phys. **50**, 105204 (2017).

[58] C. Zogning, J. Lobry, and F. Moiny, in *2020 International Symposium on Electrical Insulating Materials (ISEIM)* (2020) pp. 552–560.

[59] L. Chuan, L. Zhi, W. Pengyu, Z. Ming, Y. Yong, and Y. Kexun, Plasma Sources Sci. Technol. **29**, 045011 (2020).

[60] N. G. C. Ferreira, D. F. N. Santos, P. G. C. Almeida, G. V. Naidis, and M. S. Benilov, J. Phys. D: Appl. Phys. **52**, 355206 (2019).

[61] N. G. C. Ferreira, P. G. C. Almeida, M. S. Benilov, and G. V. Naidis, Appl. Phys. Lett. **117**, 026101 (2020).

[62] N. G. C. Ferreira, G. V. Naidis, and M. S. Benilov, J. Phys. D: Appl. Phys. **54**, 255203 (2021).

[63] P. G. C. Almeida, R. M. S. Almeida, N. G. C. Ferreira, G. V. Naidis, and M. S. Benilov, Plasma Sources Sci. Technol. **29**, 125005 (2020).

[64] A. H. Howell, Electrical Engineering **58**, 193 (1939).

[65] A. Bourdon, V. P. Pasko, N. Y. Liu, S. Celestin, P. Segur, and E. Marode, Plasma Sources Sci. Technol. **16**, 656 (2007).

[66] M. B. Zheleznyak, A. K. Mnatsakanyan, and S. V. Sizykh, High Temp. **20**, 357 (1982).

[67] M. S. Benilov, P. G. C. Almeida, N. G. Ferreira, R. M. S. Almeida, and G. V. Naidis, J. Appl. Phys. **130**, 121101 (2021).

[68] A. V. Filippov, I. N. Derbenev, N. A. Dyatko, S. A. Kurkin, G. B. Lopantseva, A. F. Pal', and A. N. Starostin, J. Exp. Theor. Phys. **125**, 246âĂŞ267 (2017).

[69] L. C. Pitchford, L. L. Alves, K. Bartschat, S. F. Biagi, M. Bordage, I. Bray, C. E. Brion, M. J. Brunger, L. Campbell, A. Chachereau, B. Chaudhury, L. G. Christophorou, E. Carbone, N. A. Dyatko, C. M. Franck, D. V. Fursa, R. K. Gangwar, V. Guerra, P. Haefliger, G. J. M. Hagelaar, A. Hoesl, Y. Itikawa, I. V. Kochetov, R. P. McEachran, W. L. Morgan, A. P. Napartovich, V. Puech, M. Rabie, L. Sharma, R. Srivastava, A. D. Stauffer, J. Tennyson, J. de Urquijo, J. van Dijk, L. A. Viehland, M. C. Zammit, O. Zatsarinny, and S. Pancheshnyi, Plasma Processes Polym. **14**, 1600098 (2017).

[70] N. G. C. Ferreira, P. G. C. Almeida, G. V. Naidis, and M. S. Benilov, in *Proc. XXXIII ICPIG (9-14 July 2017, Estoril, Portugal)* (2017) p. 325.

[71] M. Robinson, IEEE T. Power. Ap. Syst. **PAS-86**, 185 (1967).

[72] R. T. Waters and W. B. Stark, J. Phys. D: Appl. Phys. **8**, 416 (1975).

[73] H. Isa, Y. Sonoi, and M. Hayashi, IEEE T. Electr. Insul. **26**, 291 (1991).

[74] A. Takahashi and K. Nishijima, IEEE Trans. Dielectr. Electr. Insul. **1**, 590 (1994).

[75] X. Bian, L. Wang, J. M. K. Macalpine, Z. Guan, J. Hui, and Y. Chen, IEEE Trans. Dielectr. Electr. Insul. **17**, 63 (2010).

[76] M. Radmilović-Radjenović, B. Radjenović, Š. Matejčik, and M. Klas, Plasma Chem. Plasma Process. **34** (2014).

[77] A. Kh. Mnatsakanyan, G. V. Naidis, and Yu. M. Solozobov, High Temperature **24**, 771 (1986).

[78] S. Pancheshnyi, J. Phys. D: Appl. Phys. **46**, 155201 (2013).

[79] R. V. Latham and N. S. Xu, Vacuum **42**, 1173 (1991).

[80] R. V. Latham, ed., *High Voltage Vacuum Insulation. Basic Concepts and Technological Practice* (Academic Press, 1995).

[81] W. Wuensch, in *8th International Workshop on Mechanisms of Vacuum Arcs (Sept. 15 - 19, Padova, Italy, 2019)* (2019) p. 11.

[82] D. N. Sinelnikov, *Low-field emission from plasma-contacting materials of thermonuclear devices*, Ph.D. thesis, National Research Nuclear University "MEPhI" (2014), in Russian.

[83] R. S. Dhariwal, M. F. Ahmad, and M. P. Y. Desmulliez, in *MEMS Design, Fabrication, Characterization, and Packaging*, Vol. 4407, edited by U. F. W. Behringer and D. G. Uttamchandani, International Society for Optics and Photonics (SPIE, 2001) pp. 172 – 179.

[84] E. H. Cohen, Proceedings of the IEE - Part A: Power Engineering **103**, 57 (1956).

[85] N. G. C. Ferreira, G. V. Naidis, and M. S. Benilov, in *8th International Workshop on Mechanisms of Vacuum Arcs (Padova, Italy, Sept. 15 - 19, 2019)* (2019) p. 18.

[86] E. Hourdakis, G. W. Bryant, and N. M. Zimmerman, J. Appl. Phys. **100**, 123306 (2006), https://doi.org/10.1063/1.2400103 .

[87] D. B. Go and D. A. Pohlman, J. Appl. Phys. **107**, 103303 (2010).

[88] D. B. Go and A. Venkattraman, J. Phys. D: Appl. Phys. **47**, 503001 (2014).

[89] J. A. Buendia and A. Venkattraman, Europhys. Lett. **112**, 55002 (2015).

[90] A. M. Loveless and A. L. Garner, Phys. Plasmas **24**, 113522 (2017).

[91] Y. Fu, P. Zhang, J. Krek, and J. P. Verboncoeur, Appl. Phys. Lett. **114**, 014102 (2019).

[92] Y. Fu, P. Zhang, J. P. Verboncoeur, and X. Wang, Plasma Res. Express **2**, 013001 (2020).

[93] A. L. Garner, G. Meng, Y. Fu, A. M. Loveless, R. S. Brayfield, and A. M. Darr, J. Appl. Phys. **128**, 210903 (2020).

[94] W. S. Boyle and P. Kisliuk, Phys. Rev. **97**, 255 (1955).

[95] R. G. Forbes, J. H. B. Deane, N. Hamid, and H. S. Sim, J. Vac. Sci. Technol. B **22**, 1222 (2004).

[96] M. Khalifa, M. Abdel-Salam, R. Radwan, and K. Ali, IEEE Trans. Power. Ap. Syst. **96**, 886 (1977).

[97] S. Gossmann, A. Geisler, B. Lutz, and P. G. Nikolic, in *Proc. of the XXII International Conference on Gas Discharges and Their Applications (Sept. 2-7, 2018, Novi Sad, Serbia)*, Vol. 1, edited by Z. Petrović, N. Puač, S. Dujko, and N. Škoro (Serbian Academy of Sciences and Arts, and Institute of Physics, University of Belgrade, 2018).

[98] I. D. Kaganovich, V. I. Demidov, S. F. Adams, and Y. Raitses, Plasma Phys. Controlled Fusion **51**, 124003 (2009).

[99] L. D. Tsendin, Phys. Usp. **53**, 133 (2010).

[100] L. Xu, A. V. Khrabrov, I. D. Kaganovich, and T. J. Sommerer, Phys. Plasmas **24**, 093511 (2017).

[101] D. Levko, R. R. Arslanbekov, and V. I. Kolobov, Phys. Plasmas **26**, 064502 (2019).

[102] A. Kyritsakis, M. Veske, K. Eimre, V. Zadin, and F. Djurabekova, J. Phys. D: Appl. Phys. **51**, 225203 (2018).

[103] H. T. C. Kaufmann, I. Profatilova, I. Popov, W. Wuensch, and M. S. Benilov, in *9th International Workshop on Mechanisms of Vacuum Arcs (online, March 8-12, 2021)* (2021).

[104] S. Berger, IEEE T. Power. Ap. Syst. **95**, 1073 (1976).

[105] O. C. Feet, M. Seeger, D. Over, K. Niayesh, and F. Mauseth, Energies **13** (2020), 10.3390/en13174449.

[106] Y. Zheng, L. Wang, D. Wang, and S. Jia, Phys. Plasmas **24**, 063515 (2017).

[107] S. Chen, K. Li, and S. Nijdam, Plasma Sources Sci. Technol. **28**, 055017 (2019).

[108] Y. K. Stishkov, A. V. Samusenko, and I. A. Ashikhmin, Phys. Usp. **61**, 1213 (2018).

[109] M. Abdel-Salam and N. L. Allen, IEE Proc. Sci. Meas. Technol. **150**, 135 (2003).

[110] P. Atten, K. Adamiak, B. Khaddour, and J. Fourier, J. Optoelectron. Adv. Mater. **6** (2004).

[111] K. Adamiak, V. Atrazhev, and P. Atten, IEEE Trans. Dielectr. Electr. Insul. **12**, 1015 (2005).

[112] K. Yanallah and F. Pontiga, Plasma Sources Sci. Technol. **21**, 045007 (2012).

[113] M. S. Benilov, Plasma Sources Sci. Technol. **23**, 054019 (2014).

[114] A. F. Gutsol and W. R. Pyle, Plasma Sources Sci. Technol. **23**, 054015 (2014).

[115] S. Chen, R. G. W. van den Berg, and S. Nijdam, Plasma Sources Sci. Technol. **27**, 055021 (2018).

[116] G. J. M. Hagelaar and L. C. Pitchford, Plasma Sources Sci. Technol. **14**, 722 (2005).

[117] Phelps database, `www.lxcat.net` (retrieved Jan. 29, 2019).

[118] K. Masuyama and S. R. H. Barrett, Proceedings of the Royal Society A: Mathematical, Physical and Engineering Sciences **469**, 20120623 (2013).

[119] N. Monrolin, F. Plouraboué, and O. Praud, AIAA Journal **55**, 1 (2017).

[120] E. A. Mason and E. W. McDaniel, *Transport Properties of Ions in Gases* (Wiley, New York, 1988).

[121] J. W. Gallagher, E. C. Beaty, J. Dutton, and L. C. Pitchford, J. Phys. Chem. Ref. Data **12**, 109 (1983).

[122] P. Haefliger, A. Hösl, and C. M. Franck, J. Phys. D: Appl. Phys. **51**, 355201 (2018).

[123] A. Hösl, P. Haefliger, and C. M. Franck, J. Phys. D: Appl. Phys. **50**, 485207 (2017).

[124] M. S. Benilov and G. V. Naidis, J. Phys. D: Appl. Phys. **36**, 1834 (2003).

[125] R. S. Sigmond, J. Appl. Phys. **56**, 1355 (1984).

[126] I. A. Kossyi, A. Y. Kostinsky, A. A. Matveyev, and V. P. Silakov, Plasma Sources Sci. Technol. **1**, 207 (1992).

[127] L. A. Viehland and E. A. Mason, At. Data Nucl. Data Tables **60**, 37 (1995).

[128] N. Popov, Plasma Physics Reports **36**, 812 (2010).

[129] H. Böhringer, D. W. Fahey, W. Lindinger, F. Howorka, F. C. Fehsenfeld, and D. L. Albritton, Int. J. Mass Spectrom. Ion Processes **81**, 45 (1987).

[130] A. V. Phelps, Can. J. Chem. **47**, 1783 (1969), https://doi.org/10.1139/v69-289 .

[131] J. Sayers and E. V. Appleton, Proc. R. Soc. Lond. A **169**, 83 (1938).

[132] A. Fridman, *Plasma Chemistry* (Cambridge University Press, Cambridge, UK, 2008).

[133] D. R. Bates and M. R. Flannery, J. Phys. B: At. Mol. Phys. **2**, 184 (1969).

[134] E. W. McDaniel and W. L. Nighan, *Gas Lasers: Applied Atomic Collision Physics, Vol. 3* (Academic Press, New York, NY, 1982).

[135] D. R. Bates, J. Phys. B: At. Mol. Phys. **13**, L623 (1980).

[136] C. H. Sheehan and J. P. St.-Maurice, J. Geophys. Res. Space Phys. **109**, A03302 (2004).

[137] J. L. Dulaney, M. A. Biondi, and R. Johnsen, Phys. Rev. A **37**, 2539 (1988).

[138] Y. Ikezoe, S. Matsuoka, and H. Nakamura, Chem. Phys. Lett. **177**, 366 (1991).

[139] I. M. Littlewood, M. C. Cornell, B. K. Clark, and K. J. Nygaard, J. Phys. D: Appl. Phys. **16**, 2113 (1983).

[140] B. Makin and J. C. Keck, Phys. Rev. Lett. **11**, 281 (1963).